Diphenylalanine self-assembly

Kinetics, thermodynamics and its relevance to amyloidogenesis

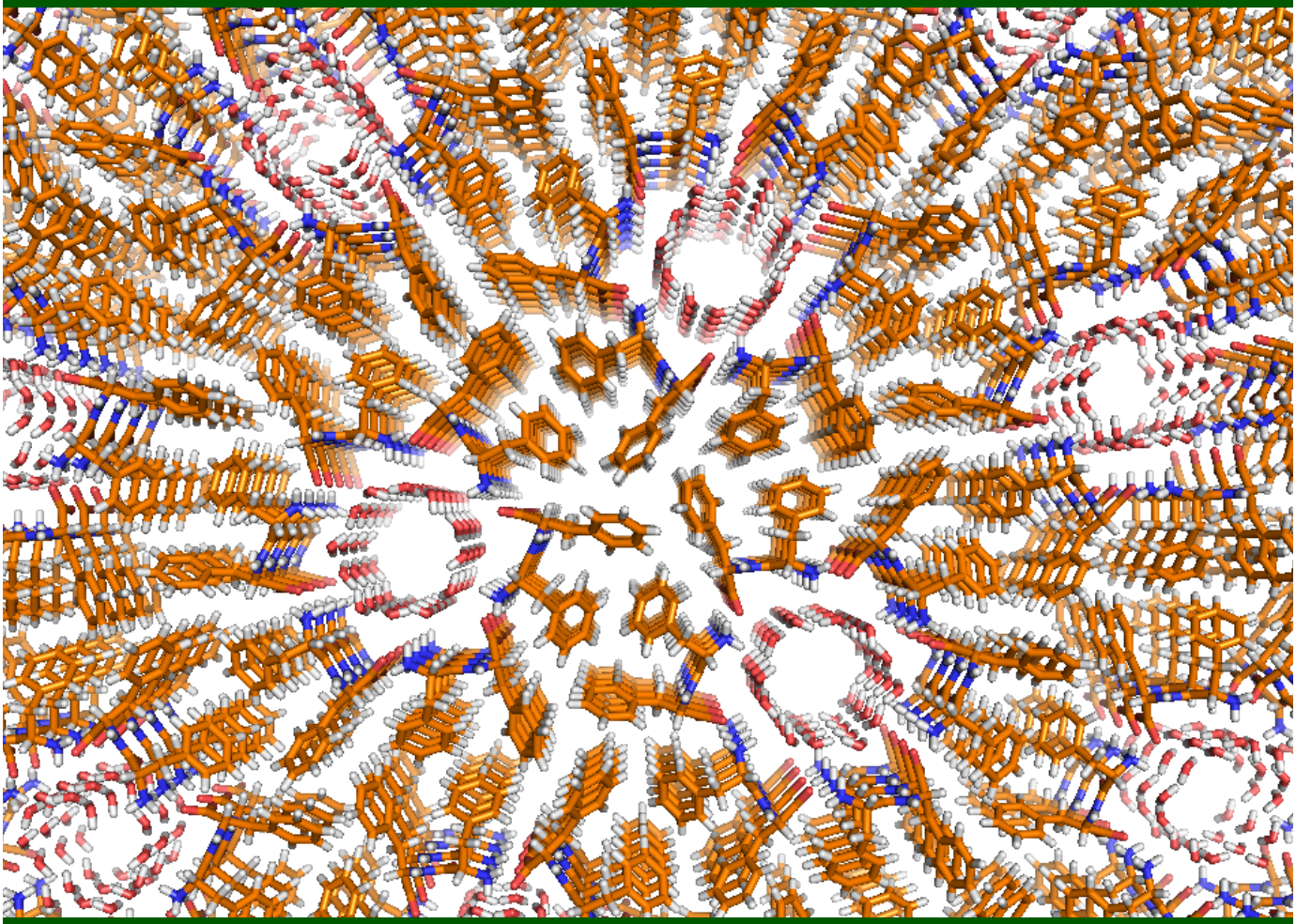

by

T. O. Mason

Supervisor

Prof. T. P. J. Knowles

St Edmund's College, University of Cambridge

Department of Chemistry

PhD Thesis, Sep. 2016

Declaration

This is an account of work carried out at the Department of Chemistry as per the requirements of the Doctor of Philosophy degree. This dissertation is the result of my own work and includes nothing which is the outcome of work done in collaboration except as declared in the Preface and specified in the text. It is not substantially the same as any that I have submitted, or, is being concurrently submitted for a degree or diploma or other qualification at the University of Cambridge or any other University or similar institution except as declared in the Preface and specified in the text. I further state that no substantial part of my dissertation has already been submitted, or, is being concurrently submitted for any such degree, diploma or other qualification at the University of Cambridge or any other University of similar institution except as declared in the Preface and specified in the text.

It does not exceed the prescribed word limit of 60,000 words.

Acknowledgements

I would like to thank:
Dr. Alex Buell and Prof. Tuomas Knowles for their invaluable assistance during the practical work presented here and for their supervision of my research during my studies here, and in the preparation of the chapters, of which this report is the aggregated state. This has been a fascinating project, due in no small part to the skill and efforts of my supervisors.
Dr. Aviad Levin, for his experimental contributions and for many important discussions about the diphenylalanine system.
Dr. Dima Chirgadze, for his expert resolution of the novel solvomorph described herein.
Prof. Ehud Gazit and the Gazit group at the University of Tel Aviv, my hosts during my short-term fellowship. The group carries out cutting-edge research into, among other things, short peptide self-assembly, characterisation, and application. I greatly enjoyed my time with the Gazit group, and look forward to seeing them again in the future.
Dr. Ulyana Shimanovich, who brought me into a fascinating microgel project and in whose group at the Weizmann Institute I hope to continue my research.
Prof. Chris Dobson, for his enlightening input into the work presented here.

-and indeed all others I have been privileged to work with during my time in Cambridge and Tel Aviv.

The author thanks the Newman Foundation and Elan Pharmaceuticals for financial support during the course of this work.

[1]

[1]The experimental data for the thermodynamics displayed in figure 3.1 was obtained during the work towards my part III project for the M. Sci. qualification at the University of Cambridge in 2012. The basic elements of the experimental protocol for chapter 2 was also originally developed during this time and has been refined and extended as part of this work.

Publications

Expanding the Solvent Chemical Space for Self-Assembly of Dipeptide Nanostructures

T. O. Mason, D. Y. Chirgadze, A. Levin, L. Adler-Abramovich, E. Gazit, T. P. J. Knowles and A. K. Buell

ACS Nano, 2014, 8, 1243

Chapter 5 is based on this work. I performed the experiments, and wrote the entirety of the first draft of this paper.

Synthesis of Nonequilibrium Supramolecular Peptide Polymers on a Microfluidic Platform

T. O. Mason, T. C. T. Michaels, A. Levin, E. Gazit, C. M. Dobson, A. K. Buell, and T. P. J. Knowles

Journal of the American Chemical Society 2016 138 (30), 9589-9596

Chapter 2 is based on this work. I performed the experiments and wrote the entirety of the first draft of this paper.

Thermodynamics of polypeptide supramolecular assembly in the short chain limit

T. O. Mason, T. C. T. Michaels, A. Levin, C. M. Dobson, E. Gazit, T. P. J. Knowles and A. K. Buell

Journal of the American Chemical Society, in press

Chapter 3 is based on this work. I performed the experiments and wrote the entirety of the first draft of this paper.

Ostwald's rule of stages governs structural transitions and morphology of dipeptide supramolecular polymers

A. Levin*, **T. O. Mason***, L. Adler-Abramovich, A. K. Buell, G. Meisl, C. Galvagnion, Y. Bram, S. A. Stratford, C. M. Dobson, T. P. J. Knowles and E. Gazit

Nature Communications, 2014, 5, 5219

Chapter 4 is based on this work. I wrote significant parts of the first draft of this paper and performed the experiments not otherwise attributed in the text. This chapter reflects my notes from the time of the study and my contribution to the experimental work.

Elastic instability-mediated actuation by a supra-molecular polymer
A. Levin, T. C. T. Michaels, L. Adler-Abramovich, **T. O. Mason**, T. Müller, B. Zhang, L. Mahadevan, E. Gazit and Tuomas P. J. Knowles
Nature Physics, 2016, 12, 926930
Chapter 5 contains elements from my contribution to this work.

Protein Microgels from Amyloid Fibril Networks
U. Shimanovich, I. Efimov, **T. O. Mason**, P. Flagmeier, A.K. Buell, A. Gedanken, S. Linse, K.S. Åkerfeldt, C.M. Dobson, D.A. Weitz and T.P.J. Knowles
ACS Nano, 2015, 9, 43-51

Self-Assembly of Amyloid Fibrils Displaying Active Enzymes
X. M. Zhou, A. Entwistle, H. Zhang, A. P. Jackson, **T. O. Mason**, U. Shimanovich, T. P. J. Knowles, A. T. Smith, E. B. Sawyer and S. Perrett
ChemCatChem, 2014, 6, 7, 1961-1968

Nanoscale spatially resolved infrared spectra from single microdroplets
T. Müller,* F. S. Ruggeri,* A. J. Kulik, U. Shimanovich, **T. O. Mason**, T. P. J. Knowles and G. Dietler
Lab on a Chip, 2014, 14, 1315

Micro-and nanoscale hierarchical structure of coreshell protein microgels
L. R. Volpatti, U. Shimanovich, F. S. Ruggeri, S. Bolisetty, T. Müller, **T. O. Mason**, T. C. T. Michaels, R. Mezzenga, G. Dietler and T. P. J. Knowles
Journal of Materials Chemistry B, 2016, 4, 48, 7989-7999

Abstract

Diphenylalanine (FF) is a dipeptide capable of self-assembly in aqueous solution into needle-like hollow micro- and nanocrystals that possess advantageous properties such as high stiffness and piezoelectricity and have emerged as attractive candidates for functional nanomaterials. In addition, these structures can be made conductive or used as scaffolds for organising functional entities which do not on their own possess a propensity towards self-assembly. At the start of this project, despite wide-ranging interest in the FF assemblies, many important and fundamental aspects of the system remained relatively unexplored. The scope of the present work ranges from nanomaterials science to the relevance of the dipeptide as a model system for the study of aromatic π-stacking interactions in amyloidogenesis. The basic thermodynamic parameters of FF assembly, the kinetics of that process, and the similarities with, and differences from, the process of fibrillogenesis in polypeptides are explored in detail. The solubility of diphenylalanine in a range of organic solvents and the role of cosolvents in the kinetics of structural assembly were systematically investigated. We find that not only the crystal habit depends on the solvent conditions, but indeed different solvomorphs, possibly differing greatly in mechanical properties, can be obtained from self-assembly in different solvents. The thermodynamics of the dipeptide self-assembly are calculated and placed in the context of earlier work on the free energy of fibril elongation for a range of amyloidogenic polypeptides. It is established that FF aggregation displays the temperature dependence typical of hydrophobic desolvation processes, and that as a model amyloid-forming peptide it displays greater aggregation propensity per amino acid than naturally-occurring polypeptides, due in part to its crystalline as opposed to fibrillar aggregate state. Transition-state measurements are made and the nature of the transition state is elucidated- at the highest-energy point on the aggregation pathway, it is thought that the hydrophobic substituents are still solvent-exposed. The kinetics of self-assembly as a function of solution concentration are quantified through the use of microfluidic techniques,

enabling high precision, time-resolved monitoring of the growth process. This work represents the first systematic study of the dependence of the growth rate of diphenylalanine on solution supersaturation. It is found that the aggregation process occurs through established mechanisms of crystal growth. The detailed dependence is shown, and the applicability of the results is demonstrated through the control of the aspect ratio of populations of the assemblies.

Tom Mason

Diphenylalanine self-assembly- kinetics, thermodynamics and its relevance to amyloidogenesis

Contents

Chapter 1

Introduction

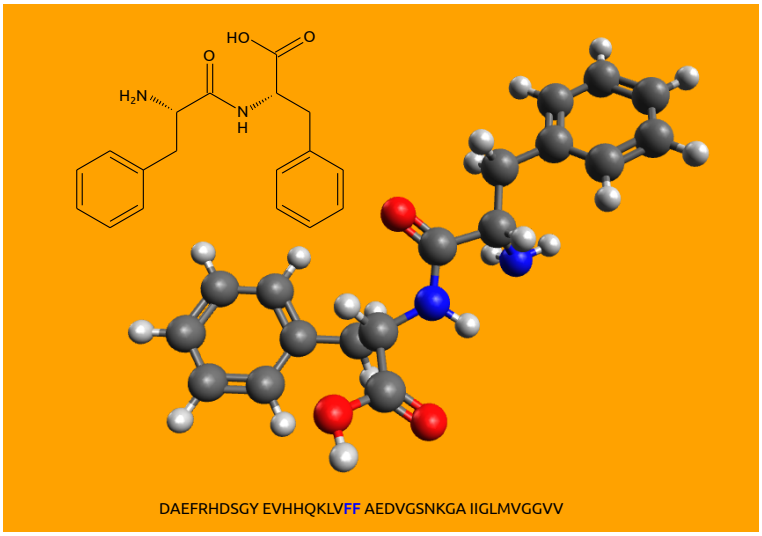

Figure 1.1: Diphenylalanine and the sequence of the Aβ_{1-40} polypeptide

The dipeptide diphenylalanine (FF) has been the subject of much interest following characterisation of its self-assembly [1, 2] due to the unusual morphology of its aggregate; FF assemblies as grown from water solution are rod-like with high aspect ratios and display axial hollow cores [3]. The dipeptide forms the central motif of the Alzheimer's beta peptides (19F, 20F) and the role of $\pi-\pi$ interactions in the general case of polypeptide aggregation has

been the subject of much study and a review by Gazit [4]. The preparation of the assemblies is accomplished very easily, typically through the introduction of a high concentration stock solution in hexafluoroisopropanol into water. This leads to rapid, uncontrolled precipitation of small crystallites which grow rapidly as in figure 1.2 (a). Alternatively, the assemblies may be grown by nucleation from a slowly-cooled aqueous solution, yielding macroscopic polycrystalline species with broad hollow cores detectable by light microscopy as in figure 1.2 (b,c).

Potential applications of diphenylalanine assemblies in nanoscience have been explored extensively, including the casting of silver nanowires [2] and even coaxial nanocables, made possible by the unusual morphology of the water-grown crystals and their ability to undergo surface modification [5]. Other key properties of the dipeptide nanostructures include intrinsic ferro- [6] and piezoelectricity [7] as well as high mechanical [8] [9] and thermal stability [10]. Nanoporous dipeptide structures represent a class [11] of bioinspired nanomaterials having similarities, both in composition and morphology with amyloid-based nanomaterials, dependent on the alignment of the inter-peptide group hydrogen bonding [3, 12]. It has been shown that the morphologies of the assemblies can be varied through chemical modification of the FF peptide [13, 14] or through control of the external conditions during the self-assembly process [15].

Solvent environment and chemical identity of a macromolecule determines its aggregation behaviour in solution. In polypeptide systems, absent posttranslational modification, the macromolecule is a polyamide chain decorated with one of 20 side chains, or "residues" bonded to the α-carbon. The individual building blocks (amino acids) can be grouped according to the nature of this side chain.

Three of the twenty carry a positive charge at physiological pH, arginine (R), histidine (H) and lysine (K), and two are acidic, carrying a negative charge- aspartic (D) and glutamic (E) acids. Four amino acids are uncharged, but with polar side chains- serine (S), threonine (T), asparagine (N) and glutamine (Q). Leaving aside the particular cases of cysteine (sulphydryl

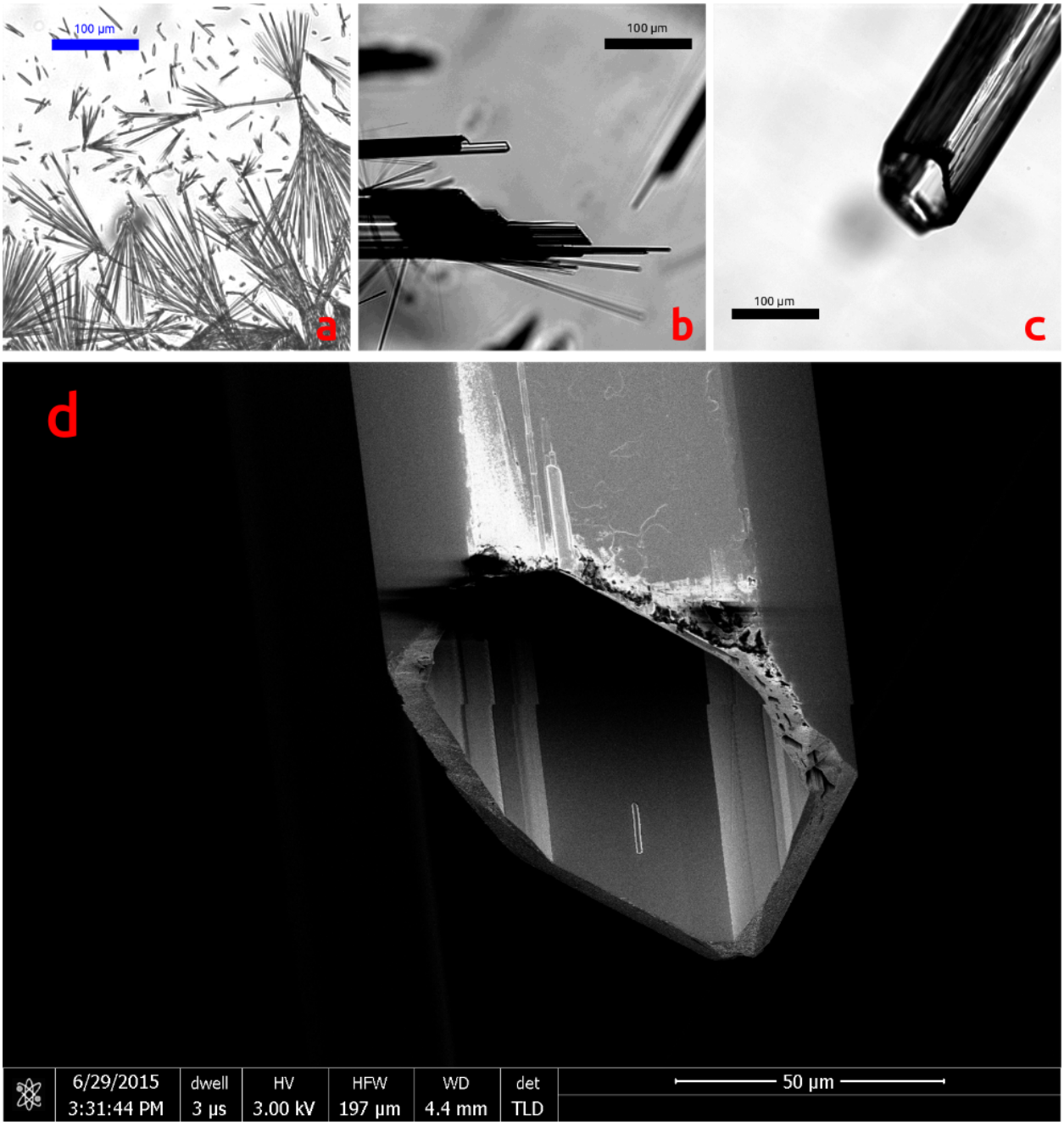

Figure 1.2: a) Uncontrolled growth from injection of stock solution into water. b) Growth face of mature crystal. c) Axial hollow core of an FF assembly. d) SEM image of an individual diphenylalanine crystal, demonstrating the hollow core and hexagonal cross section typical of crystals of the dipeptide.

group capable of disulphide bonding, C), glycine (achiral, residue a single proton, G) and proline (a cyclic secondary amine, the presence of which, in a chain, is conformationally very restrictive, P), there remain eight amino acids- alanine (A), valine (V), leucine (L), isoleucine (I), methionine (M), tyrosine (Y), phenylalanine (F), and tryptophan (W). Of these, the last three have aromatic side chains, while the others are simple alkyl (or thioether) chains.

The ordering of these residues within a chain, and its resultant effects on intra- and inter-molecular interactions determines the equilibrium structure of the protein, and it is from this form that function follows. In a very general sense, charged and polar residues tend to be exposed to solvent (the intracellular fluid, chiefly water), while nonpolar residues are found in "buried" positions in a natively folded polypeptide. Nonpolar residues do not establish the favourable intermolecular interactions with water that the polar residues can- they are limited to weaker van der Waals-type interactions. Their presence is disruptive to water structure, leading to a propensity for hydrophobic species in an aqueous environment to aggregate, limiting their solvent-exposed surface area.

1.1 Hydrophobicity and the hydrophobic effect

The hydrophobic effect is the name given to the observed tendency for nonpolar species to aggregate or desolvate when placed in a polar solvent, nearly always taken to be water. An analysis due to Kauzmann [16, 17] is based on evaluation of the chemical potential of a hydrocarbon solute on transfer from water to a nonpolar solvent, or vice versa. The chemical potential is given in this analysis in terms of mole fractions, that of the solute being assumed to be small, as $\mu_s = \mu_s^\circ + RT \ln X_s + RT \ln a_s$, for μ_s the chemical potential in solvent s, and X_s the mole fraction of the solute.

An analysis based on free energies of transfer relies on the energy required to make a "hole" in a highly associated solvent system (thus breaking hydrogen bonds) and the energy

released by filling it with either a species with strong interactions with water (tending to be favourable, solubilising the species) or with no strong polar interactions, resulting in a lower release of energy (only van der Waals type interactions exist) and a solubility equilibrium lying far to the left.

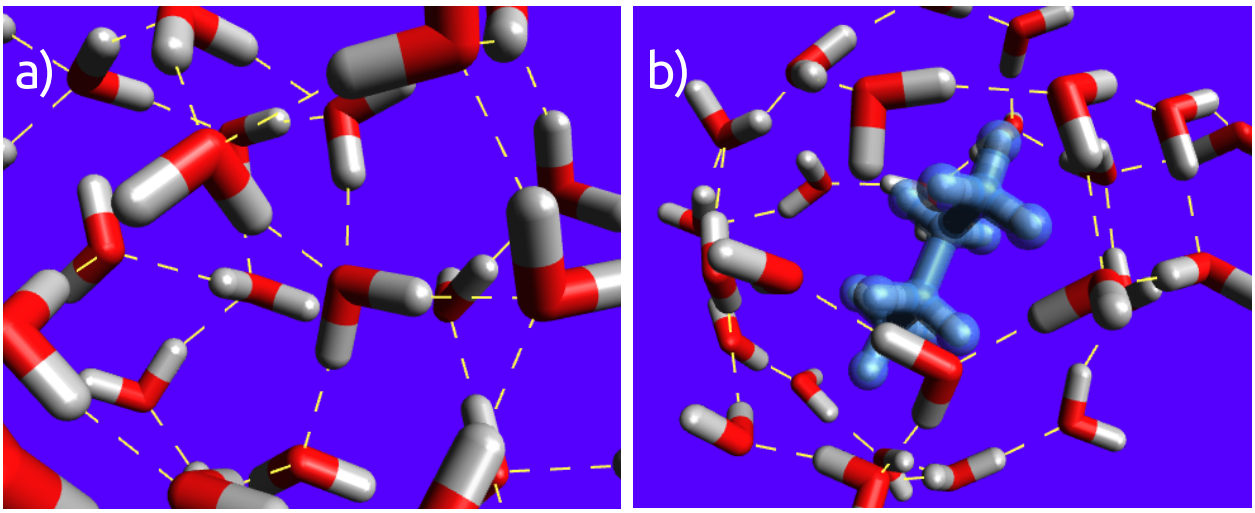

Figure 1.3: a) An intact network of hydrogen bonds in pure water b) An example of hydrophobic hydration of butane. Rendered in Avogadro 1.0.3[18]

Focusing on the equilibrium between intact and disrupted hydrogen bonding in the solvation shell around the species is at the root of an empirical analysis by Muller [19]. The equilibrium $\mathrm{H{-}O{-}H\cdots OH_2} \rightleftharpoons 2\,\mathrm{H_2O}$ is governed by the thermodynamic relation $\Delta G_b = \Delta H_b - T\Delta S_b = -RT \ln K_b$. The thermodynamic values- the enthalpy and entropy of breaking an intact hydrogen bond, are found to be dependent on the immediate presence of hydrophobic species- these values, ΔH_h and ΔS_h, vary slightly from those in bulk water. It was found by Muller, and corroborated by Graziano [20] that while the bonds in this hydration shell have a greater enthalpy of formation, the equilibrium is shifted to the right, resulting in a greater proportion of broken hydrogen bonds between the water molecules in direct contact with the hydrophobe.

The entropic and enthalpic signature of small-molecule hydrophobicity is a free energy of solvation that is composed of a favourable enthalpic (from intermolecular interactions)

and an unfavourable entropic (reduction in the number of energetically favourable conformations available to the water molecules in the presence of the hydrophobe). This effect is reversed at high temperature, where the entropic contribution becomes favourable (an entropy of mixing) while the enthalpic component becomes unfavourable. The variation of the enthalpy of solvation with temperature is a heat capacity [21], this being historically [22] (and erroneously [23, 19]) attributed to a region of highly ordered, ice-like water surrounding the hydrophobe in solution.

Such behaviour can be seen in the solubility behaviour of diphenylalanine (the simplest aromatic dipeptide) with increasing temperature, as in chapter 3. The free energy of solvation remains relatively unchanged, however, indicating an entropic contribution to the free energy that is nearly equal in magnitude and opposite in sign. This compensation is thought to arise mainly from the effect of the hydrophobic substituents on the surrounding solvent [24], and this compensated relationship is diagnostic of the influence of the hydrophobic effect [19].

1.2 Attractive forces between molecules

All molecules, with the exception of similarly charged ions, experience attractive intermolecular interactions. As was outlined previously, this includes hydrophobic species and water- why, then, do hydrophobic species desolvate and aggregate? A force clearly operates on the individual molecules, but this force is generated more by the solvent environment than by any specific interaction of the species themselves [22]. There does exist an interaction potential due to van der Waals forces that is attractive in nature, having a short range minimum (U) at a distance roughly equal to their molecular diameter (d).

The free energy change on associating two hydrophobes in aqueous solution can be approximated by following the thermodynamic cycle of transferring them to the gas phase, bringing them together, and re-immersing them in solvent [25]. This gives a free energy

change on dimerisation of two hydrophobic molecules in water (bringing them to a separation of d): $\Delta G(d) = \Delta\mu_{ss} - 2\Delta\mu_s + U(d)$, for $\Delta\mu_{ss}$ the chemical potential of the dimer in aqueous solution, $\Delta\mu_s$ that of the monomer and $U(d)$ the interaction energy at distance d.

and a mean force on the particles that is simply the gradient of the free energy with respect to distance between the particles, $F_r = \delta\Delta G(r)/\delta r$. The force has contributions both from the pairwise interaction energy U and from the effect of the presence of solvent. It is worth mentioning that the strengths of attractive intermolecular forces typically decrease rapidly with distance, and generally lower-order association is not seen in dilute solutions of hydrophobic species.

At a certain point, as the concentration of the hydrophobic species increases, the chemical potential of the hydrophobic monomer exceeds that of the hydrophobic species surrounded by other identical molecules. This is the criterion for thermodynamic stability of a solution of a hydrophobe, and is referred to as the critical concentration, c^*. Above this point, phase separation is favoured into an aqueous phase at the critical concentration (although this varies with the number of molecules in the new phase due to surface effects), and an oil phase. This can be expressed as:

$$\Delta\mu = \mu_{HC} - \mu_{aq} = kT \ln \frac{c}{c^*} \tag{1.1}$$

At equilibrium, and considering surface effects acting over an surface area of the new phase A with energy per unit area γ, the free energy of the system is given by:

$$\Delta G = \mu_{aq} dn_{aq} + \mu_{HC} dn_{HC} + \gamma dA = 0 \tag{1.2}$$

which can be expressed as a sum of contributions from the aqueous phase and the new phase, the free energy change due to the new phase, formed from n hydrophobic molecules being:

$$\Delta G = -n(\mu_{aq} - \mu_{HC}) + 4\pi r^2\gamma \tag{1.3}$$

Expressing n in terms of the size of the spherical nucleus for molecular volume V_m ($4\pi r^3$ / $3V_m$), we get the familiar relation for free energy change on cluster formation:

$$\Delta G = -\frac{4\pi r^3}{3V_m}(\mu_{aq} - \mu_{HC}) + 4\pi r^2\gamma \tag{1.4}$$

Apparent from this relation is a favourable free energy of aggregation dependent on aggregation number n, corresponding to nearest-neighbour interactions in the new phase (assumed invariant w.r.t droplet size), and an energy cost, varying as $n^{\frac{2}{3}}$ due to the surface. This leads to the concept of a "critical nuclear size", the point at which the free energy of cluster formation, plotted against aggregation number, reaches a maximum, any further additions to the cluster after that point lowering the free energy of the cluster, which then tends to grow.

1.2.1 Hydrophobicity and surfaces

The magnitude of the interaction, even judged by the simplification above (the creation of a new interface), can be expected to be a function of the surface area of the hydrophobic species. The greater the extent of this surface, the greater the entropic cost due to restriction of the varying water conformations (which is slightly compensated by a greater negative enthalpy of hydrogen bond formation). In the simplest case, that of the linear alkanes, a linear relationship between the surface area of the alkane and its free energy of solution in water, either from the gaseous or liquid phase [26] is observed. For solution of the vapour, the free energy for a carbon chain N carbons long is $\Delta G_s(g \rightarrow aq) = 23.9 + 0.74N\ kJ/mol$. The same study [26] also gives the enthalpies and entropies of solvation- the enthalpy change of the gas to solution transition is $\Delta H_s(g \rightarrow aq) = -14.1 - 2.81N\ kJ/mol$, a favourable enthalpy reflecting the establishment of water-alkane and stronger water-water interactions, and an entropy penalty of $\Delta S_s(g \rightarrow aq) = -128 - 11.9N\ J/mol/K$.

The extent to which the concept of an interface applies to single solvated molecules is dubious, however- the presence of small hydrophobic species such as alkanes is not necessarily as restrictive to the hydrogen bonding arrangement of water as is a surface with low curvature on the molecular scale (for example, the surface of an oil droplet) [27, 28, 29, 30]. For solutes, radius λa in a solvent (spheres of radius a), the probability of finding a cavity of size λ, $P(\lambda) = \exp \frac{-W(\lambda)}{kT}$, where $W(\lambda)$ is the work required to create the cavity. $W(\lambda)$ depends on

the density of solvent and its distribution through the relation $W/kT = 4\pi\rho a^3 \int_0^\lambda \lambda'^2 G(\lambda')d\lambda'$, for a density of solvent molecules at distance λ given by $\rho G(\lambda)$. The precise form of G(λ) is complex and solvent dependent generally, but for solutes less than half the diameter of the solvent spheres, the relation is very simple, $W = -kT\ln(1-(4\pi\rho a^3/3)\lambda^3)$. As λ increases (a larger solute), higher order terms appear, in particular, a surface tension term. Neglecting pressure changes, this works out as $W(\lambda) = (4\pi\gamma a^2)\lambda^2 - (16\pi\gamma a/R_c)\lambda$. The first term is recognisable as a familiar form of the surface energy, with the second (curvature-based) being identifiable with the Laplace pressure.

This would indicate that hydrophobic aggregation proceeds in two different regimes, depending on whether the hydrophobic species is small or large, relative to water [27]. For large assemblies, which may be formed by the progressive addition of small hydrophobic species, a definite "surface" can be said to form due to the larger radius of curvature completely disallowing the formation of hydrogen bonds, after the fashion of the air-water interface, and the aggregation process is thenceforth described by classical nucleation theory.

Nucleation and growth of a hydrophobic aggregate is a phase separation process, resulting in one (or more) new interfaces, which are high energy features, counterbalanced by a favourable "bulk" energy, arising from interactions within the hydrophobic region, and also, importantly, from the desolvation of hydrophobic species present at above the concentration in water that can exist in the presence of the aggregate.

The free energy of nucleation is related to the free energy of transfer of a hydrophobic species from water to its pure phase, the relationship being of the form $\Delta G = -4/3\pi r^3(\mu_{HC} - \mu_{aq})/V_m + 4\pi r^2\gamma$, with μ_{HC} and μ_{aq} the free energy of the species (molecular volume V_m) in the non-aqueous (hydrocarbon) phase and aqueous phase respectively. The Laplace pressure is omitted here. This simple relationship gives rise to a maximum in the relation of nucleus energy to size, a point which will become important in mechanistic discussions of diphenylalanine aggregation in chapter 2.

1.3 Intermolecular forces

The intermolecular forces governing hydrophobic interactions are entirely due to electronic distribution. Electrostatic forces exist between charge distributions, and are highly orientation dependent. Induced charge phenomena are due to the effects of neighbouring molecules on the electron distribution of a molecule- they are always attractive. The dispersion force is a non-classical phenomenon arising from the correlation of the relative motions of electron clouds and nuclei in the interacting species. It is always attractive, and always present.

In the previous discussion of polar and non-polar species, we separated the interactions into those between polar species (for example, water and the arginine side chain), those between a polar and a non-polar species (such as the interaction between water and the phenylalanine side chain), and those between non-polar species. While all are attractive forces, arising from the motion and density of electrons, they vary in strength (hence the hydrophobic effect). Molecules that are considered polar, broadly speaking, are those which display a permanent unequal charge distribution, that is, regions of high and low electron density.

It is easy to see that there must be a highly directional component to electrostatic intermolecular forces, with the exception of the spherically symmetric isolated charge. It is from this that the concept of water "structure" springs, and, due to the strength and the directionality of interactions between permanent dipoles, they play a significant role in biological self-assembly processes. Particularly of interest in pathological processes of protein misfolding is the role of polyglutamine repeats- the highly polar, though neutral, primary amide of the glutamine side chain is capable of forming strong hydrogen bonds with other glutamine residues, stabilising β-sheet structures within fibrillar aggregates [31, 32], even in the absence of water (i.e. in buried regions of the aggregate).

Interactions between hydrophobic species, however, are typically far weaker than hydro-

gen bonds and similar charge phenomena. They have a considerable effect on the folding and conformation of proteins due to the fact that the solvent is water, and therefore polar in its own right. Polar residues, for example glutamine, can easily satisfy hydrogen bonding with the surrounding (or indeed trapped) solvent. Burial of hydrophobic residues by the adoption of a folded form, in which the hydrophobic residues interact more with each other than with the solvent, is favoured by the effect of these residues on water and vice versa.

Desolvation of hydrophobic species is a major driving force in protein folding for precisely this reason- however, the internal dynamics of the folded or aggregated polypeptide chain does not resemble a liquid in hydrophobic regions, except as a fleeting intermediate during folding (a state described as a "molten globule") [33, 34]. Hydrophobic residues have been hypothesised to play a key role in the initial adoption of a natively folded structure- this is the "hydrophobic collapse" model, in which desolvation, with or without secondary structure formation is on the main folding pathway [35, 36]. It is also noted that the non-surface residues typically pack extremely closely in their native state- the packing efficiency in some cases being found to be as high as in organic crystalline solids [37].

There is, therefore, a well-defined inner structure in hydrophobic regions, arising from both the steric (short-range repulsion potential) and electronic properties of the hydrophobic species themselves. While alkyl groups chiefly only vary in their shape (and thereby the volume they exclude/surface area they make available for intermolecular contacts), there remain three amino acids with a distinctive electron distribution and hence directional, rather than simply steric, structural effects. These are the aromatic species phenylalanine, tyrosine, and tryptophan.

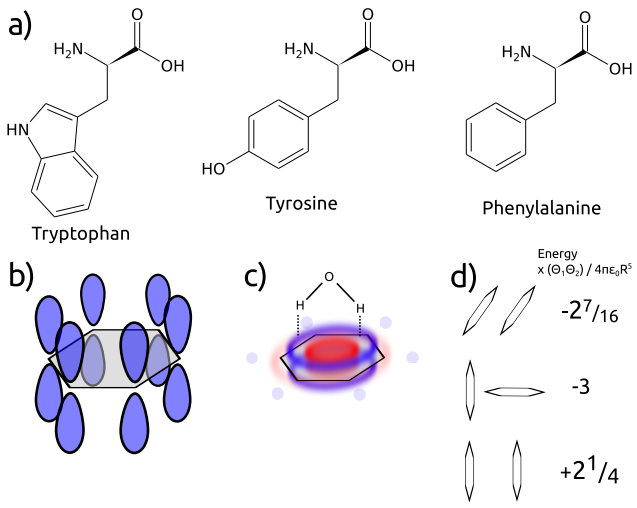

Figure 1.4: a) Aromatic amino acids tryptophan (W), tyrosine (Y) and phenylalanine (F). b) Atomic orbitals contributing to the delocalised pi system. c) Illustration of benzene quadrupole, with water molecule in most stable position for the benzene-water dimer [38]. d) Arrangements of benzene rings and their energies in terms of the quadrupole interaction, after Stone [39]

1.4 Aromaticity and the hydrophobic effect

Aromaticity is a phenomenon by which certain ring systems display an enhanced stability to any reaction that would disrupt the presence of a continuous electron density on each "face" of the planar ring. The molecular orbitals occupied by these electrons all have π-symmetry, with a node in the plane of the ring. Both homocycles, such as benzene, and heterocycles such as indole, display aromatic character, but the presence of heteroatoms perturbs the orbital energies and typically renders the species more polar and more reactive.

Simple hydrocarbon aromatic species such as benzene or toluene are well-known and display a limited water solubility, as might be expected. There is, however, a discrepancy between the magnitudes of the hydrophobic effects acting on simple alkanes and aromatic hydrocarbons- aromatic species are significantly more soluble in water than alkanes of comparable hydrophobic surface area [40, 41]. Aromatic species do display variable electron density, and hence some "polar" behaviour- the poles in this case being electrical quadrupoles capable of interacting with water dipoles to a small extent.

These quadrupoles have further implications for the packing behaviour of aromatic species, if and when the aromatic substituents are desolvated. Quadrupolar interactions are at the root of the "herringbone" packing of aromatic species that is observed in solid benzene, and interestingly a very similar motif occurs in the crystals of diphenylalanine [1].

1.5 The crystal habit of aromatic peptides

The equilibrium shape of a crystal is defined (ideally) in terms of the energies of its faces. High energy faces, as defined by the chemical potential change on addition of monomer, grow more quickly than do lower energy faces. This result has been known for over a century, first being expressed by Josiah Willard Gibbs [42] and Georg Wulff [43] in variant forms. The theorem of Gibbs stated that a crystal in its equilibrium form occupied an energy minimum such that:

$$\Sigma_j \gamma_j \delta O_j = 0 \tag{1.5}$$

for a closed polyhedral crystal with faces of areas O_j and surface free energies γ_j, the surface free energies per unit area being assumed constant with variation in crystal size. The Wulff statement related the energy of crystal faces to the distance h_j parallel to the normal of the face from the centroid of the crystal:

$$h_j = k \cdot \gamma_j \tag{1.6}$$

A full proof is given elsewhere [44, 45], but it is important to note that the Gibbs-Wulff theorem, whatever its form, really only applies at very small lengthscales- crystals very soon after nucleation or at the last stage of dissolution. Strickland-Constable demonstrates this as follows- as an equilibrium crystal increases in size, the areas of the faces are, through some geometrical constant of proportionality, related linearly to the square of the normal distance from the centroid:

$$O_j = g_j h_j^2 \tag{1.7}$$

allowing the Gibbs equilibrium criterion to be written as:

$$\Sigma_j \gamma_j d(g_j h_j^2) = 2\Sigma_j (O_j dh_j)/k \tag{1.8}$$

which, taken together with the expression for chemical potential change on crystallisation $\Delta\mu_{cryst} = (\frac{\delta \Delta G_n}{\delta n}) = kT \log(c/c*)$ gives an excess chemical potential in the crystal nucleus of $\Delta\mu = 2V_m/k$,

where V_m is the molecular volume and n the number of molecules in the aggregate- a result exactly analogous to the Thomson relation for liquid droplets. As such, it is to be expected that the Gibbs-Wulff theorem will only predict a significant driving force for crystal habit in the very early stages of crystal growth after nucleation. For larger crystals, as noted in reference 45, the change in chemical potential on the addition of a new layer of molecules to a crystal face is dominated by the chemical potential difference required to trigger surface nucleation (in the absence of crystal defects that may cause addition sites to exist that are inherent to the face).

The advance of a crystal face occurs in discrete steps, corresponding to the "height" of an incorporated monomer along the face normal. The requirement for stability of an adsorbed monomer on the surface is typically that it be coordinated by other monomers in the same new layer- this leads to a cooperative, nucleation-dependent growth regime, where the free energy change to start the growth is far greater than the energy required to add the same number of monomers to a partly-covered face, a theme that will be explored in chapter 2.

It should be mentioned, in light of the above discussion of the Gibbs-Wulff theorem and its limitations, that the small nuclei that give rise to the deposition of a new layer are, in terms of size, well within its remit. The free energy change on formation of a stable nucleus on a crystal face is very much affected by the nature of its edges, in two-dimensional analogy to the faces of a three-dimensional crystal. Variations in the edge energy between different crystal faces will strongly affect the rate of nucleation on those faces and hence the rate of growth normal to that face, all other things being equal.

An interpretation of the shapes of crystals is given by Hartman and Perdok [46, 47]- they state that crystal habit is chiefly determined by the presence of "chains" of strong bonds at the unit cell level, described as periodic bond vectors. In the case of the crystals of the dipeptides, these are the C(8) (C(16) in methanol solvate) and to a lesser extent the C(4) and C(5) hydrogen bonded chains. This is certainly observable in the needle-like crystals of FF, where the bonds along the long axis of the crystal are helical hydrogen bond chains, and the radial bonds in the short dimensions of the crystal are mainly dependent on hydrophobicity, generally a far weaker interaction than the hydrogen bond, even in aqueous solution.

Hartman and Perdok's analysis divides crystal faces into F, S and K faces, depending on the number of periodic bond vectors in the plane of the face. Defined for the simple cubic crystal, F (flat) faces have two periodic bond vectors in the plane of the face, S (stepped) have one, and K (kinked) have zero, the F faces growing the slowest and thereby dominating the final surface of the crystal. "Chains" of bonds along a lattice vector are only as morphology-determining as their weakest link, which has implications for the segregated hydrophilic/hydrophobic structures of the hydrophobic and aromatic dipeptides.

1.6 Hydrophobicity in FF aggregation

Dipeptides represent the simplest "polypeptides" displaying an amide bond and charged termini- various studies on this dipeptide have been carried out as detailed in the following chapters, and comparisons were drawn to longer species. Notably, it represents the central motif of the amyloid beta polypeptides- this aggregation-prone protein, secreted in the brain, contains phenylalanine at positions 19 and 20 [48]. It is contained in the fragment KLVFFAE, itself capable of self-assembly into ordered fibrils [49], bound together in an antiparallel conformation stabilised by both charge-charge and hydrophobic interactions. The free dipeptide FF can be easily compared- both consist of oppositely-charged termini, with

hydrophobic R-groups on the amino acids in between. Tjernberg [50] found that polypeptides as short as tetrapeptides (KFFE, KVVE) were capable of forming amyloid-like fibrils, and Gazit investigated the role of the F side chain in amyloidogenesis [51, 4], with a focus on pi-stacking interactions as a driving force for aggregation. It was also proposed [52] that electrostatic interactions between oppositely-charged residues further increase the propensity of short sequences to form amyloid fibrils. The ability of short peptides to form amyloid fibril appears to be highly dependent on both the hydrophobicity of the side chains but also on aromatic-specific π-π interactions [4]. As the simplest possible aromatic polypeptide, with unblocked and oppositely charged terminal amine and carboxylate groups, diphenylalanine is an ideal model system to investigate in detail the relative importance of the different energetic contributions

Comparison of the thermodynamics of dipeptide and polypeptide aggregation is more than an interesting exercise- in these model systems, individual effects with differing thermodynamic or kinetic "signatures" can be isolated in a far simpler system, one which is very amenable to both in vitro and in silico experimentation. In the case of FF, and fragments or full-length proteins containing the motif, the desolvation of the benzyl groups is predicted to contribute a significant negative free energy to the process of amyloid fibril formation.

1.7 Overview of the thesis

In this thesis, I will show that FF can be said to demonstrate some of the chemical principles underlying the aggregation of longer polypeptides. FF aggregation displays the energetic signature of hydrophobic desolvation, and I will explain its unusual crystal habit in terms of the relative strengths of hydrophobic and dipole-dipole interactions and hydrogen bonds. Conversely, I will show that FF cannot be said to be a model system for amyloidogenesis. Mechanistically, the processes occurring as a solution of FF ($A\beta_{19-20}$) and the full length

$A\beta_{1-40}$ separate into an aqueous phase and an aggregate phase are quantitatively and qualitatively very different.

In the first part of the thesis, I establish the growth kinetics of FF as a function of solution supersaturation, in terms of the elongation rate of the needle-like crystals and also in terms of their increase in radius. The elongation and radial growth rate are described in terms of theories of crystal growth, in a paradigmatic shift from earlier conceptions of the aggregation of short polypeptides. The growth rates are continuous functions of the solution supersaturation, in accordance with the predictions of existing theories of crystal growth, in contrast to the rather less predictable thickening processes of amyloid fibril. The growth rates are used to derive a mechanism for the aggregation of FF, one that is found to be based on cooperative (multi-molecular) processes occurring at the growing face. Addition of FF to its aggregate occurs by a mechanism that involves nucleation of new layers on a surface- in the amyloid paradigm, the processes of secondary nucleation and of elongation of fibrils are kinetically and mechanistically distinct in vital ways.

I further explore the thermodynamics of FF aggregation in light of the amyloid paradigm of marginal stability of full-length polypeptides in nature. Previous work demonstrated approximate power-law relationships between polypeptide chain length and the free energy of aggregation (per peptide unit). In order to extend this theory to the highly heterogeneous dipeptides, I devise and apply a measure based on hydrophobic surface area to contextualise the free energy of aggregation. In these terms, highly hydrophobic FF can be considered an extension of the scaling laws to the shortest possible chains. I extend the investigation to analysis of the barriers to incorporation of FF into its aggregate. Longer polypeptides show remarkably compensated transition states- that is, the incorporation process passes through a low entropy, high enthalpy intermediate. Interestingly, this is the result of the barrier analysis for FF, but the mechanisms involved in the incorporation are markedly different.

At the beginning of the project, FF was already more than a model system. It had been explored in a variety of applications, and in this thesis I establish and demonstrate a

method for the continuous growth of FF crystallites without alteration of diameter. Materials science applications are further explored in my role in the investigations into an N-terminally substituted variant of diphenylalanine, one which displays a remarkable polymorphism. One polymorph is rapidly formed, glassy in structure and having extreme mechanical stiffness. I establish that it is labile in suspension following formation, and undergoes an Ostwald ripening process on a timescale of minutes. I rule out the possibility of its coagulation from suspension as a route to the thermodynamic product. The thermodynamic product, the second previously known polymorph, is crystalline, displaying long range order and is the thermodynamic product of the aggregation process. I present the discovery and partial characterisation of a new, previously unrecorded, polymorph of the substituted dipeptide and a protocol for its preparation. I conclude that the multi-stage aggregation process in BocFF is an example of Ostwald's step rule, a principle that may also be applicable in the early stages of amyloidogenesis. This stands in contrast to FF, for which no short-lived oligomeric species have been detected.

Extending the materials science applications of the dipeptide, I present a previously unknown polymorph of FF aggregated from its solution in methanol. This polymorph is also a solvate, incorporating methanol on defined lattice sites as the water-grown crystal does, but there is no void or channel in the unit cell. What is observed, however, is the β-sheet connectivity of the central amide bonds that is typical of amyloid fibril- a feature that is absent in the crystals of FF as precipitated from water, and one that is critical to any classification of a structure as 'amyloid'. The polymorph is, however, crystalline, and is fully characterised by X-ray diffractometry. I survey the solubilities of FF in a range of familiar solvents and note a number of potential new systems that could be employed by nanotechnologists working on the dipeptide, in particular, acetic acid- a readily available solvent for use in stock solutions. The FF-water-acetic acid system is applied in an investigation into the osmotic triggering of high power-density chemo-mechanical actuators.

Taken together, my major conclusion is that FF and amyloid fibrils are simply different systems, this difference arising from the three-dimensional crystalline order of the dipeptide

in its aggregate state, and conversely (to a lesser extent) its lack of structure in solution. Thermodynamic measurements demonstrate hydrophobic hydration of the dipeptide in solution, and conformity with hydrophobicity-based trends among short polypeptides, some of which are fibrillar in the aggregate state. In common with amyloid fibril, the addition process is thermally activated, but mechanistic differences render direct comparisons problematic. A similar conclusion may be drawn about the multi-stage assembly of BocFF, where clear analogies can be made between on- and off-pathway oligomerisation in the dipeptide and amyloid, and the application of the step rule that governs BocFF aggregation to fibril assembly. These are analogous, but mechanistically distinct processes.

Where the dipeptide and its derivatives are most applicable must be as materials, rather than as model systems from which conclusions may be drawn about the aggregation and propagation of amyloid fibrils. Two solvomorphs are now known and structurally characterised, and their ease of preparation and scale of their assemblies permits them to be applied in micromechanical systems.

Chapter 2

Kinetics of the self-assembly process

2.1 Introduction

Polymers that are formed through non-covalent interactions between the building blocks have been shown to possess a range of advantages over conventional polymers, such as easy processability and self-healing [53]. If the building blocks are based on peptides, the resulting aggregates can possess biological functionality [54] and be biodegradable. Short peptides can assemble into filamentous, as well as crystalline solid phases; in some cases a given sequence can assemble into both types of structures, depending on the solution conditions [55]. In particular aromatic dipeptides have been found to be capable of self-assembling in aqueous solution to form highly anisotropic nano- and microcrystalline structures that possess remarkable and potentially valuable physicochemical properties [1, 2]. In the case of diphenylalanine (FF), the simplest aromatic dipeptide, these microcrystals are often characterised by central voids parallel to and coaxial with the long axes of the crystals [3, 56], though it has been shown that solid rods can also be fabricated [57]. The crystal structure has been found

to be the same irrespective of the overall dimensions of the crystal [58, 59] for diameters above 100 nm, and to display a channel containing associated solvent molecules [1, 56].

Early investigations into the self-assembly of diphenylalanine were stimulated by the discovery that the phenylalanine residue had a significant effect on the stability of aggregates formed from hexa- and pentapeptide fragments of the human islet amyloid polypeptide, hIAPP(22-27) and hIAPP(23-27) [60]. These species self-assembled in solution into amyloid fibrils displaying characteristic morphology [61], but mutation of the F residue of hIAPP(22-27), which has the native sequence NFGAIL abolished the formation of any fibrillar structure.

It was observed that the kinetics of aggregation of NFGAIL and FGAIL were characteristic of a nucleation-based mechanism, displaying significant "lag phases" that were not present when seeds, preformed aggregates of the peptide, were introduced to the solution. The presence of these seeds avoids the kinetic barrier presented by primary nucleation[1] and the reaction kinetics are thereafter dominated by other processes [62].

The fact that it was demonstrated that the phenylalanine residue had such a significant effect on the hIAPP derived peptides prompted further research into the possible role of phenylalanine specifically [4] in the processes of amyloid formation and deposition. Around the same time, it was observed that still shorter polypeptides, the designed tetrapeptides KFFE and KVVE, were capable of organisation into fibrillar structures stainable with Congo red and displaying β-sheet like structures in solution, as detected by circular dichroism [50]. This remarkable aggregation behaviour, ascribed to sequence-dependent β-sheet propensity and terminal charge-charge interactions led to investigation of the dipeptide as a still-simpler model system for the amyloid fibril.

The mechanisms leading to the propagation of amyloid aggregates *in vivo* are of major

[1]This nucleation process, the initial phase separation from a homogeneous solution to a single, stable particle of the new phase, is referred to in protein biophysics as primary nucleation, and in crystal growth theory as homogeneous nucleation.

concern in the treatment of amyloidoses, the broad family of diseases characterised by the misfolding and phase separation of proteins in living systems. Amyloid fibrils are low-energy states, typically far more stable than the famously *metastable* globular forms of the proteins, which are typically the functional form of the protein [63]. The processes of amyloidogenesis and propagation are the product of four kinetically distinct phenomena- elongation, the addition of a monomer to a fibril; primary nucleation, in which local fluctuations in a homogeneous solution of monomer result in formation of a new phase; secondary (heterogeneous) nucleation, in which monomers bound to a fibril surface interact to form a new growth-capable nucleus; and fragmentation of an aggregate to yield additional growth-capable sites [64, 65]. These processes are kinetically distinguishable in the bulk, and the micrometer-range diameter of the fibrillar structures formed by FF gives a potential opportunity for direct growth measurements on an analogous system, should the aggregation process be comparable.

A wide range of studies have explored possible nanotechnological applications of supramolecular assemblies of FF and its derivatives [66], resulting in their surface decoration [67, 5] and the fabrication of metal nanowires [5], biosensor electrodes [68] and optical waveguides [69]. As a structural building block, such micro- and nanoscale peptide structures are very promising, as they are easily prepared, thermally stable [10] and possess other unexpected qualities such as piezoelectric behaviour [14] and high mechanical strength [8]. Nevertheless, while many of the remarkable properties of the various dipeptide assemblies have been characterised in detail, little is known about the mechanisms by which they self-assemble. Such mechanistic information would be of considerable value as it could lay the foundations for systematic control of the assembly processes.

In this chapter, I develop and demonstrate an approach for this purpose that is based on a microfluidic flow-reactor, and enables the use of time resolved optical microscopy to quantify independently the axial and radial growth rates of crystalline assemblies while controlling the chemical potential of the peptide building blocks in solution. Furthermore, it is possible to vary rapidly the solution conditions under which growth occurs, as a result of

the small volumes of reactants that are used in this approach and the predictability of the flow properties within the reactor.

These results reveal that the growth of FF microcrystals occurs through the nucleation and spread of monolayers on the growing faces of the crystals [70, 71]. I show in addition that the varying ratio of axial-to-radial growth rates, resulting from a difference in edge energy between axial and radial nuclei, can be exploited to establish routes to design tubular FF aggregates with controllable aspect ratios, beyond the thermodynamic products.

2.2 Results and discussion

2.2.1 Kinetics of FF aggregation measured in a microfluidic flow reactor

At the beginning of the project, the standard method of preparation of FF assemblies was by rapid dilution in water of a concentrated stock solution in a high-capacity solvent, the fluoroalcohol hexafluoroisopropanol (HFIP). Solutions were prepared in HFIP at 100 mg/ml, and were then injected rapidly at a ratio of 1:50 into water, leading to instant precipitation of tubular microstructures [10, 72]. A micrograph of the results of this process is shown in figure 1.2a. It was also known that the dipeptide displayed greater solubility at higher temperatures, and that FF would be precipitated from a concentrated aqueous solution cooled to room temperature [1, 73].

A preliminary experiment was designed to prepare a reproducible system for the dilution of stock solutions of HFIP, in the hopes of observing the early stages of the self-assembly process and potentially obtaining suspensions of FF assemblies with low polydispersity. A

microfluidic mixing device was used for this process, prepared using a soft lithography process [74, 75].

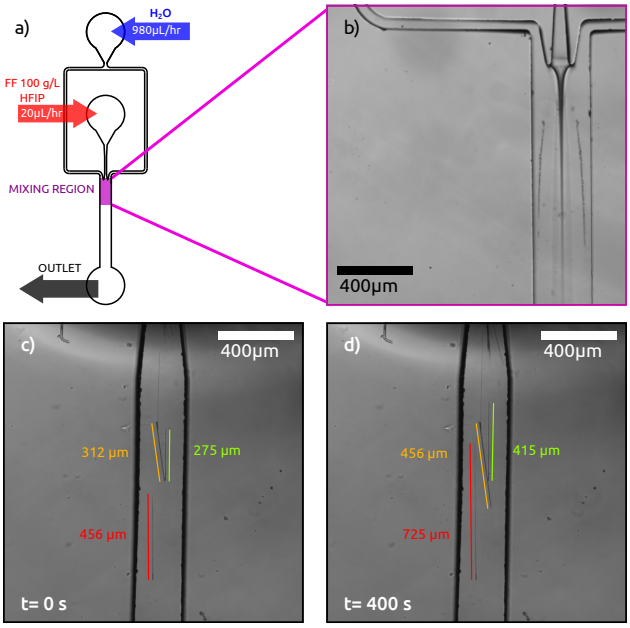

Figure 2.1: a) Schematic of the device used. A syringe pump was used to inject water at 980μL/hr into the outer channel, simultaneously with a stock solution of 100g/L FF in HFIP at 20μL/hr into the central channel. The region where the flows met was observed. b) Junction region of a device with 300μm channel, showing non-turbulent flow. HFIP is in the central channel, and a "halo" of FF precipitate is visible as dark lines, these lines representing the point at which mutual diffusion of the three components and surface-catalysed precipitation results in precipitation of FF. c) Device with 250μm wide channel that has been pre-injected with seeds via the outlet. The images are taken near the outlet, where precipitation is reduced. d) 400 seconds later, growth of the three seeds is evident. The assembly highlighted in red has grown by 268 microns, while the yellow and green highlighted assemblies have grown by 143 and 140 microns respectively.

Two-phase devices such as those shown in figure 2.1 presented a number of problems. Most notably, the flow in a microfluidic channel operates in a low Reynolds number regime where mixing of the phases occurs through diffusion and not through turbulent flow [76]. As a result, there is a significant variation in the concentration of each of the three components

across the channel width, leading to variations in the solvent conditions (HFIP solubilising the dipeptide, water tending to precipitate it) and indeed variations in FF concentration across the channel. This is visible in the symmetric precipitation of small FF deposits on the surfaces, the distance from the channel centre varying as the components mix, leading to variations in concentration profile across the channel length.

However, figure 2.1c and d give the results of experiments where, prior to introduction of the flows of HFIP and water, the mixing channel was injected with a suspension of pre-formed FF assemblies. In these images, taken closer to the outlet, where the concentration gradients of each solution constituent are less steep, nucleation is not observed, but there is clear evidence of the axial growth of the assemblies. One grows nearly twice as fast as the other two, a phenomenon perhaps due to the lateral placement of the growing ends of the assembly within the channel.

The dipeptide is readily prepared as a metastable solution, in a fashion similar to solutions of larger proteins. Longer polypeptide chains capable of forming amyloid fibrils are typically soluble in the globular state at concentrations far exceeding the concentration of protein that would exist in equilibrium with such species (the critical concentration) [63]. The critical concentration of FF was measured and found to be 0.76 g/L, measured from the supernatant of an aqueous solution that was allowed to aggregate.

I employed a simple flow cell arrangement (2.2a) based on the use of a simple metastable solution rather than an HFIP dilution step, consisting of multiple inlets and a large central chamber with support pillars, which allows the growth kinetics of individual crystalline FF assemblies to be measured via optical time lapse microscopy (2.2d). The flow reactor was used to expose the injected, pre-formed seed crystals (2.2b) to a flow of solution at a series of constant supersaturation levels (2.2c), leading in each case to a distribution of observed growth rates. The growth solutions were maintained at high temperature to avoid nucleation prior to injection, and the aliquots used for the test runs were extracted and equilibrated rapidly to room temperature.

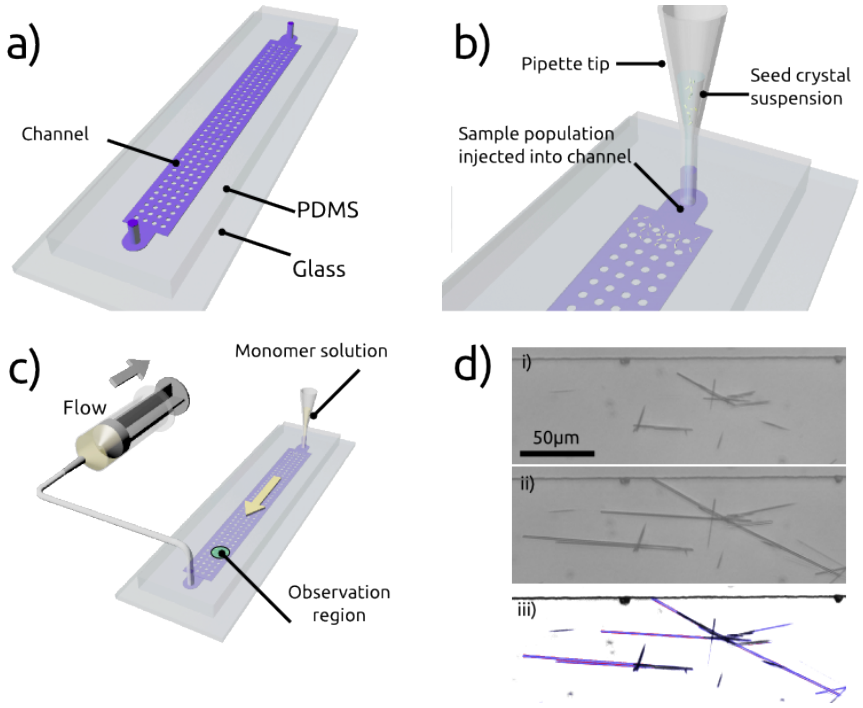

Figure 2.2: The study of the aggregation kinetics of FF developed in this work using a microfluidic flow reactor. The schematic diagrams illustrate: a) The reactor itself prepared through soft lithography [74]. Channel dimensions are 17 mm length, 25μm in height and 1000μm in width. b) A suspension of seed crystals is injected into the reactor. c) A supersaturated solution of FF is drawn through the channel by means of a syringe pump at a rate of 800μl/hr. d) A series of images separated by fixed time periods are taken via optical microscopy and changes in the dimensions (blue) are recorded. The growth rate is then computed from the five fastest growing crystals in the observation region.

Observation of dissolution processes using this setup suggested to me a significant "off rate", a rate at which monomer left the aggregate and returned to solution, a phenomenon known to occur with amyloid fibrils at far slower rates, such that kinetics are generally held to be linear [77] in monomer concentration. This led to the recording of growth rates as a function of the solution supersaturation ratio σ, defined as $\sigma = (c - c^*)/c^*$ with c^* the critical concentration. Thus, σ is a dimensionless parameter that expresses the ratio of the concentration c in a given experiment to that under equilibrium conditions, i.e. the critical concentration (for FF at T = $23°C$, its value is $c^* = 0.76$ g/L= 2.4 mM) [56]. The value of σ is zero when $c/c^* = 1$, i.e. when the growth rate of the (semi-infinite) aggregate is zero. The supersaturation ratio σ is related to the free energy of aggregation through the relationship:

$$\Delta G_\nu = RT \ln(c/c^*) = RT \ln(\sigma + 1) \tag{2.1}$$

where R is the gas constant.

2.2.2 Limiting rates in crystal growth

In order for this work to be broadly applicable to the growth of FF microstructures, and so that conclusions about mechanism on the crystal face rather than transport phenomena in solution can be drawn, it is necessary that limiting rates of growth must be found. These rates of growth must be independent of channel geometry, crystal number density in the channel or other extrinsic parameters. Only through establishing the maximum possible growth rate as a function of concentration can information be obtained about the processes involved in incorporation of monomer by growth rate studies. In the case of amyloid fibrils, a linear relationship between concentration (strictly, supersaturation) and growth rate, transitioning into a sublinear relationship due to growth site saturation, is a well-established phenomenon [78, 79, 77].

One parameter that had to be controlled was the rate at which FF could arrive from solution to the addition sites. If the limiting factor is diffusion through solution, then the

expected kinetics are linear in supersaturation- the "off rate" is proportional to the critical concentration, while the addition rate is proportional to the actual concentration in bulk, which gives rise to the concentration gradient. This process gives no information about the nature and rate of reactions occurring at the growth sites, as these are not the rate limiting step.

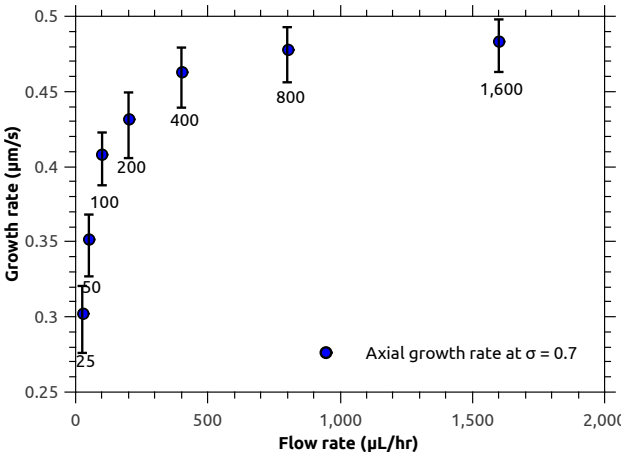

Figure 2.3: Variation of growth rate (at σ=0.7, 1.3g/L) with flow rate from 25 to 1600 μl/hr in this device. 800 was used in the rest of the study due to greater reliability and lower stresses on the device at the 800 as opposed to 1600 μl/hr. Error bars are range of five fastest growing crystal faces (from at least 25 crystals)

Figure 2.3 demonstrates a transitional region between diffusion dominated kinetics and a regime where the growth rate is independent of flow rate, corresponding to data points at 800 and 1600 μl/hr. 800 was used throughout the rest of the study due to increased channel distortion, leakage and interestingly extensive deflection of crystals under flow at the faster rate.

It is also necessary to address other extrinsic factors in the analysis. Deposition of the crystals by settling of suspensions of seeds may involve an electrostatic component. The crystals themselves are polar [15] and it is known that glass surfaces display a negative surface charge [80]. This electrostatic interaction may lead to occlusion of growth sites, and close association with the walls of a microfluidic channel may position the growth face in a region of relatively slow flow due to non-slip boundary conditions. As a result, nearly all crystals imaged during the investigation displayed a "fast" and a "slow" end. Other processes leading to inhibition of crystal growth on the scale of individual crystals include obstruction by growth into an obstacle, either a channel wall or another crystal, or obstruction of a growth

face by smaller dislodged crystals. Measurement error may also occur due to non-zero angles between the crystal and the imaging plane.

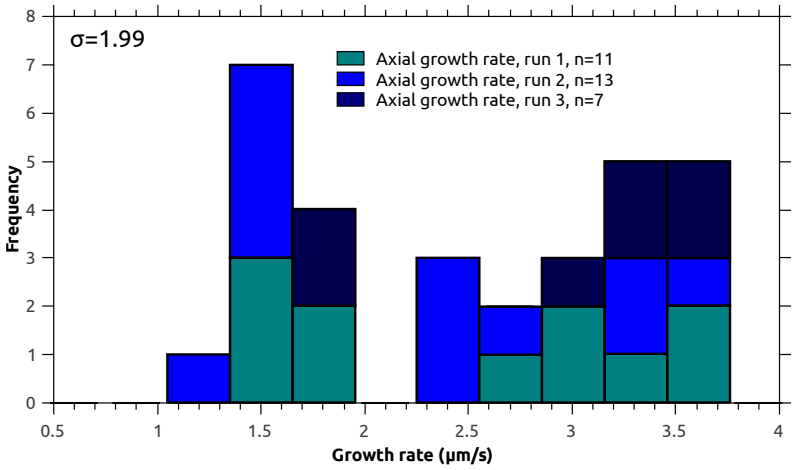

Figure 2.4: Distribution of growth rates at 2.27g/L FF in water. 3 runs, n = 31.

A distribution of growth rates from an experimental run is shown in Figure 2.4. Here the "slow" and "fast" ends are visible in the bimodal nature of the distribution (crystal faces not growing at all were not recorded), and there is an abrupt termination of the distribution at the fastest values. This is what is expected from an intrinsic limit to addition rates- regardless of channel geometry, flow rate, angle and random obstruction, monomer cannot be added faster to the growth face. The fastest growth rates, therefore, contain the information on mechanism sought in the investigation.

2.2.3 Measurement of growth rates

Figure 2.5 displays the maximum observed growth rates along the long axes of the crystals in units of μm/s. Vitally, the data in 2.5 reveal that there is a higher than linear dependence on σ of the axial growth rate (i.e. along the (100) direction, parallel to the long axis of the crystal. Measurements of growth kinetics were performed on single ends of individual crystals. The data points represent the average rate of the five fastest growing crystals,

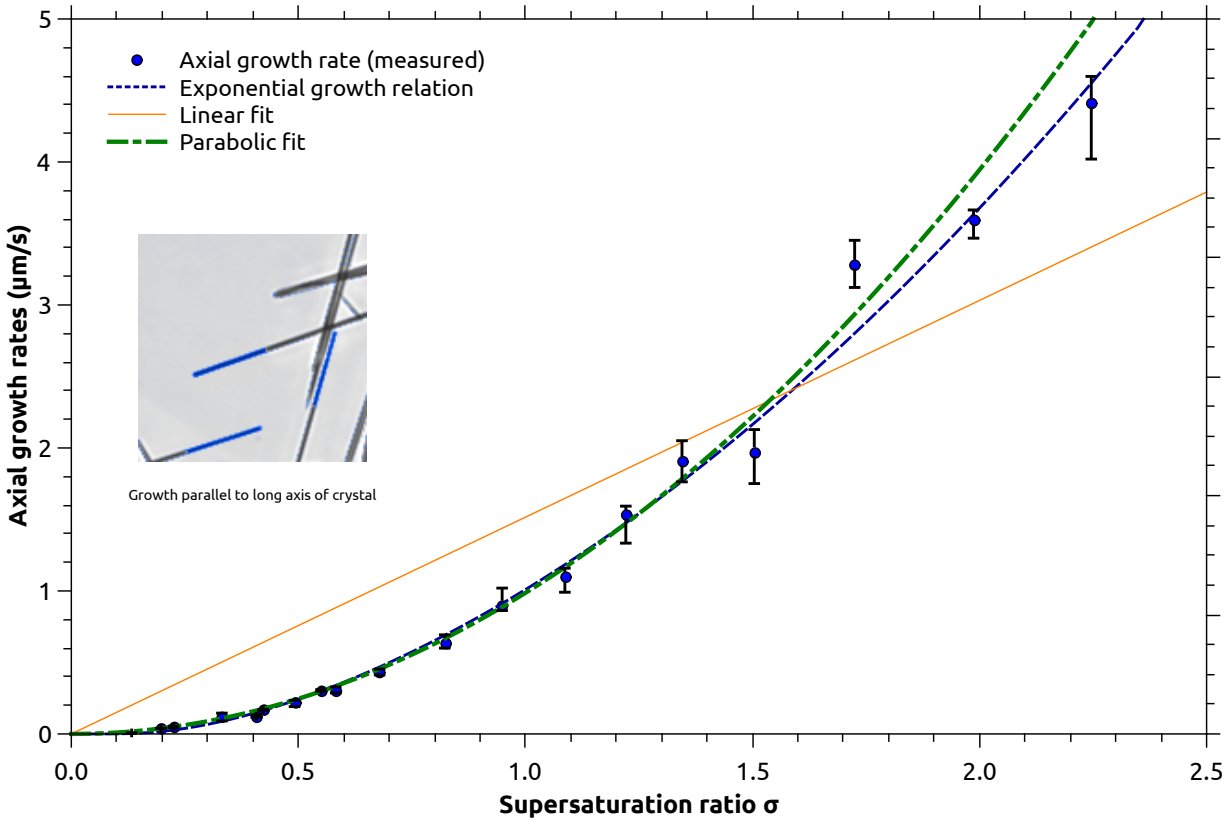

Figure 2.5: Analysis of axial growth of crystalline FF assemblies. a) Plot of the rate of growth of axial faces of FF crystals as a function of the degree of supersaturation $\sigma = (c - c^*)/c^*$. The blue dashed line is the best-fit curve obtained from the 2D nucleation-growth model [71]. The figure also shows the best fits to the linear (orange dotted line) and parabolic (green dashed dotted line) rate laws.

in each case from experimental runs yielding at least 25 growing crystals. The error bars represent the range of those five crystals.

The radial growth rates for FF are shown in 2.6a. As in the case of the axial growth rate, the radial growth rate also depends in a higher than linear manner on σ. Interestingly, the radial growth rate remains at a very low value over a wider range of values of the supersaturation ratio than does the axial growth rate; indeed, at σ values below $\sigma = 0.4$, radial growth is not detectable, although axial growth is significant. Moreover, the rates

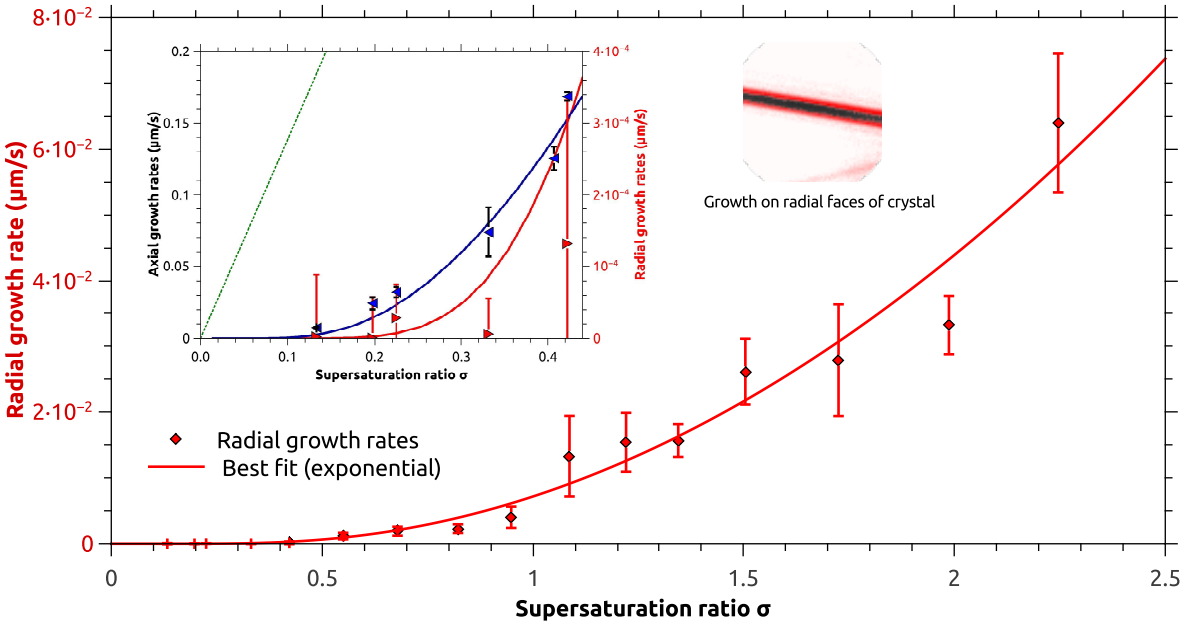

Figure 2.6: Analysis of radial growth for FF crystals. a) Radial growth rates of FF crystals as a function of the supersaturation ratio over the range $\sigma = 0$ to $\sigma = 2.25$. Inset: comparison of radial (in red, and right scale) and axial (in blue, and left scale) growth rates. Note that, within experimental error, radial growth is negligible in the range of σ shown in the inset ($\sigma = 0$ to $\sigma = 0.4$). Error bars are the standard deviations of the five fastest measurements (one measurement per crystal) due to limitations of resolution.

of radial growth are ca. two orders of magnitude slower than the axial growth rates for all values of σ that were tested.

2.2.4 The mechanism of growth of diphenylalanine crystalline assemblies

Crystal growth from solution is a complex process. Once it has been established that the assembly reaction is proceeding according to a process occurring at, or at least involving the surface (in this case, this is demonstrated by the independence of growth rate from

diffusional arrival rate demonstrated in figure 2.3), the functional form of the relationship can be analysed. The growth process involves diffusional arrival of the monomeric building blocks, adsorption onto a growing face, which is usually accompanied by desolvation, followed by surface diffusion until a defect is encountered or by the formation of a two dimensional nucleus [71]. Each of these processes can be rate determining, depending on the chemical nature and concentrations of the species involved and the solution conditions. For simple inorganic crystals, it has been established that the observed functional dependence of the growth rate on the degree of supersaturation of the solution can be used to decide which of the elementary steps is rate determining [71].

Broadly speaking, the growth of new layers on the face of a crystal from solution is a co-operative process. Incoming monomers must be stabilised against resolvation by the formation of bulk-like contacts with other monomers adsorbed to the face. The basic structure of a face capable of incorporating incoming monomer is detailed in figure 2.7- that is, a monomolecular "step" containing a position at which the incoming monomer is coordinated at half its (bulk) contacts with the monomers in the new layer and the layer below. The diagrams display a simple cubic (Kossel) crystal structure, only found naturally in crystals of $\alpha-$polonium [81], but the principles remain the same regardless of the actual crystal structure.

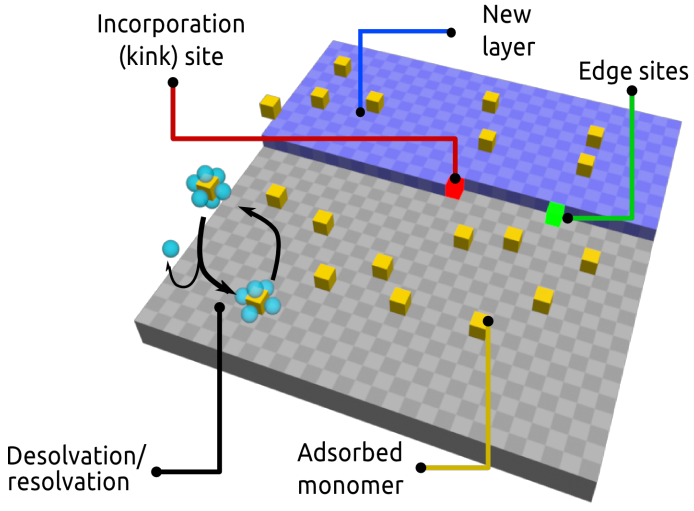

Figure 2.7: Representation of features on a simple cubic crystal face. The base crystal is highlighted in grey, the first layer of the crystal is shown in blue and the monomers adsorbed to the surface are shown in yellow. The black arrow denotes a (de)solvation process. Monomers occupying an edge site are highlighted in green, while those occupying a kink site are shown in red.

For a perfect flat (F) face, it is obvious that no incoming atom will be coordinated on more than one face by like atoms (i.e. those in the layer below). In terms of the edge energy, the 2D analogue of the surface free energy introduced in equation 1.3, for our $\alpha-$polonium crystal we have created five new uncoordinated sites. This raises the energy of the face. Raising the energy of the face rather less is the green atom at the edge of the new layer- however, desorption of that atom still reduces the edge energy of the new layer by the energetic cost of two uncoordinated sites. Only the red atom, at a "kink" site, does not change the edge energy of the new layer. These sites, being as they are unaffected by the influence of edge energies, are the positions that are equally occupied/unoccupied in equilibrium (although this does imply that the face is imperfect, containing at least one "step").

Recalling the definition of the critical concentration in equation 2.1, the face of the crystal will be in equilibrium with the species in solution when the concentration is equal to the critical concentration. The desorption and resorption rates (the "on and off" rates) are equal at this concentration. Generally speaking, the "on rate" is proportional to the concentration in the ambient phase, whereas the "off rate" is proportional to the critical concentration. In cases where the growth rate R_g of a given face is limited by the diffusional arrival of the building blocks, a linear dependence of R_g on σ is anticipated, such that $R_g = k_l\sigma$ with rate constant k_l. Steps were taken to ensure that incorporation rather than diffusion was the rate limiting step for the kinetics experiments in this chapter- Figure 2.3 shows the growth rate plotted against flow rate in the reactor- a limiting rate is observed at 800 μL/h and above, corresponding to a change of regime from diffusion to incorporation-controlled growth.

The dotted line in 2.5 shows that a linear relationship of the growth rate on σ, corresponding to a monomolecular or diffusion-limited addition process, does not provide a good fit of the data and hence cannot describe the addition of FF to its crystals. Surface diffusion to defects, such as screw dislocations or kink sites, is expected to yield a parabolic rate law [71], $R_g = k_p\sigma^2$, with k_p being the rate constant. A similar rate law applies in the case of rate limitation by the incorporation process, the flux on to the addition (kink) sites [71]. This phenomenon is explored in Chapter 3.

Diffusion from the solution in the immediate surrounding of a step is the dominant route to incorporation for solution-grown crystals [70, 82]. In crystals grown from the vapour, monomer diffuses once adsorbed to the face, frequently making a great number of diffusional "jumps" from site to site. This is strongly inhibited by the presence of solvent on the surrounding surface, reducing the number of diffusional jumps made before resolvation occurs and hence the range on the surface over which incoming monomer will be incorporated by a step after adsorbing to the surface.

At any one time, on an F-face of the assembly (as the axial faces are currently being assumed to be), there will exist a population of adsorbed monomers dependent on the adsorption equilibrium constant- considering the volume described by the layer of adsorbed monomers/solvent, the concentration in this layer is $c_{ad} = K_{ad}c$ for c, c_{ad} the concentrations of monomer in the bulk and on the face respectively. As in the 3D case, the population of monomer on the surface will consist of simply adsorbed monomer and groups of monomers forming "islands" of multiple monomers occupying adjacent sites and thereby stabilising each other against resolvation. This gives rise to a familiar relationship- the limiting step in growth normal to the surface has a nucleation-dependent component.

If the crystal face extends by the 2D-nucleation and subsequent growth (birth-and-spread) of islands, higher-than-quadratic or exponential behaviour is predicted [71]. It is difficult, based on the data alone, to distinguish between a parabolic or exponential dependence which yield similarly good fits (2.5, blue and green dashed lines). However, it has been established that growth due to surface defects, such as screw dislocations, is dominant only at very low degrees of supersaturation in most systems [70]. At higher supersaturation ratios, the rate at which addition (kink) sites are formed by the simple presence of high surface concentrations of monomeric subunits is far greater than the rate at which they are formed by addition to pre-existing sites [70, 71].

Defects are of course non-kinetic phenomena on these timescales, however rates limited by incorporation processes are predicated on there being an abundance of addition sites,

however these arise. If nucleation is not rate determining, then the incoming monomer arrives at a kink-rich surface on account of the presence of the stable nuclei. Burton, Cabrera and Frank [70, 83] give an equation relating the equilibrium kink density on a stepped face as a function of supersaturation, appearing in chapter 3 as Equation 3.15. This kink density is approximately linear in σ, and for a gross arrival rate also linear in σ, the result is that R_g varies as σ^2 [71].

Defect-mediated growth is dependent to a large degree on surface diffusion of monomers to kink sites; this process is inhibited in solution growth relative to diffusion from bulk solution [70, 84]. Therefore, the defect theory of growth is inconsistent with the wide range over which the growth rate is non-linear in σ.

By contrast, a nucleation and spread mechanism is able to explain the data in 2.5 and 2.6. In this model, the non-linear relationship between the degree of supersaturation and the growth rate is the result of the balance between the energy cost of creating the coordinatively unsaturated edge sites relative to the energy released by the formation of the more fully coordinated sites in the interior of the nucleus. According to classical nucleation theory [71], this criticality behaviour gives rise to an exponential dependence of the nucleation rate on the surface density of monomers, which is in turn dependent on the relative magnitude of the desolvation/resolvation rates and hence on the degree of supersaturation [85].

To explain the exponential dependence of the rate of growth on σ, we note that the overall excess free energy of a surface island with n growth units is given by [71]:

$$G(n) = 2\gamma(\pi n)^{1/2} - n\Delta G_\nu \tag{2.2}$$

where γ is the edge energy and $\Delta G_\nu = k_B T \log(\sigma + 1)$ is the free energy change of the transformation per growth unit. This is the 2-dimensional analogue of the nucleation expression given in chapter 1, equation 1.4. Edges, the analogue of the surface in the 3D expression, are the high energy feature with a free energy cost. We see, therefore, that secondary nucleation is an intrinsic part of the elongation process in the kinetic regime explored in this study.

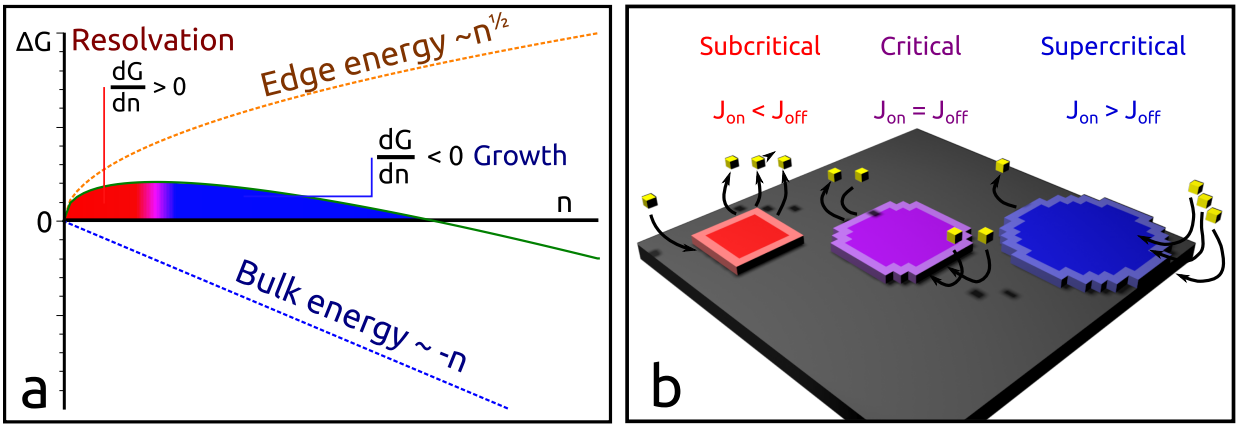

Figure 2.8: a) The overall excess free energy of a surface island with n growth units, $G(n)$, has contributions from the edge energy ($\sim n^{1/2}$) and bulk ($\sim n$). Hence, the sum of these two terms has a maximum in correspondence to the critical nucleus size n^* (purple). When $n < n^*$, island growth is unfavourable ($dG/dn > 0$, red), whereas for $n > n^*$ island growth is favourable ($dG/dn < 0$, blue). b) Schematic representation of nuclei, with edge sites highlighted. Edge sites are coordinatively unsaturated and so have a higher rate of resolvation; the ratio of edge-to-bulk sites determines the nucleus size (n).

The first term of $G(n)$ is positive and increases in proportion to $n^{1/2}$, while the second term is negative and varies linearly with n. Hence, as shown in 2.8a, the sum of these two terms has a maximum value that occurs when $dG/dn = 0$. The value of n at this point is $n^* = \frac{\pi\gamma^2}{\Delta G_\nu^2}$. When $n < n^*$, island growth is unfavourable ($dG/dn > 0$), whereas for $n > n^*$ island growth is favourable ($dG/dn < 0$). Along with this critical nucleus size comes a nucleation barrier of magnitude:

$$G^* = \frac{\pi\gamma^2}{\Delta G_\nu} \tag{2.3}$$

that determines the rate of nucleation

$$J \sim e^{-G^*/k_B T} \tag{2.4}$$

. If we now define the rate of growth R_g as the inverse time required for nucleated islands to fill up the layer of area A across the growing crystal face, $\tau \sim (JA)^{-1/3}$, we find, using the expression for the nucleation rate that $R_g \sim (AJ)^{1/3} \sim e^{\frac{-K_b}{\ln(\sigma+1)}}$, where $K_b = \frac{\pi}{3}(\frac{\gamma}{k_B T})^2$.

The exact exponential relationship between the growth rate and σ that is predicted by classical nucleation theory [71] can be expressed as:

$$R_g = k_e(\sigma+1)^{7/6}\sigma^{2/3}(\ln(\sigma+1))^{1/6}e^{\frac{-K_e}{\ln(\sigma+1)}} \tag{2.5}$$

where

$$k_e = 2a\nu_{in}(K_{ad}c^*V_m)^{4/3}e^{\frac{-\gamma}{k_B T}} \tag{2.6}$$

and

$$K_e = \frac{\pi}{3}(\frac{\gamma}{kT})^2 \tag{2.7}$$

In this expression, a is the lattice site spacing, ν_{in} is the integration jump frequency (incorporating the desolvation step) for the diffusional jump to a stable (kink) lattice site, γ is the edge energy and K_{ad} is the equilibrium constant for adsorption to the surface. The term $K_{ad}c^*V_m$ therefore represents the occupation ratio of surface sites in equilibrium with the solution [71]. The values for the rate constant k_e and the parameter K_e obtained from the fit

of the axial and radial experimental kinetic data were determined to be: $k_{e,ax} = 1.02 \pm 0.06$ μm/s and $K_{e,ax} = 0.52 \pm 0.04$, yielding $\gamma_{ax}/k_BT = 0.70 \pm 0.03$ per site for nuclei on the axial face, and $k_{e,rad} = 0.03 \pm 0.01$ μm/s and $K_{e,rad} = 1.5 \pm 0.3$, yielding $\gamma_{rad}/k_BT = 1.2 \pm 0.12$ per site for nuclei on the radial face.

Therefore, a relatively small difference in edge energy of 0.5 k_BT leads to a striking difference of up to three orders of magnitude in axial and radial growth rates, and consequently to a highly elongated morphology. The origin of this difference in energy at the molecular level can be attributed to the alignment of the charged and polar groups within the crystal structure [1, 56, 46].

2.2.5 Morphological control of dipeptide supramolecular polymers

Variations in crystal morphology and aspect ratio have been achieved for inorganic crystals [86, 87] through control of the degree of solution supersaturation. The extended metastability of supercooled FF solutions at high concentrations allows the degree of solution supersaturation to be varied over a wide range, suggesting that the morphology of FF assemblies might be varied through the control of supersaturation. As FF is the subject of much research into possible applications in materials science [5, 88, 89, 90], the ability to tune aspect ratios of these crystalline supramolecular assemblies is of great importance [68, 91]. Based on our conclusions concerning the growth mechanism and its dependence on supersaturation, experiments were designed with the goal of growing the assemblies in a regime in which only axial growth can occur at a significant rate, and to compare the aspect ratios of the resulting assemblies with those that are grown under conditions permitting both axial and radial growth. The use of a flow reactor makes it possible to maintain the system under a non-equilibrium condition, in which the crystal dimensions are not determined by the equilibrium solubilities of each face, but rather by the respective growth rates [82, 92], opening up the possibility of kinetic rather than purely thermodynamic control of peptide self-assembly.

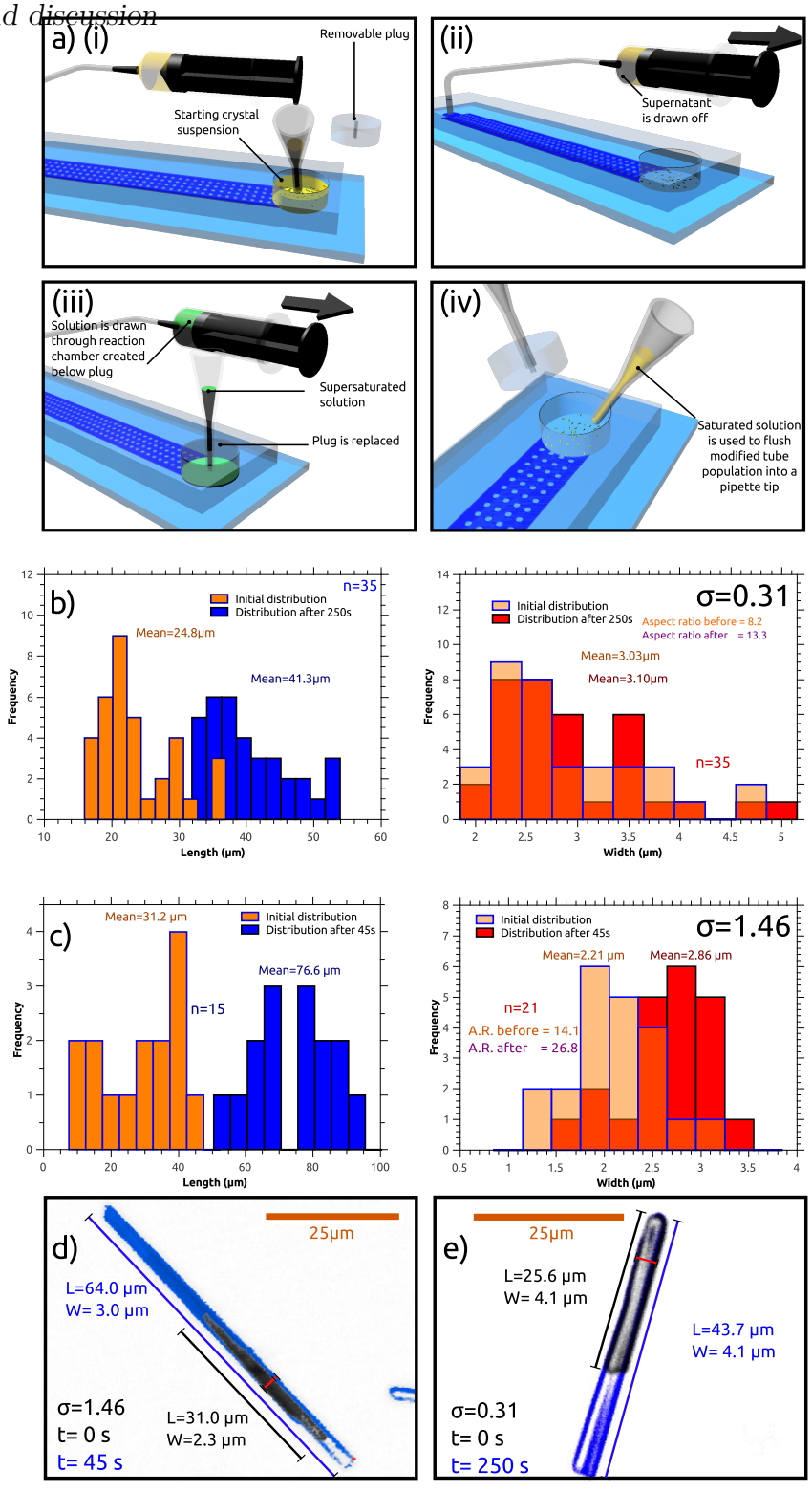

Figure 2.9: (Continued on following page.)

Figure 2.9: Morphology control in a non-equilibrium flow reactor setup a) Schematic representation of a bulk microfluidic reactor. (i) A homogenised suspension of FF crystals is introduced into the channel through a broad well that is generated by the removal of a circular plug. (ii) The supernatant is drawn off with a syringe pump. (iii) The plug is reinserted generating a second reservoir containing a solution of known supersaturation (green). This solution is drawn over the bed of the reactor by the syringe pump. (iv) The modified crystals are flushed into a pipette tip for further processing and study. (b,c) The results of this experiment indicate the development of the populations of crystals measured *in situ* without removal from the device. b) Length and width distributions before and after exposure for 250 s to a flow of solution at σ=0.31. Average aspect ratio changes from 8.2 to 13.3 during the 250 s run. c) Length and width distributions before and after exposure for 45s to a solution at σ=1.46. Aspect ratio changes on average from 14.1 to 26.8 in 45 s. Some crystals grew outside of the observed area during this run. d) Illustration of a crystal that has undergone both axial and radial growth at $\sigma = 1.46$. e) At σ=0.31, only axial growth is observed.

To establish the applicability of the findings described above to the controlled growth of populations of FF microcrystalline assemblies, an experiment was devised to prepare initial samples of highly homogeneous crystals and then to grow them in a device with removable plug, allowing opening and re-sealing to enable the recovery of samples after exposure to the supersaturated solutions (2.9a). Comparison of the distributions of length and width before and after exposure to a given growth condition demonstrates the controlled increase in aspect ratio possible at a low level of supersaturation ratio ($\sigma = 0.31$), where the solution conditions are maintained by continuous flow; under these conditions, no radial growth was detectable within experimental error. The rapid growth at a higher supersaturation ratio ($\sigma = 1.46$) results in radial growth occurring simultaneously with axial growth. From an initial suspension of microcrystals with a given distribution of radial dimensions, this distribution can be maintained while the crystals undergo solely axial growth (2.9b and e), or it can be increased (2.9c and d) simultaneously with axial growth. The crystals so modified are easily recovered from the device through resuspension in a saturated solution, or in a liquid in which the dipeptide is practically insoluble, e.g. hexane or perfluorocarbons [56].

2.3 Conclusions

Detailed mechanistic analysis, made possible by the application of microfluidic techniques described here, reveals that crystalline FF supramolecular polymers grow in aqueous solution by a process of 2D surface nucleation (2DN). There are differences between axial and radial growth rates in FF as a result of the very different surface free energies characteristic of each face. The relative growth rates of the axial and radial faces of the FF microcrystals have been found to be adjustable through simple control of the supersaturation levels of the solutions in microfluidic flow reactors. This conclusion enabled the development of procedures for the controlled modification of the aspect ratio beyond the values dictated by thermodynamics, and for the transfer of populations of crystalline assemblies for further processing. The overall morphology of these crystalline aggregates is of great significance in the context of their applications as scaffolds or actuators for a variety of complex nanoscale structures, and the ability to control the aspect ratio of the structures enables in a simple manner to tune the physical properties of the assemblies.

It is possible to contrast the FF microcrystals studied here with amyloid fibrils formed from polypeptides and proteins. Amyloid fibrils are typically stable as μm sized filamentous aggregates with diameters in the nm range, consisting of one or more protofilaments [93, 94], though the fibrils often display a propensity towards higher-order association or "bundling" dependent on sequence and growth conditions [95, 96, 97]. A "step-like" saturation dependence of radial growth in amyloid has been modelled [98] but the kinetics of such a process remain obscure. Other studies indicate that bundling is mediated through colloidal aggregation of pre-formed fibrils [99, 100] in contrast to the monomer saturation dependent relationship in the case of FF radial growth.

Direct comparison to the growth kinetics of amyloid fibrils is difficult because the rates of FF crystal growth recorded in this study are upper limits of the rate for a given concentration- if the crystal face is effectively one atomic diameter from a solution of supersaturation σ, the incorporation rate is then limited by whatever processes may be necessary to place

the monomer on a lattice site. At low and moderate supersaturation, the requirement for cooperativity due to the instability of single adsorbed monomers on the surface results in a higher-order limiting step- there must exist sufficient addition sites on the surface, and these can arise from steps generated by persistent defects (parabolic kinetics), or by the requirement that nucleation of stable 2D steps can occur on the surface. If the nucleation is rate limiting, the observed kinetic signature is exponential. At some point, represented by σ_L in figure 2.10, mechanism becomes indistinct as extreme arrival rates reduce the barrier to addition to whatever step is necessary to transport a monomer on to the surface. Addition does not become barrierless, but it does become linear in supersaturation. Figure 2.10 shows the fastest rates at which a crystal can grow for a given supersaturation. A real growing crystal can display one or more of these growth regimes, which represent limiting rates. A crystal growing in the nucleation-limited regime $0 < \sigma < \sigma_P$ can grow at any rate up to that highlighted by the solid blue line, but the crystal itself cannot incorporate monomer any faster.

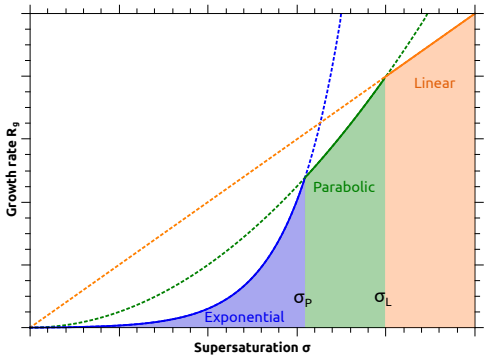

Figure 2.10: Figure based on references 70, 71 demonstrating possible transitions between regimes. The observed rate is in bold, while the calculated dependencies are dotted lines. Below σ_P, the rate is limited by the unavailability of addition sites due to the lack of growing nuclei. Between σ_P and σ_L, the reaction is parabolic in σ due to dependence of growth rate on surface adsorption [71] or a σ-dependence of growth site concentration on a face with established nuclei generating steps [83]. Above σ_L, the face is effectively "roughened" by rapid deposition and the rate is linearly related to bulk supersaturation through some energetic barrier to incorporation.

In the case of amyloid fibril, however, most experimental assays result in linear σ dependence of growth rate, transitioning with increasing concentration to sublinear scaling due to the kinetics of internal processes of the chain as it is added [77]. The incoming monomer in a process of amyloid elongation must rearrange in order to adopt the required conformation [101], thus propagating the growth position in much the same way as the spreading layers of the crystal (Figure 2.7). Such a process naturally leads to a "saturation" regime, where growth rate is effectively independent of the concentration of free monomer.

A strictly analogous definition of growth rate, if applied, would constrain the discussion to the elongation and secondary nucleation processes on amyloid fibrils- the elongation process is readily identifiable with the axial growth process of FF, and what for an amyloid fibril may be considered secondary nucleation could be said to correspond to the radial growth of FF. It would be very hard in light of results in this chapter to argue both analogies at the same time, however. Results here suggest that the mechanism, if not the kinetics, of the addition process on the axial and radial faces of FF are the same, and that they are described well by the models that apply to the crystallisation of small molecules [70, 71, 83]. These processes involve both secondary nucleation (the nucleation of new crystal layers on a face) and addition to those nuclei (analogous to elongation), and the limiting nature of the nucleation/addition process can be observed in the kinetics of growth of FF aggregates.

The kinetics of diphenylalanine aggregation therefore are distinct in several important ways from the processes underlying amyloid propagation. In the first instance, diphenylalanine displays aggregation kinetics with order >1, while non-saturated amyloid elongation is first order in monomer concentration, and saturated amyloid elongation is zeroth order, the kinetics being determined by the rearrangement of the monomer at the fibril tip.

Chapter 3

Thermodynamics of diphenylalanine self-assembly

3.1 Introduction

As has been mentioned, the structures so formed were initially discovered by Carl Henrik Görbitz [1] in a survey of the crystal structures of hydrophobic dipeptides, and the remarkable mechanical properties [9] and unusual tubular morphology [3] have led to great interest in possible nanotechnological applications of the dipeptide, and indeed in various modified forms of the dipeptide, in particular the readily available derivative N-tertbutyloxycarbonyl-phenylalanyl phenylalanine (Boc-FF), a material notable for the extreme mechanical stiffness displayed by an amorphous aggregate [13], an aggregate surprisingly distinct from a crystalline polymorph of the compound identified years earlier [102].

Comparison of the thermodynamics of dipeptide and polypeptide aggregation is an important step towards rationalising or discounting the employment of short peptides as model

systems for amyloid propagation. In particular, the desolvation of the benzyl groups is predicted to contribute a significant negative free energy to the process of amyloid fibril formation. In polypeptide systems with hydrophobic residues, the enthalpic component of the free energy of aggregation is negative at low temperature, transitioning through zero to give a positive ΔH at high temperature [103]. The free energy of solvation remains relatively unchanged, however, indicating an entropic contribution to the free energy that is nearly equal in magnitude and opposite in sign. This compensation is thought to arise mainly from the effect of the hydrophobic substituents on the surrounding solvent [24], and this compensated relationship is diagnostic of the influence of the hydrophobic effect [19]. Hydrophobicity also leads to more transient interactions in solution, most notably amphiphilic aggregates, highly fluxional polymeric aggregates of species in solution which display both hydrophilic and hydrophobic properties promoting solvent-induced self-association.

Baldwin et al. studied the dependence of the free energy of fibril elongation, per peptide unit, on the length of the polypeptide [63], and found an empirical power-law relationship governed by contact area between chains. The free energy was established by solubility studies via the linear polymerisation model of Oosawa [104], where the equilibrium constant for the addition to fibrils of all lengths reduces to that between fibril ends and monomers. Diphenylalanine displays markedly greater non-polar side chain surface area per peptide than typical biologically relevant polypeptides, and the pi-stacking interactions will represent a significant portion of the side chain interaction energy.

Tjernberg [50] found that polypeptides as short as tetrapeptides (KFFE, KVVE) were capable of forming amyloid-like fibrils, and Gazit investigated the role of the F side chain in amyloidogenesis [51, 4], with a focus on pi-stacking interactions as a driving force for aggregation. It was also proposed [52] that electrostatic interactions between oppositely-charged residues further increase the propensity of short sequences to form amyloid fibrils. The ability of short peptides to form amyloid fibril appears to be highly dependent on both the hydrophobicity of the side chains but also on aromatic-specific pi-pi interactions [4]. As the simplest possible aromatic polypeptide, with unblocked and oppositely charged terminal

amine and carboxylate groups, diphenylalanine is an ideal model system to investigate in detail the relative importance of the different energetic contributions.

3.2 Results and discussion

3.2.1 Critical concentration

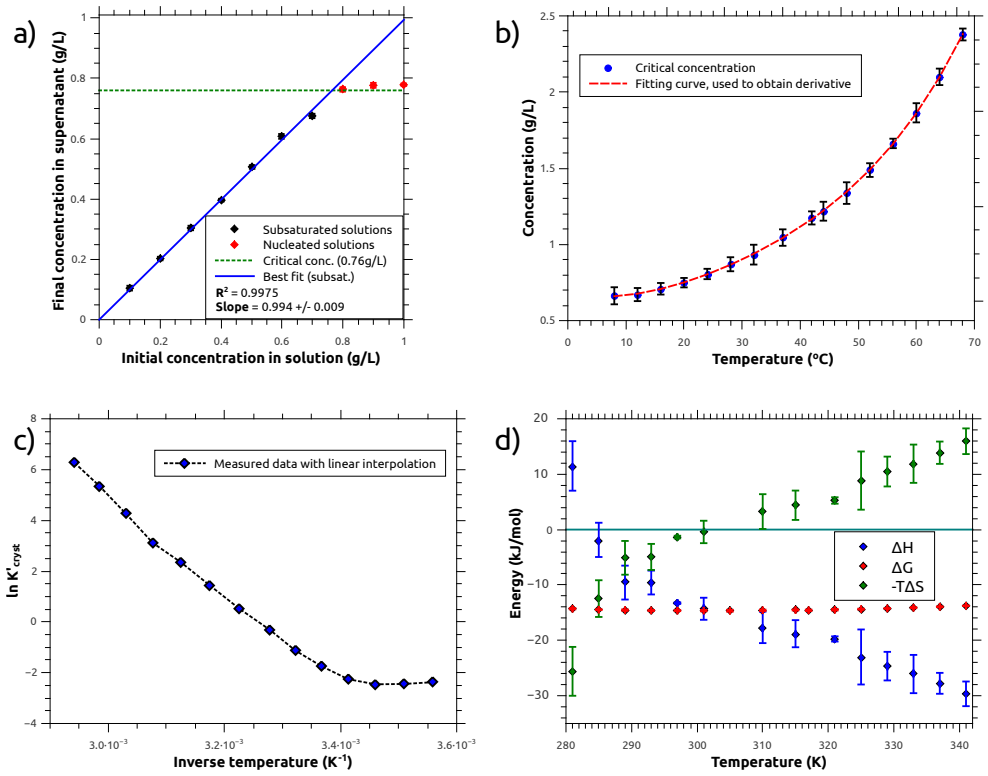

Figure 3.1: a)Absorption of supernatants following centrifugation of equilibrated samples of varying peptide concentration, demonstrating absence of association below 0.76 g/l at 293 K. Error bars range of 3 repeats. b) Critical concentration of FF in water as a function of temperature, 8 to 68^oC. c) Van't Hoff plot derived from solubility data. d) Thermodynamics of FF crystallisation, derived from the solubility data and the van't Hoff relation in (c)

I first established the critical concentration, i.e. the concentration below which no aggregation is observed. This was carried out by ultracentrifugation of aggregated samples (represented by the green line on the graph), followed by spectroscopic determination of the concentration of soluble peptide as a function of total peptide concentration. Figure 3.1a shows how peak absorption varies with concentration in samples above and below the critical concentration at room temperature. The absence of detectable curvature to the plot implies the absence of subcritical aggregation, and the consumption by the nucleation process of only enough material to reduce the concentration to this critical value. This result indicates the criticality behaviour of classical nucleation theory, with a large critical nuclear size, a conclusion supported experimentally by the ease with which supersaturated solutions can be prepared through cooling. Metastable solutions of 6 g/L (19.2 mM) can be prepared at room temperature through the cooling of homogeneous solutions that are stable close to the boiling point of water.

In order to probe this hypothesis further, the size distribution of FF species in sub-critical and supercritical solutions, in water, methanol and acidic (HCl) solution was investigated by means of dynamic light scattering. A supercritical solution at 2.1 g/l was prepared by dissolving the peptide in water at 80°C and cooling the solution to room temperature. Prior to measurement, the solution was passed through a 0.22μm filter. The 0.7 g/l solution was prepared by threefold dilution of the 2.1 g/l sample and also filtered before measurement. The acidic sample was prepared from a different stock solution at 1.53 mg/ml and the pH was adjusted by adding 20 μl of 1M HCl to 200 μl of peptide stock, yielding a pH of 1.6 (due to the buffer effect of the peptide) and a final concentration of 1.39 g/l.

Figure 3.2 shows the scattering intensity weighted size distribution. Both aqueous samples in Figure 3.2 a) show a peak at ca. 1 nm, corresponding to monomeric FF or possibly very small oligomers, such as dimers/trimers. Peaks also exist in all samples apparently corresponding to species with a Stokes diameter between 100 and 1000 nm. These larger species would dominate the scattering intensity if present at significant concentrations, due to the Rayleigh scattering relation $I(d) \propto d^6$. The fact that the monomer/small oligomer

is detected above species contributing signals many orders of magnitude greater in intensity suggests that FF solutions are monomeric prior to the start of the nucleation process. The high concentration of FF in the solution may potentially give rise to some degree of non-ideality, or spurious peaks may have arisen from the from the fitting process. The strong similarity between the size distribution in sub-critical and super-critical solutions also speaks in favour of the absence of pre-nucleation clusters, as such the concentration of clusters could be expected to display a highly non-linear dependence on the total concentration of FF.

The sample in methanol at 2.1 g/l, the green curve in figure 3.2 a), shows the same characteristics - far below the critical concentration in the methanol/FF system, the largest peak corresponds to a monomer or other small species. Due to the very different solvent environment, amphiphilic aggregation processes are thought an unlikely origin of the 200 nm peak. Furthermore, in Figure 3.2 b), the Stokes diameter population of a 1.39 g/l FF solution in solution at pH 1.6 is depicted, corresponding to a clearly sub-critical concentration at this pH, and the detected size distribution is very similar to that in pure water.

The critical concentration is that at which the chemical potentials of FF in solution and in the (infinitely sized) crystal are equal, the driving force for the crystallisation being:

$$\Delta G = RT \ln \frac{c}{c_{crit}} \tag{3.1}$$

In addition, I examined the critical concentration as a function of temperature. As was mentioned in the Introduction, hydrophobic desolvation processes have a particular enthalpic signature. Solubilities at the tested temperatures (8 to 68°C) range from 0.65 to 2.4 g/L, with a minimum close to 10°C. The variation of the solubility with temperature allows the enthalpy change on crystallisation to be derived from the van't Hoff relation:

$$R\frac{d(\ln K_{cryst})}{d(\frac{1}{T})} = -\Delta H \tag{3.2}$$

Figure 3.1b shows that the $\Delta \mathrm{H}_{cryst}$ is temperature dependent, and therefore confirms the existence of a heat capacity of crystallisation, $\Delta \mathrm{C}_{cryst}$.

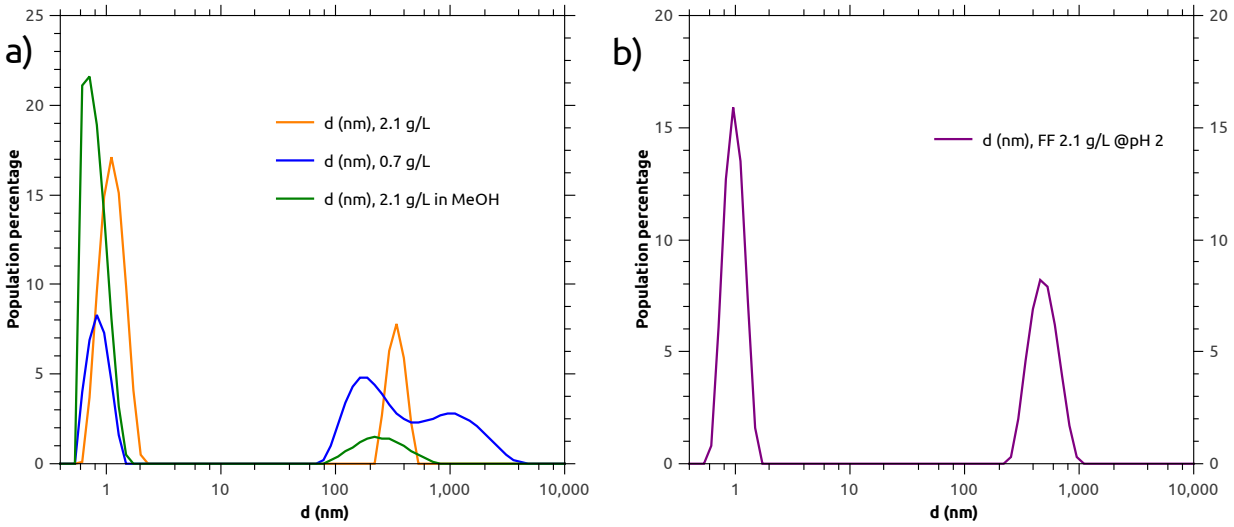

Figure 3.2: Calculated Stokes diameter distribution from DLS experiments of a) solutions of FF in water, 25°C. The orange line is the reading for a supercritical solution at 2.1 g/l, the blue line the reading for a subcritical solution at 0.7 g/l. The green line shows the reading from a solution in methanol at 2.1 g/l, in methanol solution the critical concentration is 10 g/l [56]. b) 2.1 g/l solution of FF in HCl solution (pH 1.6)

This heat capacity falls away sharply with increasing temperature, at 45 degrees it is already possible to approximate the solubility data with a linear best-fit line. The minimum of the van't Hoff plot in figure 3.1 represents a point of zero enthalpic change on solution/crystallisation, ΔG depending solely on the negative entropy of the forward process at this point.

Despite the large changes in ΔS, ΔH, the process of FF crystallisation in water appears heavily compensated- while the entropies and enthalpies of crystallisation vary widely across the temperature range, the free energy is relatively invariant.

A favourable enthalpy will arise from the interactions in the crystal- the aromatic substituents are engaged in an extended π - stacked structure and relatively fixed, well-aligned hydrogen bonding is present along helix axes. This enthalpy due to crystal interactions will again be largely temperature independent, and as mentioned above, dependent on the surface area of the hydrophobic group that is "buried".

A main aim of this chapter is the determination of the relative contributions of the peptide backbone and the (aromatic) side chains to the free energy of aggregation. This analysis is complicated by the existence of nonlinear effects- the presence of the polar peptide link and the charged termini changes the structure of the solvent in the region around the hydrophobic groups and so the total free energy of aggregation may be far from the sum of the free energies of the component groups [25].

The observed behaviour is typical of assembly processes driven through hydrophobicity, regardless of the presence of solubilising groups on the dipeptide (the interactions between these and water and these and corresponding groups in the crystal being roughly energetically similar). Interestingly, a similar nonlinearity of critical concentration with temperature occurs for certain hydrophobic single amino acids in solution (for V, L, I, W) [105].

3.2.2 Diphenylalanine as a model amyloidogenic peptide

The critical concentration (the concentration of FF in solution that is in equilibrium with its aggregate), can be directly compared with Baldwin's M_s, the equilibrium concentration of soluble protein in the presence of a fibrillar form of that protein [63]. Baldwin et al. further identified a power law relationship between the free energy of monomer addition to the aggregate, per peptide, and the fibril length (in peptide units).

$$\frac{\Delta G_{el}}{N} = \epsilon_0 + \epsilon_1 N^{\gamma} \tag{3.3}$$

This relationship is obeyed by protein fragments and short peptides, whereas complete, naturally occurring globular proteins tend to display a lower propensity to fibrillise, regardless of length. In order to test whether the relationship holds for the diphenylalanine system, I computed the relevant values and the fit evaluated with this additional data point (a polypeptide for which N=2, and for which $\Delta G_{el}/N = 7.35$ kJ/mol at 298 K).

The data in figure 3.3b is identical to that above, however, polypeptide chain length has been replaced by the related parameter of non-polar solvent-accessible surface area. In light of the observed hydration, even in the aggregate state, of various hydrophobic dipeptides [1, 108, 109] via their polar components, it was thought that relating the close-packed, non-solvent-exposed surface area to the energy of aggregation would yield an insight into the application of the geometric theory given by Baldwin et. al. .The contact-area scaling hypothesis arises from the modelling of the inter-chain interactions in the aggregate state [63]- for an aggregating species the interactions are divided into two contributions- those scaling with the length of the chain ($\epsilon_v N$) and those that are due to surface contact- dimensional arguments give the scaling of this contribution as $\propto N^{2/3}$. This argument explicitly includes surface-area contributions, although the term describing the interactions scaling directly with N (or indeed $A^{3/2}$) is still approximated as a constant. There are a number of reasons why, even for a series with the same N (the dipeptides, here), this is not valid- the high energy inter-amide hydrogen bonds do display varying connectivity [110], and as chain length increases, the influence of the charged termini decreases.

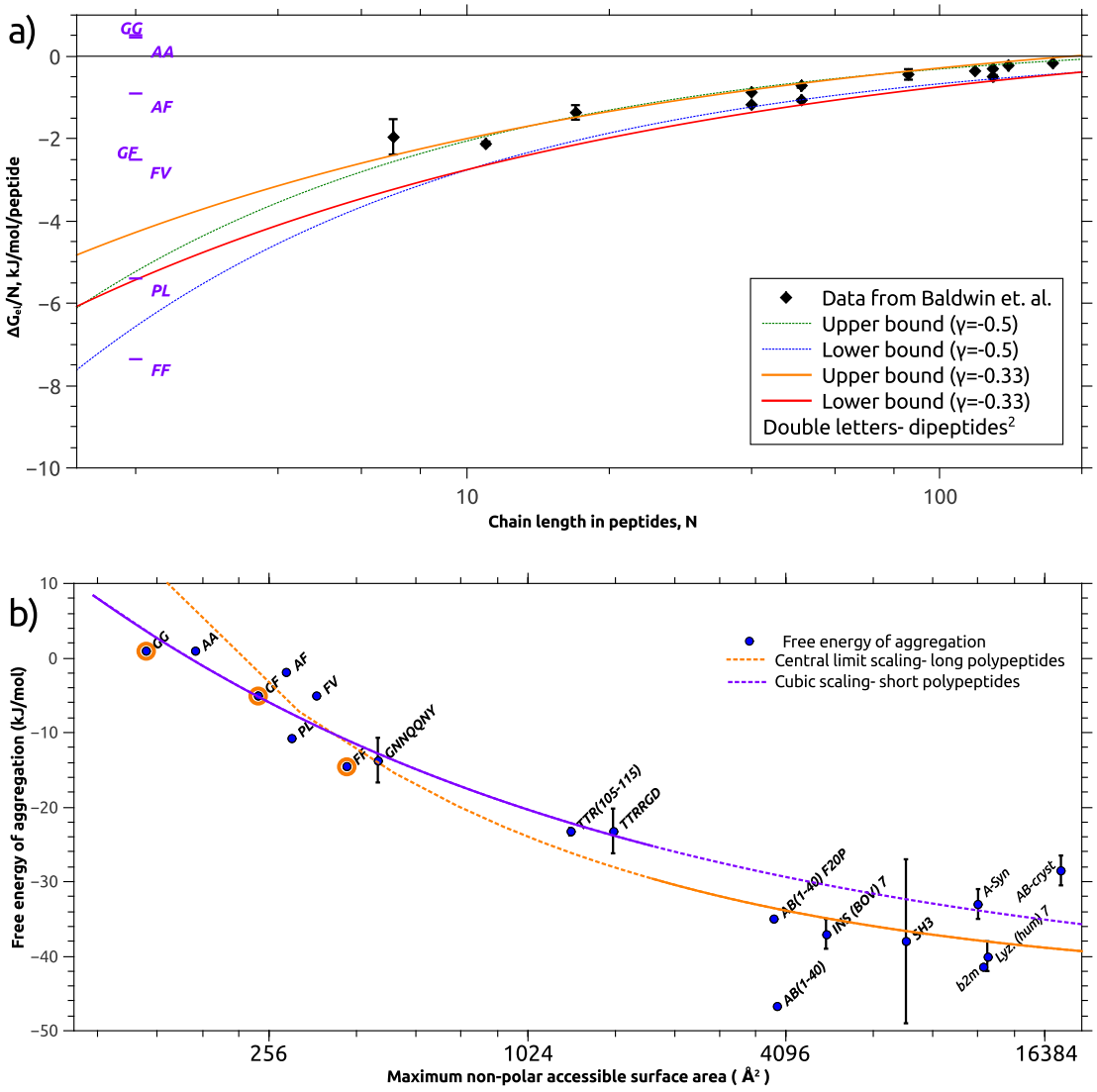

Figure 3.3: a) Data from reference 63 with addition of the dipeptides FF, AF, FV, AA and GF (this study), GG [106] and PL [107]. b) Chart displaying the relationship between non-polar surface area of the studied polypeptides and the free energy of fibril elongation. The fit for polypeptides with NPSASA <2000Å^2 is cubic ($R^2 = 0.8931$ vs. 0.8816 for the central limit expression as applied to those polypeptides), for those above 2000Å^2 the central limit theorem was applied, $R^2 = 0.3265$ vs. 0.2874 for the cubic expression (see supporting info for reference 63). The fitting curves displayed were established using a Leverberg-Marquardt algorithm, applied separately to the data points either side of the 2000Å^2 divide.

In longer species, these could be considered to "average out" as above to give the observed fit, however in dipeptides with bulky or self-associating substituents this side chain contribution to the free energy of aggregation will be somewhat larger per peptide than in naturally-occurring polypeptides. This is visible in the average non-polar surface area per residue, which I calculate to reach an average value of around $95\dot{A}^2$ for longer chains using the values calculated by Karplus [111]. A more general relation is required to approximate the behaviour of these longer polypeptides, and a scaling exponent of $N^{-1/2}$ arises from a Gaussian distribution. In figure 3.3b above, this relation is plotted as before, due to the "averaging" effect of the long chain relating the chain length (and thereby the number of contacts between chains) to the average non-polar surface area.

It is apparent that diphenylalanine displays a greater free energy of aggregation and hence a lower free concentration than the extrapolation of the curve to N=2 would predict. Inspection of the structures of Baldwin's polypeptides at N=7 and 17 (GNNQQNY and a fragment of transthyretin - YTIAA LLSPY SGGRG DS) suggest reasons for the deviation arising from the relative hydrophilicity of the fragments. GNNQQNY is unusually hydrophilic, while the TTR fragment, also deviating upwards, has a hydrophobic central strand terminating in highly hydrophilic regions. As the sequences become longer, such deviations due to predominance of hydrophobic or hydrophilic peptides "average out" producing a close agreement between data and fitting curve. Chromatographic techniques, however, present a useful method for the estimation of inter-R-group interactions, the study by Pochapsky and Gopen [112] being particularly relevant to this work as the stationary phase was designed to mimic the R-group of phenylalanine and a phenylalanine derivative was eluted. The authors found that the minimum free energy of the R-group interaction was -5.0 kJ/mol, a significant proportion of the observed ΔG_{cryst} here for diphenylalanine (-14.7 kJ/mol).

The solubilities of glycylglycine (GG) [106] and glycylphenylalanine (GF) were obtained and compared to that of diphenylalanine and compared to the predictions above. It was noted that glycylglycine (implicitly assumed to have zero free energy of side chain interaction per peptide in the chromatographic study) had a small positive $\Delta G/N$ of 0.51 kJ/mol/peptide,

while GF displays $\Delta G/N$ of -2.50 kJ/mol/peptide (and, in fact, fine needle-like crystalline habit). In this case the free energy of aggregation shows a nonlinear dependence on non-polar surface area- the F1G substitution results in nearly twice the energy change of the second substitution.

Evidently, the simple calculation used here for non-polar solvent accessible surface area (based on side chain area accessible, for each peptide, in a Gly-X-Gly tripeptide [111]) will be incorrect, even as an approximation, in longer chains with defined tertiary structure in the soluble states that will "bury" hydrophobic species in solvent-inaccessible areas.

Further, in the amyloid forms of the longer chain proteins, there exists a close-packed "core" region, where the packing model will be valid, and less structured loop regions that are not close packed [113]. The inability of a long chain to adopt conformations in which all contacts are optimal has been investigated [63], with the prediction of a different scaling exponent ($\gamma = -\frac{1}{2}$) arising from the application of the central limit theorem. Further, the specific free energy being investigated here is the difference between the soluble states as a whole, and the insoluble state (the fibril) by design of the experiment. Short peptides generally display a range of many rapidly interconverting and energetically similar structures in solution. For the longer species, a far narrower distribution of conformations is observed in solution, at the bottom of a deeper potential well.

Additional structural complexity of the close packed regions in long-chain amyloid, such as a fold resulting in intrachain interactions [114] will increase the number of close contacts per residue and stabilise the fibril. The complexity of the systems, however, precludes such a relatively simple model as that which applies to the short peptides from applying so generally.

3.2.3 Comparison with long chain amyloidogenic species

Despite a strong thermodynamic propensity for naturally-occurring polypeptides to undergo aggregation in physiological conditions due to the concentration at which some proteins are found *in vivo*, the initiation and propagation of an aggregation process remains a fairly rare event. Significant barriers are known to exist for the nucleation of amyloid fibrils, which are readily observed as nucleation "lag phases" in bulk assays [62, 115], and these can be contrasted with the often low barrier to the addition of a monomer to an existing fibril.

Direct measurement of amyloid growth kinetics has been achieved through atomic force microscopy [116, 117], and through the use of quartz crystal microbalances [78, 118]. The relation between supersaturation and growth rate is found to be linear, transitioning to a sublinear relationship thought to be due to saturation of available growth sites due to the finite time required for monomer incorporation at a growth site. The supersaturations relative to the fibrillar state are very high in typical experiments with amyloid fibrils of longer sequences compared to the supersaturations in the FF system. For example in the case of insulin a protein concentration of 1 mg/ml (174 μM) corresponds to a supersaturation of the order of 10^3-10^4, due to the very low critical concentration of this system in the sub-micromolar range [63]. It is therefore common to neglect the critical concentration in such systems and to quantify the driving force for aggregate growth directly through the absolute monomer concentration rather than supersaturation, which amounts to neglecting the fibril dissociation rate. It was found for amyloid fibrils in bulk experiments that their growth rate is a linear function of the monomer concentration, transitioning to a sublinear relationship at higher concentrations [119]; this is thought to be due to saturation of available growth sites due to the finite time required for monomer incorporation at a fibril end to produce a new growth competent end [119].

A comparison of the ratio of incident to incorporated monomer reveals a major difference between the FF and insulin systems. Estimating to an order of magnitude the rate at which monomer enters a reaction volume v surrounding one incorporation site, for a number

concentration C as $\Gamma = D \cdot v^{1/3} \cdot C$ [120], the rates of arrival at the growth sites are $\Gamma_{INS} = 1.6 \cdot 10^4 \cdot c/((mg/ml) \cdot s)$ assuming $D_{INS} = 1.5 \cdot 10^{-10} m^2/s$ [121], $v_{INS} = 10^{-27} m^3$ and c in mg/ml, and $\Gamma_{FF} = 4.9 \cdot 10^5 c/((mg/ml) \cdot s)$, assuming $D_{FF} = 4.2 \cdot 10^{-10} m^2/s$ [122] and $v_{FF} = 2 \cdot 10^{-28} m^3$. The observed rates are compared in Figure 3.4.

3.3 Calculation of the free energy barrier of FF crystal growth

A simple estimate of activation energy can be obtained from the ratio of "attempts" where an FF molecule diffuses into a reaction volume, to the absolute rate of addition. The parameter σ is supersaturation, discussed in chapter 2. It is a dimensionless ratio of the "excess" concentration of FF in solution relative to its equilibrium value in the presence of its aggregate. It is a useful parameter due to its accounting for the "off rate", or the rate at which FF molecules leave the aggregate. If all additions were successful (barrierless addition), the maximum growth rate, computed from the diffusional arrival rate, is given by:

$$R_{max} = \frac{DV_m c_s}{a}\sigma \tag{3.4}$$

where V_m is the molar volume of FF, c_s its critical concentration and D its diffusion coefficient. This gives a prefactor, in velocity units, of $6.7 \cdot 10^{-4}$ m/s. The relation

$$E_a = RT \ln \frac{R_{max}}{R_g} \tag{3.5}$$

then gives a simple free energy barrier of 15.8 kJ/mol at 295K and $\sigma = 1.06$. This analysis mirrors that for amyloid fibrils, but a non-linear dependence of R_g on σ is evident from figure 3 in the main manuscript. A fit of the growth rate R_g as a function of supersaturation σ of the form $R_g = k\ \sigma^{n_c}$ yields $n_c = 1.9$ [123]. Activation energy can then be derived as follows:

$$R_g = k^+ \sigma^{1.9} \tag{3.6}$$

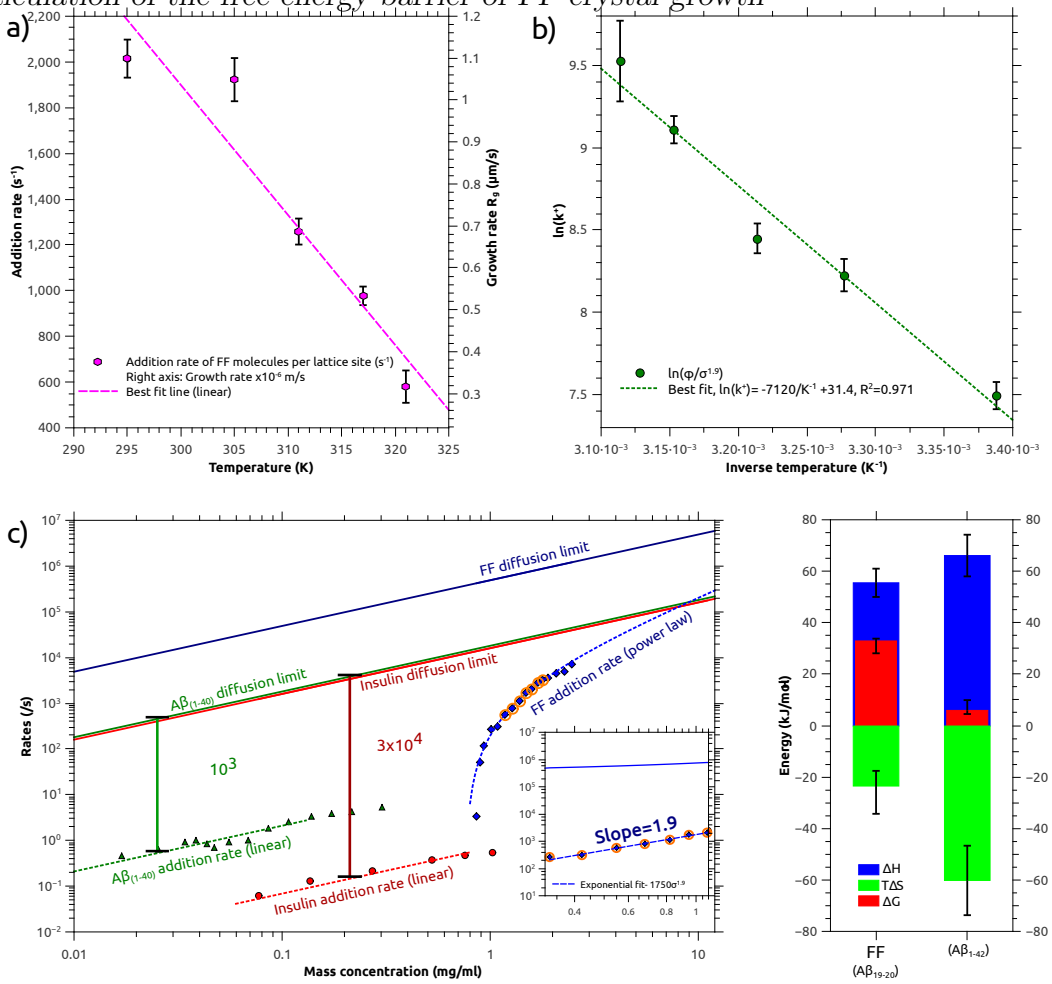

Figure 3.4: The barriers of FF self-assembly in relationship to those of amyloid fibril growth. a) Relationship between growth rate and temperature for FF for the five temperatures tested. b) Arrhenius plot of FF crystal growth; the growth rate data from panel a) has been corrected for the supersaturation dependence of the rate. c) Log-log graph comparing the aggregate growth rates of two amyloid systems (insulin [12] and Aβ(1-40) [64]) with those of FF [123]. All concentrations are given in [mg/ml]. The solid lines represent the diffusional fluxes of monomers into a reaction volume on the end of the aggregate and correspond to the theoretical maximum rates. Inset: Comparison of the measured incorporation rate as a function of supersaturation with the flux into a reaction volume the size of an FF molecule. The reaction order with respect to the supersaturation σ is determined from the fit to be 1.9. d) Comparison of free energy barriers and their entropic and enthalpic contributions between FF (computed with two different kinetic pre-factors, see supplementary material) and Aβ(1-42) [124]. Note that FF is compared with Aβ(1-40) in c) and with Aβ(1-42) in d), due to the fact that concentration-dependence data has been measured for Aβ(1-40) [64] and a complete barrier analysis has been performed for Aβ(1-42) [124].

and hence

$$E_a = RT \ln \frac{R_g}{R_{max}\sigma^{1.9}} \tag{3.7}$$

The activation energy computed by this method is 16.1 kJ/mol at 295K, and a supersaturation of 1.06.

Processes at the crystal face leading to stable addition of molecules are either sequential (one must occur prior to the other, such as generation of an addition site and addition to that site) or parallel (occurring simultaneously, such as addition of molecules in solution and of those adsorbed to the surface). The observed rate is the rate of the slowest step of a sequential process, and the fastest rate of a parallel process.

3.3.1 Nucleation and spread model

The rate law in the case of surface nucleation-limited growth is given by [71]:

$$R_g = k_e(1+\sigma)^{7/6}\sigma^{2/3}(\ln(1+\sigma))^{1/6}\exp(-K_e/\ln(1+\sigma)) \tag{3.8}$$

k_e is a rate constant, with units of m/s, while K_e is related to the nucleation activation energy.

$$k_e = 2a\nu_{\text{in}}(K_{ad}c_sV_m)^{4/3}\exp\left(-\frac{\gamma}{k_BT}\right) \tag{3.9}$$

$$K_e = \frac{\pi\gamma^2}{3(k_BT)^2} \tag{3.10}$$

meaning that the exponential term can be expressed as:

$$\exp\frac{-K_e}{\ln(\sigma+1)} = \exp\frac{-\pi\gamma^2}{3(k_BT)(k_BT\ln(c/c_s))} = \exp\frac{-\Delta G^*_{nuc}}{3k_BT} \tag{3.11}$$

where ΔG^*_{nuc} is the free energy for the formation of a critical nucleus. The Nielsen model provides for simultaneous processes of nucleation and addition to the sites generated at the edges of the growing nucleus, and the rate of growth is a product of the rate of nucleation

(J) and the (square of) the rate at which a nucleus can spread laterally (ν_∞) (equation 3.12). The rate-limiting step is different for each of these parallel processes, and the observed barrier will have contributions from both processes, though their relative importance will vary with σ.

$$R_g = a(\pi J \nu_\infty^2/3)^{\frac{1}{3}} \tag{3.12}$$

The nucleation barrier will be dominant at low supersaturation, as it approaches infinity as supersaturation approaches zero- as a result, the growth rate becomes extremely small in systems where addition sites are generated by association of molecules at the surface in a 2D nucleation process.

3.3.2 Integration rate control

Free monomer is generally not stably incorporated onto the surface of its crystalline aggregate without stabilisation by neighbouring species. Incomplete layers contain sites where addition or separation of a monomer does not result in a change of edge energy. At moderate to high supersaturations, these edges and the addition sites within them are typically generated by a nucleation process. Certain crystal defects also generate persistent edges, even at zero supersaturation, but nucleation is generally capable of generating edges at a far greater rate.

The nature and distribution of these sites (referred to as "kink" or "K" sites) are more fully described in references 70 and 83, as well as chapter 2, but the key results are the distance between kink sites on the edge of growing islands, $x_0(\sigma)$, and the distance between the edges of growing islands $y_0(\sigma)$. Together these give the 2D density of addition sites on a crystal face [71]:

$$[B] \propto (x_0 y_0)^{-1} \tag{3.13}$$

where

$$(x_0 y_0)^{-1} = \frac{(\sigma+1)^{1/2}(\ln(\sigma+1))}{19a^2(\gamma/k_B T)} e^{\gamma/k_B T} \tag{3.14}$$

for lattice site spacing a, and edge energy γ. Taylor series expansion of the numerator allows the approximation $(\sigma+1)^{1/2}(\ln(\sigma+1)) \approx \sigma$. Variation due to the temperature/edge energy term γ/k_BT is only 3% in the temperature range tested and is neglected here.

We therefore have:

$$[B] = \frac{A}{h}\frac{\sigma}{19a^2(\gamma/k_BT)e^{-\gamma/k_BT}} = m\sigma \tag{3.15}$$

for growth face area A and lattice step height h, combining all σ-independent terms into the constant m. The dependence of the addition rate on supersaturation is then given by the relations:

$$\phi(T) = k_+[FF][B] - k_-[B] \tag{3.16}$$

$$= [B](k_+[FF] - k_-) \tag{3.17}$$

$$= m\sigma(k_+([FF] - [FF]_{eq})) \tag{3.18}$$

$$= k'_+c^*\sigma^2 \tag{3.19}$$

for a concentration of addition sites [B], on and off rates $k_{+,-}$. Taking together the components of the rate constant, the result is a parabolic rate dependence on supersaturation:

$$R_g = k_2\sigma^2 \tag{3.20}$$

3.3.3 Kinetic prefactors and activation energies

Both scenarios therefore lead to an equation of the form $R_g = k_n\sigma^{n_c}$. The exponent of n_c = 1.9 that we have found experimentally at room temperature lies in between the exponents predicted for the two models described above, $11/6 < 1.9 < 2$. Therefore, while the data clearly demonstrate the cooperative nature of the rate-determining step at the crystal face, it is not possible based on this data alone to discriminate between the nucleation and

incorporation-limited scenarios. The two different models predict that the exponent of σ is temperature-independent (incorporation-limited) or weakly temperature-dependent. For small values of σ, the term $\exp(-K_e/\log(1+\sigma))$ is not treatable as constant, and leads through the temperature-dependence of $K_e{=}\frac{\pi}{3}\left(\frac{\gamma}{k_BT}\right)^2$ to a temperature dependence of the exponent of σ. Due to low growth rates in these regimes, approximations based on power laws remain sound within experimental error. Detailed numerical analysis of the temperature dependence, assuming constant γ=0.70, yields that K_e changes from 0.49 to 0.59 in the temperature range from 290 to 320 K, leading to a maximal variation of n_c between 1.79 and 1.87.), as long as the system is below the so-called roughening transition, which marks the transition into a linear growth regime [70].

Together with our measurements of the temperature dependence of the critical concentration, we are therefore able to calculate the effective supersaturation at all temperatures and hence to determine the temperature dependence of k_n. Figure 3.4 shows the natural logarithm of $\mathrm{k}_n = \frac{R_g}{\sigma^{n_c}}$ as a function of the inverse absolute temperature (Arrhenius plot) and it is found, for all models, that there is a significant dependence of k_n on temperature, increasing significantly with increasing temperature suggesting that the growth of FF assemblies is an activated process with an apparent activation energy of 55 kJ/mol for this model. Therefore, the growth of diphenylalanine crystals is a thermally activated process, very much like the elongation of amyloid fibrils [124]. The interpretation of this activation enthalpy, however, depends on the structure of the growth rate constant k_n. Analytical expressions have been given for k_e and k_2 as [71]:

$$k_e = 2a\nu_{\mathrm{in}}(K_{ad}c_sV_m)^{4/3}\exp\left(-\frac{\gamma}{k_BT}\right) \tag{3.21}$$

for k_2 when the rate is limited by the integration into kink sites [71]:

$$k_{2,in} = \frac{0.1a\nu_{\mathrm{in}}k_BT}{\gamma}K_{\mathrm{ad}}c_sV_m\exp\left(-\frac{\gamma}{kT}\right) \tag{3.22}$$

Therefore, the temperature dependence of the crystal growth rate that we have determined is a combination of the temperature dependence of the rate of incorporation of the molecule into a kink site, ν_{in}, of the surface adsorption equilibrium constant K_{ad}, of the edge energy γ

$= a^2\tau$ (where τ is the surface tension) and potentially also of the rates of surface adsorption ν_{ad} and surface diffusion ν_{sd}. Using the relationships $\nu_i = \nu_0 \exp\left(-\frac{\Delta G_i^{\ddagger}}{RT}\right)$, $\mathrm{K_{ad}} = \exp\left(-\frac{\Delta G_i^{0}}{RT}\right)$ and $\exp\left(-\frac{\gamma}{k_B T}\right) = \exp\left(-\frac{N_A \gamma}{RT}\right)$, we can write all the possible rate constants in the form k_i $= \mathrm{A}_i \cdot \mathrm{e}^{-\frac{\Delta G_i^{\ddagger}}{RT}}$. In particular, we obtain:

$$A_e = 2a\nu_0 (c_s V_m)^{4/3} \tag{3.23}$$

$$\Delta G_e^{\ddagger} = 1/3 \Delta G_{nuc}^{*} + \Delta G_{\mathrm{in}}^{\ddagger} + 4/3 \Delta G_{ad}^{0} + N_A \gamma \tag{3.24}$$

as well as

$$A_{2,in} = 0.1 a \nu_0 c_s V_m k_B T / \gamma \tag{3.25}$$

$$\Delta G_{2,in}^{\ddagger} = \Delta G_{\mathrm{in}}^{\ddagger} + \Delta G_{ad}^{0} + N_A \gamma \tag{3.26}$$

whereby we have decided to partition all of the exponential terms into the barrier-part of the rate equation and all the other terms into the pre-factor. It has to be noted that other partitionings are possible; for example the case of the nucleation component of the activation energy in equation 3.24- this component has a concentration dependence, but behaves as an activation energy- the work done on formation of a critical nucleus against the edge energy. The prefactor A can be calculated to within an order of magnitude from known quantities, given the expressions above- from the crystal structure, we take a = 5.46 Å [56]. The solubility c_s at room temperature is 0.76 g/l = 2.44 mM. The density can be computed from the structure and is 1.05 g/cm^3 and therefore the molar volume V_m is 0.30 l/mol. The frequency ν_0 corresponds to the Eyring prefactor, $\nu_0 = \frac{k_B T}{h} = 6.15 \cdot 10^{12}$. The largest uncertainty lies in the factor $\frac{\gamma}{k_B T}$. A fit to the exponential model of our kinetic data at room temperature has yielded $\frac{\gamma_{\mathrm{ax}}}{k_B T} = 0.7 \pm 0.03$ for axial growth (corresponding to K_e = 0.52; see also footnote on page 7) and $\frac{\gamma_{\mathrm{rad}}}{k_B T} = 1.2 \pm 0.12$ for radial growth [123]. A relatively modest change in this quantity therefore leads to a dramatic difference in relative growth rate. As a consequence, we assume for our estimate of the pre-factor that $0.2 < \frac{\gamma}{k_B T} < 2$. Together with our measurements of the absolute growth rate $\mathrm{R}_g(\sigma)$, we can then compute the magnitude of the free energy barrier using the empirical exponent n_c 1.9, according to:

$$\Delta G^{\ddagger} = -RT \log\left(\frac{A\sigma^{1.9}}{R_g(\sigma)}\right) \tag{3.27}$$

. Furthermore, we can then determine the entropy of activation from $\Delta\ S^{\ddagger} = \frac{\Delta H^{\ddagger} - \Delta G^{\ddagger}}{T}$. The results of this analysis are compared with those of figure 3.4. The free energy barrier computed in this fashion is considerably higher, 32.0 $^{+0.9}_{-4.9}$) kJ/mol at 295K. The enthalpic barrier, calculated from the Arrhenius plot, is reasonably robust to model variations, and this is found to be 55.5±5.5 kJ/mol, resulting in an entropic barrier component ($T\Delta S$) of -23.5$^{+6.0}_{-10.8}$ kJ/mol, an entropy of activation of -79.7$^{+20.3}_{-36.6}$ J/mol/K.

The result in figure 3.4 is calculated analogously to those of the amyloid fibril, with the prefactor being diffusional in origin- however, a different choice of prefactor based on the above reasoning suggests a far higher free energy of activation when it is defined in terms of crystal growth processes. These are compared in figure 3.5.

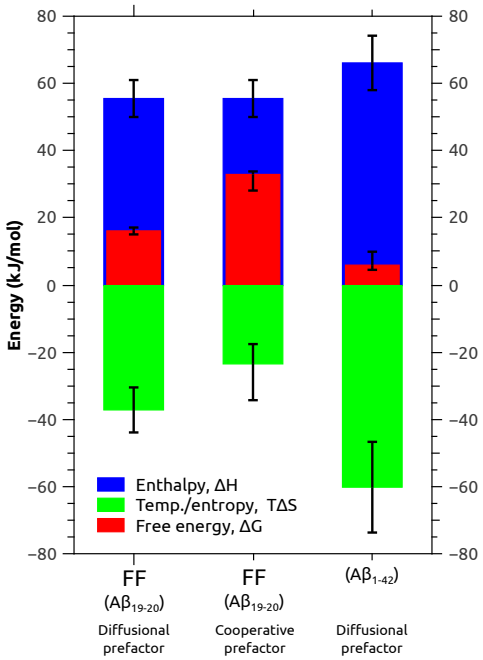

Figure 3.5: Column 1) Contributions to free energy of FF addition, based on a diffusional prefactor. Column 2) Contributions to FF addition, based on the cooperative prefactor A_e. Column 3) Contributions to the addition of $A\beta_(1-42)$ to its aggregate.

A final comment is that it is impossible to ascribe the observed barrier to any one elementary process- inspection of equations 3.26 and 3.24 shows how the exponential terms,

here taken as components of the barrier, are very similar in both cases and indeed both are sums.

3.4 Conclusions

Burial of hydrophobic residues and the aromatic pi-stacking interactions are important determinants of structure in the crystals of diphenylalanine, but these must be considered secondary to the hydrogen-bond networks formed within the channels. Instantly apparent from the crystal structure given by Görbitz [1] is the "cis" arrangement of the bulky phenyl groups, the walls of the nanochannels being described by the peptide linkages and the ionic termini. F1G substitution will certainly result in a different crystal structure, but in all cases it is expected that the water sites, if any, in the crystal will not be in contact with aromatic side-chain sites, and further that the aromatic species will self-associate in the nucleus and in the mature crystal.

Interestingly, Baldwin's empirical power law relationship between the free energy of fibril elongation and the hydrophobic surface area does seem to hold, with adjustments, down to the smallest polypeptides possible. The data in that paper is concerned explicitly with fibrillisation, whereas FF, GF, GG crystallise, as does GNNQQNY under certain conditions [55], the crystal of GNNQQNY differing marginally in chain conformation from the amyloid fibril it is also capable of forming. Protein structures display close packing comparable to that in molecular crystals [125], however the absence of the termini from the close-packed "core" region in many longer polypeptides will lead to deviation from contact area scaling.

The magnitude of hydrophobic effects displays significant size dependence. For small species, such as the isolated R-groups of the hydrophobic amino acids, the key parameter determining the strength of the hydrophobic effect is the area of the hydrophobic species [126]. Here, we see this effect clearly demonstrated for the short species investigated, from 2 to 17

peptide units in length, from three dimensional crystals [1] to fibrillar amyloid aggregates. Hydrophobicity is a common driving force to all these aggregation processes. We find that the thermodynamics of the self-assembly of the FF peptide displays the typical signature expected for the burial of hydrophobic residues: the driving force for assembly is entropic in nature at low temperatures and becomes enthalpic at higher temperatures. Furthermore, even though the free energy of assembly is more favourable than expected from a general scaling law relationship derived for longer sequences, the deviation can be explained through the strong sequence bias of this aromatic dipeptide.

Detailed analysis of the free energy barrier to aggregation of diphenylalanine is complicated by the fact that the process of FF aggregation is highly cooperative (as detailed in Chapter 2). Depending on the model used to represent the process, variations can be observed in the values returned, though here it is notable that the results returned by both the nucleation-and-spread mechanism and by the model where the spread, i.e. the incorporation, is the sole limiting step, are closely comparable. This is to a degree understandable in the similar nature of the two processes at moderate supersaturation, comparison of the contributions to the free energy in equations 3.24 and 3.26 show that there is little variation besides than the complicated nucleation barrier, which becomes small at higher supersaturations. The addition-limited rate can be thought of as a limiting case of the nucleation-and-spread rate, as might be expected- the nuclei that form on the face obviously must themselves spread, and the measurement R_g, the ensemble measurement used to define rate of reaction in the paradigm of the Arrhenius activation energy, is a composite of all additions to the growth face. Indeed, when measured in this fashion (addition rate per site, per second) nucleation and spread are *parallel*, rather than sequential, processes. Both the appearance of a critical nucleus on the growth face and addition to an edge are necessary and sufficient to advance the growth face by one unit. As such, the processes cannot be deconvoluted based on the data we have at present.

Interestingly, the enthalpic component of the barrier to the aggregation of FF and the parent Aβ polypeptides is of similar magnitude- it has been observed previously that acti-

vation enthalpy tends to scale linearly with polypeptide chain length due to simple addition of more interactions, in particular, but not limited to, solute-solvent hydrogen bonding and hydrophobic solvation [124]. Further, no tertiary structure is present in solvated FF, a small molecule with few internal contacts. The deviation of FF from this relationship is noted, but in light of the far-ranging differences in the aggregation process and hence the contributions to the free energy of aggregation, direct comparison is difficult.

I suggest that these fundamental differences in the nature of the process of aggregation limits the application of experimental results based on oligopeptides of as few as two amino acids to systems involving much longer chains. The presence of internal degrees of freedom and extensive intramolecular hydrogen bonding leading to tertiary structure are all significant contributors to the stability, or otherwise, of native proteins in solution. These contributions are absent in the dipeptides, which in solution will exist in rapidly interconverting conformations. The distribution and directionality of intermolecular interactions in the aggregate state is also far more uniform in the case of the dipeptides, as opposed to the longer chains. The crystal structures of unsubstituted dipeptides are diverse, but invariably involve extended 2D or 3D networks mediated through hydrogen bonding chains (see chapter 5) and charge-charge interactions at the termini. [110]. The interaction energies along all three crystalline axes are, while disparate enough to yield significant growth rate differences on the axial and radial faces [123] are not enough to cause departure from conventional crystalline order, that is, a well-defined unit cell repeated indefinitely in all three dimensions.

Chapter 4

Structural transitions and Ostwald's step rule in N-tertbutyloxycarbonyl-diphenylalanine

4.1 Introduction

Studies of diphenylalanine alone lead naturally to investigations into the structure and properties of self-assembled aggregates of modified, or substituted, derivatives of the dipeptide [2, 127, 66]. These include the protected dipeptides N-fluorenylmethoxycarbonyl-FF (Fmoc-FF) and N-tertbutyloxycarbonyl-FF (Boc-FF) commonly used in peptide synthesis. Both are distinguished from the parent dipeptide by the presence of a bulky and hydrophobic substituent at the N-terminus.

In this chapter, I show that Boc-FF displays a range of structures in a ternary system consisting of the substituted dipeptide, water, and ethanol. Thermodynamic and morpho-

logical investigations of the structures sequentially formed by this FF derivative give a clear demonstration of Ostwald's step rule [128]. Spherical, filamentous and fibrillar morphologies are commonly observed for supramolecular structures from peptides [129, 130], although the characterisation of structural transitions linking such phases has heretofore remained elusive- in this chapter it is shown that the processes are sequentially nucleated. In chapter 2 a route to kinetic control of morphology was demonstrated- in that case, it was strictly the aspect ratio of important microstructural scaffolds that was controlled. Here, the overall morphology- a spherical suspension, a continuous fibrillar phase, and a crystalline, needle-like precipitate, can be controlled through modification of reaction times and conditions.

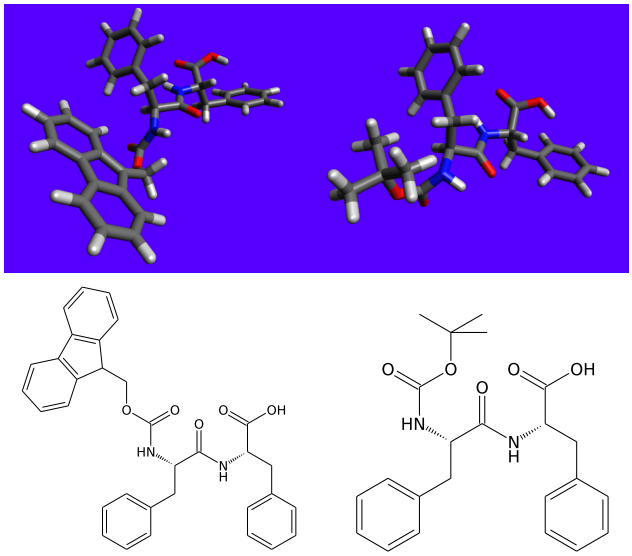

Figure 4.1: Structure and diagram of Fmoc-FF (left) and Boc-FF (right). Both are derivatised at the N-terminus by bulky hydrophobic groups. Both Boc- and Fmoc- are used as amine protecting groups in solid phase peptide synthesis, and their steric bulk renders them incapable of incorporating into the crystal of the parent dipeptide FF. Upper images rendered in Avogadro 1.0.3[18].

Fmoc-FF is known to form persistent hydrogels in water on change of temperature, pH or solvent conditions [131, 132]. The morphology of these hydrogels is a mesh of 10-30 nm diameter fibres, having an FTIR signal suggesting the presence of β-sheet type contacts between neighbouring molecules in the aggregate (interestingly, in contrast to FF itself, as discussed in chapter 5) [133]. Boc-FF is capable of self-assembly into structurally distinct states on nanometer length scales as a result of variations in the solvent composition in which the process occurs. Rapid dispersal of a highly concentrated stock solution (in HFIP) of the substituted dipeptide in water yields needle-like crystals with an axial hollow core. These crystalline structures are of course reminiscent of FF itself, but are found by FTIR to have an amide I band peak corresponding to that of an α-helix [102] at 1662/cm, in contrast to FF

itself which has its amide I peak at 1686/cm [58], a region typically associated with β-sheet structures, though FF has important structural deviations from the β-sheet arrangement common to amyloid fibril.

More gradual dispersal of a less concentrated solution in ethanol yields a suspension of microspheres, these microspheres having remarkable, metallic-range stiffness in the dry state [13], but only a slight degree of crystalline order. The final stable state of a mixed aqueous/ethanolic solution of the protected dipeptide is the crystalline tubular structure, and in this section it is shown that two identifiable and separable intermediate polymorphs are formed before the tubular structures nucleate. The existence of the second intermediate phase, a gel-like structure displaying some crystalline order and extreme shear sensitivity, was unknown prior to this investigation. Taken together, these results represent a first demonstration of Ostwald's step rule in diphenylalanine-based systems.

4.2 Phase behaviour and stability

I noted that the Boc-FF/water/ethanol mixtures were effectively a ternary system, in contrast to studies on FF involving HFIP where the initial solvent was deemed to be present at sufficiently low concentration to not perturb the morphology of the crystals. The correspondence between the observed morphology [1] where the dipeptide was crystallised from evaporating aqueous solution, and where it was precipitated by HFIP [59] is convincing, though it was shown that the presence of HFIP does indeed perturb at least the solubility equilibrium [56]. To survey the roles of water, ethanol and Boc-FF concentration on the intermediate and final state of the system, a phase diagram of the system was prepared showing the appearance (spherical/rodlike) of the observed Boc-FF aggregates, if any, in suspension.

This snapshot of a phase diagram shows the extended metastability of the spherical

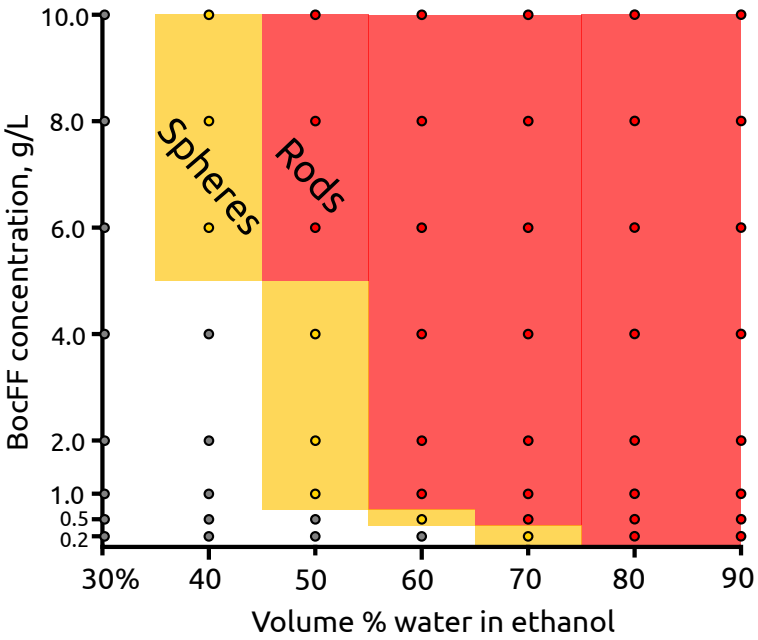

Figure 4.2: Phase diagram of the Boc-FF/water/ethanol system, after standing at 295K for 60 minutes. Circles represent concentrations that were used, colours represent the regions of the phase diagram to the resolution allowed by the survey. Yellow regions represent a dispersion of the spherical aggregates, however it must be noted that only rodlike crystallites were present in these samples after 24 hours. Red- rodlike crystallites, yellow- spherical structures, white- isotropic solution (no phase separation) at 1 hour.

dispersion. On injection of stock solutions into water, the spheres may persist for hours in the absence of mechanical disturbance, this lifetime being dependent on concentration and solvent composition. They are not found to be stable indefinitely- all solutions will on standing yield a precipitate of the rodlike crystals. Both of these species are well known, the spheres being characterised in reference 13 and the rodlike, tubular crystals being first described earlier [102]. However, transitions between the phases had only recently been observed by coworkers.

The transformation between the phases was then observed using time-lapse optical microscopy, with the samples sealed in glass capillaries to prevent evaporation. The data in Figure 4.3 show that the spheres initially present in such systems are progressively replaced by a heretofore unknown fibrillar species after incubation in a glass capillary for ca. 30 minutes. The fibrillar phase is found to be localised initially at a single point, seen as filamentous aggregates by light microscopy, but is observed to spread progressively in space. Dissolution of the spheres is observed to occur in the vicinity of this growing network of fibrils, resulting in the quantitative conversion over time of the Boc-FF from the spheres to the filamentous form of self assembled structures. Shortly after the emergence of the filamentous phase, thicker tubular structures are observed to form. Tube nucleation is seen to be spatially correlated with the presence of filamentous aggregates of the fibrillar phase (Figure 4.3)

Tube nucleation is seen to be spatially correlated with the presence of filamentous aggregates of the fibrillar phase, which are visible in Figure 4.3 throughout, initially appearing in the central and upper-right regions of the micrograph, with the crystals nucleating in the upper-right region. I was able to isolate this previously unrecorded aggregate of Boc-FF from suspensions of spheres as they start to dissolve, and it was found to be somewhat more easily obtained from cooled solutions. Suspensions of the spheres (1.0-2.0 g/L) were prepared at 4°C and were then centrifuged for 15 minutes under 12000g, and were then allowed to stand at that temperature for a further 15 minutes. This yielded an optically homogeneous (to the naked eye), thin gel with remarkable shear sensitivity, any agitation resulting in immediate nucleation of the crystalline phase. Knowing that crystalline order must appear at some

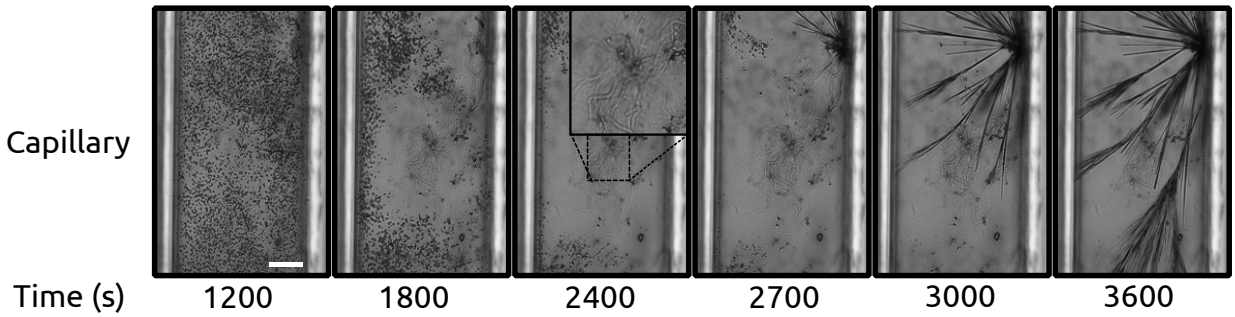

Figure 4.3: Timelapse optical microscopy of a region within a sealed glass capillary, containing a 1.0g/L dispersion of Boc-FF in a 10% v/v ethanol in water solution. Scale bar at 1200s is 50μm, that in the inset (2400s) is 20μm. 1200-1800 seconds after mixing, an initial uniform dispersion of the spheres is seen to begin to dissolve in a specific region, being replaced by an optically uniform region that develops apparently fibrillar anisotropies. At 1800 seconds, this fibrillar morphology is obvious and seems to display features with relatively tight radii of curvature compared to familiar Boc-FF crystals. At 2400 seconds (30 min), the spheres have almost vanished in the observed region, replaced by the new, low optical density phase. Around 2700 seconds, tubes nucleate close to a region where the fibrillar phase initially appeared, and grow continuously with branching. *Micrographs and test run prepared by Dr. Aviad Levin*

point between the formation of tubes and spheres, I sought to test the gel phase for crystallinity by means of X-ray diffraction. A sample was lyophilised and X-ray diffractograms were recorded for each of the isolated phases.

The spherical species, after removal of solvent, show a diffraction pattern typical of amorphous materials, with two broad halos. The diffraction pattern of samples of the gel phase, however, differs considerably from that of the spherical species, with flattening and partial resolution of the broad peaks centered at $2\theta = 8°$ and 19°. While the gel itself can be seen to be devoid of ordered crystallinity, the further peaks of a low amplitude in the fibrillar phase are likely to be due to the presence of small quantities of tubular crystals, see below. The diffraction patterns demonstrate that the spherical and filaments structures are both largely amorphous in nature, but that the short-range order present in each type of structure is different. The tubular structures are, however, crystalline as shown by their diffraction pattern which exhibits distinct sharp peaks with high intensity.

Figure 4.4c demonstrates the reason for the optical clarity of the gel phase, the average diameter of individual fibrils being about 30 nm and therefore being unresolvable by light microscopy unless sufficient fibrils are bundled, or the refractive index is significantly changed by the presence of the aggregate across a larger area.

Nucleation is a rare event and, as such, is expected to be statistically suppressed in small volumes [134, 135]. The phase transition from spheres to tubes occurs reproducibly within 30-45 minutes in droplet volumes approaching those of the bulk solution (average droplet volume = 7 nl), yet when encapsulated in picolitre droplets (average droplet volume = 300 pl), the spheres are stable for significantly longer periods of time without undergoing a phase transition. Indeed, in the droplets with the largest volumes the phase transition from spheres to tubes is detectable after 30-45 min, in the low volume microdroplets the spheres remain present at all times monitored in the experiments [136]. These observations show that the formation of the fibrillar phase is significantly suppressed in small volumes and therefore has the characteristics of a nucleated process [134]. Also notably absent is the tubular phase.

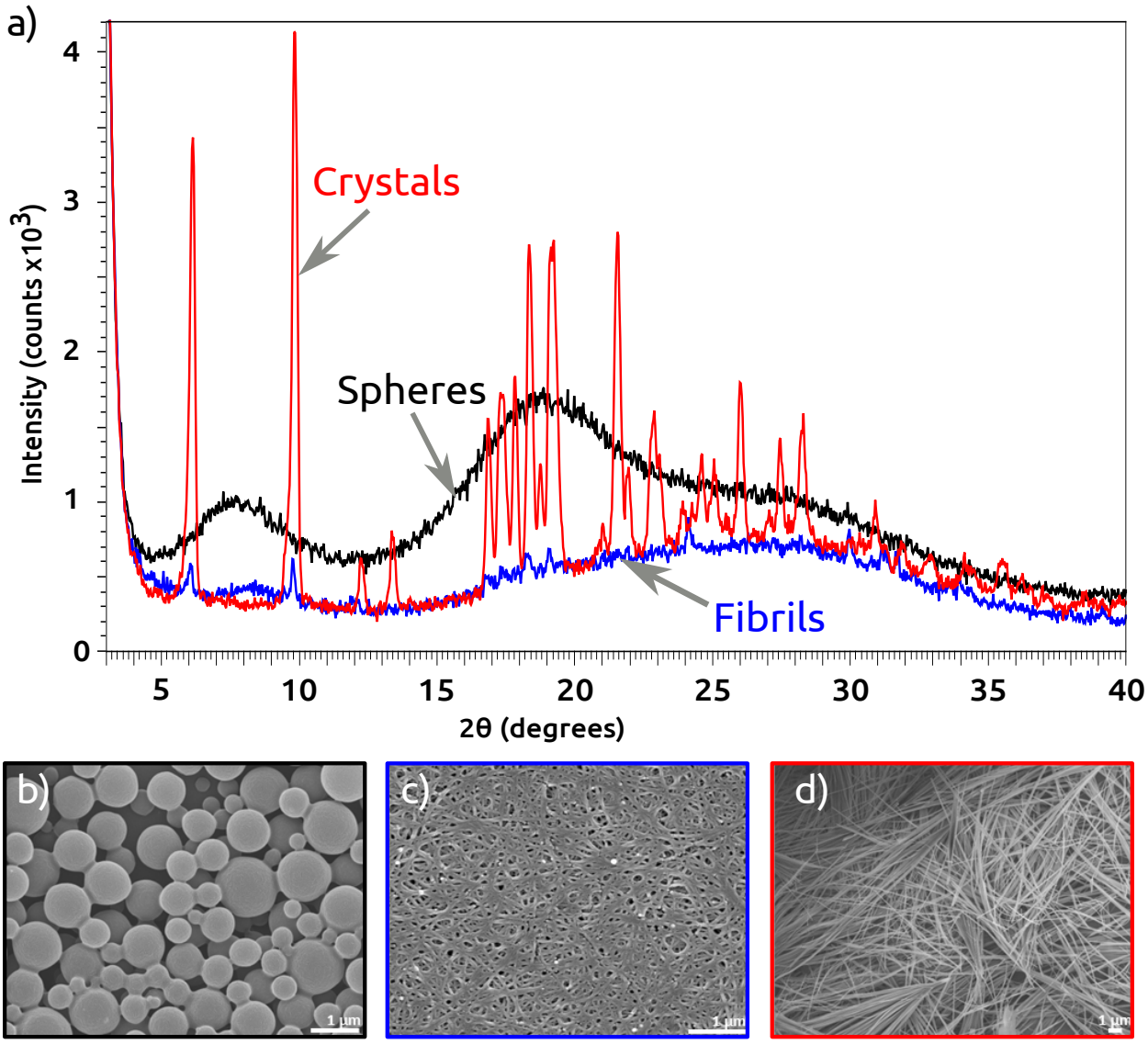

Figure 4.4: a) Powder X-ray diffraction data, 2θ ranging from 3-40°. Immediately apparent is the crystalline structure of the tubes, with sharp well-defined peaks. The spheres are observed to be amorphous, with broad, low peaks centred on 8, 19 and 27 degrees. The gel phase gives some evidence of crystalline order, with peaks observed that do not obviously correspond to peaks appearing in the diffractogram of the tubes (24 and 30 degrees), while other peaks are common to both gel and tube, suggesting some contamination of one by the other. b,c,d) SEM images of the three phases, prepared by rapidly drying samples on a glass coverslip at 2, 40 and 60 minutes after mixing. Samples prepared and imaged by Dr. Or Berger following protocol mentioned in the text.

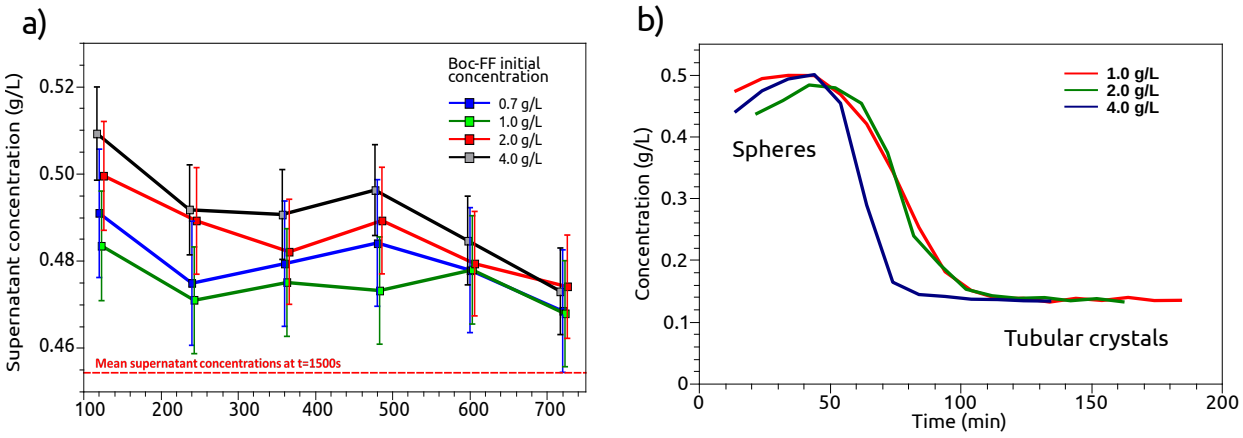

Figure 4.5: a) Concentration of free Boc-FF in supernatant 120-720 seconds following mixing and nucleation of spheres. Despite a wide variation in initial concentration, the supernatant concentrations following mixing are very similar. b) Concentration of free Boc-FF as measured by NMR for three different initial concentrations. Nucleation lag time is closely comparable for all samples.

Following the rapid initial formation of spheres, these structures were observed progressively to change size over a time scale of minutes (Figure 4.6a). This behavior can be attributed to Ostwald ripening [137, 138]. This process, due to the difference in stability between highly curved surfaces on smaller particles and the flatter surfaces of larger ones (the Gibbs-Thomson effect) results in the growth of larger particles at the expense of smaller particles, which redissolve.

For processes where monomer addition to the growing aggregates is limited by surface processes rather than diffusion in the solution, the average particle size changes according to the relationship [139, 140]$\langle R(t)^2\rangle - \langle R(0)^2\rangle \propto t$, where t is the time and $R(t)$ is the radius of the particle at time t. Under that mechanism, a linear relationship between the square of the average change in particle size and the time of incubation is indicative of an Ostwald ripening process in which the rate of monomer addition is limited by surface processes. Also notable is the increase in the polydispersity of the sample- as is demonstrated in figure 4.6a, the distribution of particle radii becomes far larger. This is again typical of Ostwald ripening, which will tend to result in the shrinking of small particles and the growth of larger ones.

Figure 4.5a shows that this increase in size is not coming about through incorporation of free monomer from solution, as the supernatant concentration is roughly constant throughout the time period measured. The change in the average particle size cannot be accounted for by depletion of monomer from solution but rather as a result of a redistribution of mass between the particles through Ostwald ripening, or through a process of surface-directed recrystallisation [141, 142].

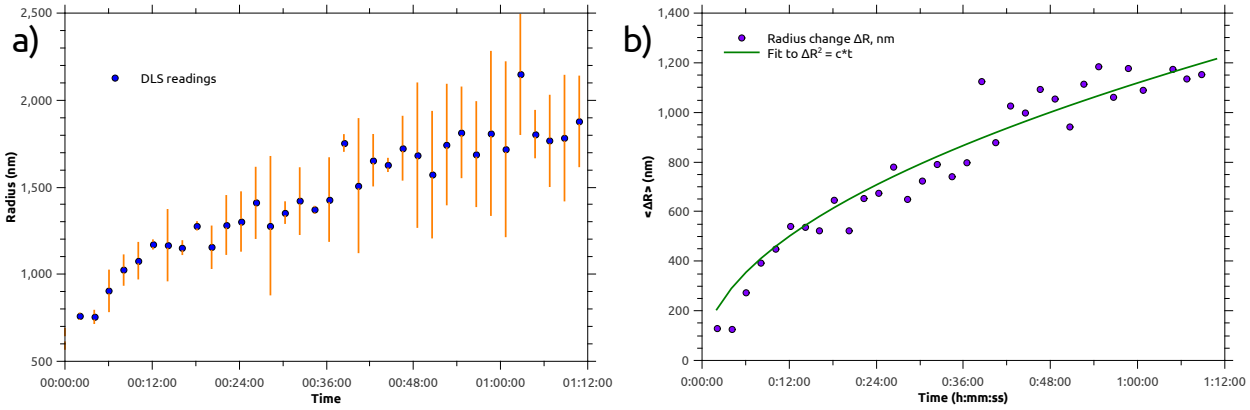

Figure 4.6: a) DLS data for a suspension of BocFF in water at a concentration of 2.0 g/L. Orange bars are the standard deviation of the calculated radii. b) Mean hydrodynamic radius of a sphere suspension over time, showing sub-linear scaling of rate of change, typical of Ostwald ripening processes.

It was suggested that the time-dependent variation in size, or indeed the phase transition from a spherical suspension to the extended gel network, may be due to coalescence between spheres in suspension. In order to confirm or deny the hypothesis, zeta-potential measurements were taken to establish the strength of the repulsive barrier to particle coalescence due to charge effects. We found that over the first five minutes after formation, the average ζ-potential of the system was observed to remain constant within experimental error at -73 $\pm$2 mV, a much larger value than the commonly assumed to be the threshold for stability, ca. 25 mV. This large value indicates that the spheres form a highly stable colloidal suspension and that coalescence of the particles is strongly suppressed.

Kinetic assays for evaluating the rate of sphere-to-tube rearrangement were performed

through spatially resolved optical density measurements monitoring the variance as a function of time between the absorbance at multiple points separated by a distance of 1.2 mm on a square grid. The optical density of a suspension of spheres was found initially to be, on average, uniform throughout the sample, however, a transition from this uniform density as spheres to a markedly inhomogeneous suspension as tubes was observed to take place over time, Figure 4.7. It is immediately apparent, however, that the time taken for the system to overcome the barrier presented by the rearrangement is markedly abbreviated. This provides evidence that agitation, such as those arising from rapid movements of the plate over the reader, tend to result in nucleation of the tubular phase from the gel phase- charge-charge repulsions, such as those between worm-like micelles, are strong but are overcome in the short range by strongly attractive van der Waals interactions.

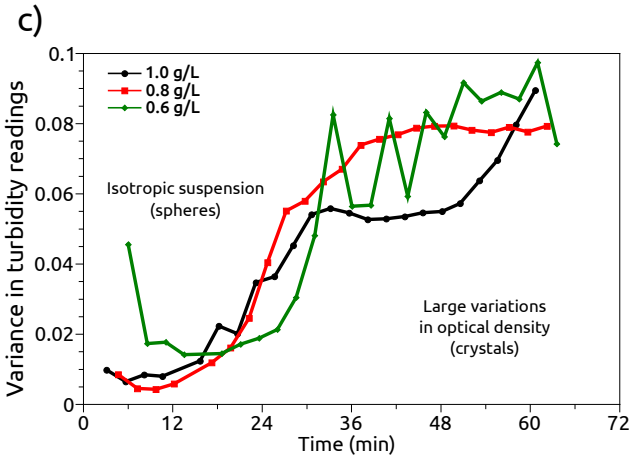

Figure 4.7: Variance (σ^2) of optical density readings across 9 points separated by 1.2mm on a square grid within individual wells of a standard volume 96-well plate. Spherical suspensions are isotropic, while condensation into tubular structures gives rise to "light" and "dark" regions.

In the presence of the spheres, the free monomer concentration was evaluated to be 0.52 g/L, while at the end of the reaction, when all the spheres had converted into tubes, a concentration of 0.14 g/L was measured by NMR. While we cannot distinguish between free monomers, which did not take part in the assembly of each of the various structures and the structural units released from assemblies in transition, the free monomer concentration in the solution was seen to be reduced as the assembly of further, more stable structures, occurs (4.5b). This observation clearly indicates that formation of the tubular phase depletes the previously free monomers in solution, and in addition the "off rate", the rate at which monomer leaves the spheres, remains constant while the "on rate", the rate at which spheres incorporate incoming monomer, drops sharply as the supernatant concentration decreases

below the critical concentration, at which point the on rate and off rate are equal. The decrease is made possible by the lower chemical potential of the newly present crystalline phase, which provides a sink. This is a clear demonstration that the transition is governed by Ostwald's step rule.

Equation 3.1 gives the relationship between a critical concentration and a free energy of aggregation. It is found that the critical concentrations of Boc-FF in the 10% ethanol-water solution for the spherical suspension and the crystal are, respectively, 0.52 g/L and 0.14 g/L. This corresponds to a free energy of aggregation into the spherical suspension of -16.3 kJ/mol, and into the crystal of -19.6 kJ/mol. The free energy of the resolvation of the spheres, nucleation of the gel phase and transition to the final, thermodynamic product is the difference between these figures, a relatively small -3.2kJ/mol. I must also add that the value for the spherical phase must be considered as an upper bound- nucleation of the gel phase occurs during a process of Ostwald ripening and the phase boundary between spheres and solution still has a considerable area at this point, contributing a positive free energy relative to surfaces with lower curvature.

This phase transition process was monitored at 0.75 g/L peptide concentration by differential scanning calorimetry. Using this method, the exothermic or endothermic processes leading to the phase transition between spheres and tubes could be followed by comparing the heat changes taking place in a 1:10 ethanol to water solution containing 0.75 g/L Boc-FF compared to a control solution devoid of the peptide (a simple solution of ethanol in water). The data show [136] a release of heat at a time corresponding to the observed transition from spheres to tubes by microscopy, indicating that the transition from spheres to tubes is exothermic in the temperature range investigated (10-20°C) with $\Delta H_{s,t} = -21 \pm 2.1$ kJ/mol and that the apparent heat capacity of the reaction is negligible. The exotherm (and compensating entropy cost) is unsurprising- the glassy, amorphous spheres of figure 4.4 are replaced by a system displaying long-range order, mediated through strong intermolecular interactions. An overall loss of entropy occurs (-83 J/mol/K).

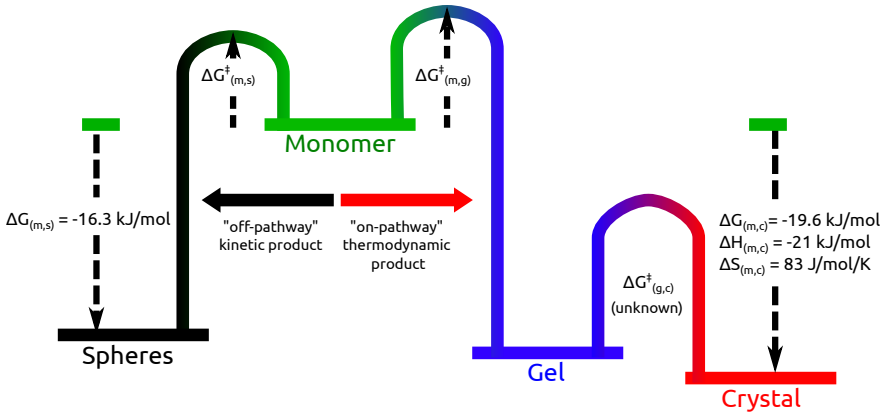

Figure 4.8: Thermodynamics of Boc-FF aggregation based on results in reference 136. The crystals are a thermodynamic product, while the spheres are a kinetic product. The barrier to the formation of the on-pathway gel and crystal phases is higher than that to the formation of the spheres, and this is seen first. The spheres undergo Ostwald ripening (lowering their free energy) but a gel phase nucleates and sinks monomer, causing dissolution of the spheres. The gel is ephemeral and nucleates tubes, probably via a structural rearrangement.

A multi-step phase transition process underlies the supramolecular assembly of Boc-FF peptides, and this transition exhibits series of identifiable phases, from spheres to gel to tubes. The results indicate that the spheres, previously envisioned as distinct end-products of a solvent-induced self-assembly process [102, 13], can undergo a structural rearrangement mediated by nucleation of a new phase and subsequent transport through solution. The spheres formed in suspension are rigid and resistant to shear, however on a timescale corresponding to the earliest possible appearance fo the gel phase, the system proceeds to the rod-like phase rapidly under agitation (Figure 4.5c). The sphere as isolated dry for mechanical testing in reference 13 appear broadly similar to spheres in suspension, based on the persistence of the sphere phase during viscometry testing. This study confirmed that the spheres are non-crystalline, the PXRD (Figure 4.4a) being devoid of peaks, instead displaying two broad halos suggesting a glassy structure. It was theorised during this study that the spheres in suspension may contain excess ethanol relative to the surrounding solution due to favourable interaction parameters and that diffusion or dispersal of this excess may play a role in the phase transition. However, NMR relaxation time measurement was inconclusive

on the internal structure of the spheres.

For possible typology of the phases observed, the crystalline solid is familiar, being analogous to the corresponding phases of the parent dipeptide FF and displaying typical properties of crystalline solids, for example a well-resolved powder X-ray diffractogram. The spheres and gel phase, however, are more enigmatic. In figure 4.6, the absence of amphiphilic aggregates in FF solutions is clearly demonstrated. In the case of BocFF, however, the spheres display many of the characteristics of such solutions, including a particularly high ζ potential suggesting an outward orientation of the acidic moieties and corresponding burial of the bulky and hydrophobic Boc group and aromatic rings. The desolvation due to injection into water may be a major kinetic structural determinant leading to a densely-packed surface. Nanotubular and vesicular structures in solution are well-known for peptide-based amphiphiles, with hepta- and octapeptides of the form X_6D and X_6DD where X is A, L or V [143], and polyglycine-based penta- to decapeptides [144] forming micellar aggregates and indeed wormlike extended micelles, a possible structure for the elusive gel phase. The spheres, however, are mechanically stable, ruling out a vesicular or similar semi-liquid structure.

The propensity of the gel phase to undergo shear-induced nucleation, as observed in Figure 4.5c, where nucleation lag time is greatly and uniformly reduced, and reduced to a timescale comparable to that corresponding to the first appearance of the gel phase in quiescent systems, is a property in common with many native proteins [145]. The tendency of shear forces to trigger aggregation is also associated with surface effects [146], in particular those due to hydrophobicity [147]. These forces, however, which have a magnitude dependent on the radius of the species on which they act, are relatively feeble at the scale of monomeric proteins, and more feeble still in the case of small molecules such as Boc-FF [148]. However, where polypeptides, for example, silk fibroin undergo self-assembly in solution to give amphiphilic aggregates, these aggregates by virtue of their greater size are far more susceptible to mechanical shear, the disruption of these structures being thought to play a major role in the nucleation of the β-sheet rich silk fibril [149, 150]. The unstable aggregates of Boc-FF

observed in this study therefore represent a potential model for shear sensitivity studies in biological systems.

4.3 Conclusions

The results of the investigation of Boc-FF indicate that the spheres are initially formed through a rapid condensation in the solution phase, and then undergo a process of Ostwald ripening over a longer time scale, and finally convert, in an exothermic reaction, into the thermodynamically most stable crystalline form. Zeta potential measurement rules out the possibility that the formation of the fibrillar states is achieved by coalescence of spheres, small volume experiments conversely suggest that it is a nucleated process. Other forces acting on the system include a potential inhomogeneous distribution of the two other components of the ternary system, water and ethanol. It is possible, given the absence of internal structure in the spheres when rapidly dried, that the interior of the spheres is liquid in suspension, perhaps solvated by ethanol retained during the rapid original formation of the interface between the Boc-FF-rich spheres and the surrounding solution. Capillary experiments, though, seem to suggest that the spheres do not rearrange into other phases [136], rather that the gel phase nucleates independently. There is further evidence for this in the NMR timecourse, where the nucleation lag time of the gel phase is virtually independent of the number concentration of spheres.

The Boc-FF crystal and its precursor forms exemplify a thermodynamic process distinct from that of the aggregation process of the parent dipeptide. It has been demonstrated in chapter 3 that FF has no pre-crystalline solution structure- no persistent aggregation occurs prior to the nucleation process, after which the growth processes take over. There seem to be no lasting non-specific interactions between FF molecules in the FF-water system- they are either monomeric, or a sufficient number of them cluster, forming a nucleus that grows into the one crystalline form. Boc-FF demonstrates a fascinating process of sequential

nucleations of progressively more stable structures. Similarly, during the aggregation of longer polypeptides, the effect of solvent environment through hydrophobic desolvation can lead to amorphous aggregation, with specific, higher-enthalpy interactions forming on longer timescales to give the final mature fibril [151, 152]. However, not all oligomeric aggregates formed through non-specific interaction are aggregation competent, and formation of these "off-pathway" oligomers can actually slow amyloid growth, even as monomer concentration increases [153].

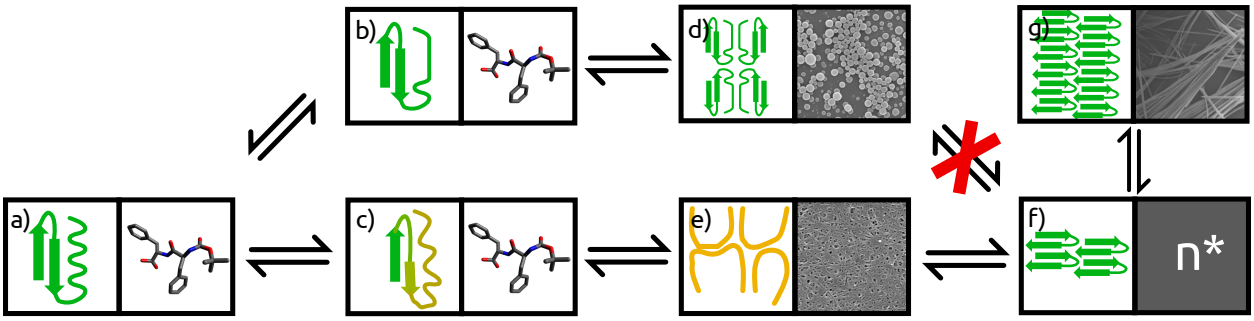

Figure 4.9: Map of generic amyloid aggregation, based on that in reference 154, with potentially comparable BocFF phases included. I do not include the nucleation-growth pathway from the original, which is dependent on an internal transition of a polypeptide chain. a) Native monomeric protein. b) "Native-like" protein. c) Partially unfolded protein. *In the case of BocFF, a,b,c are entirely equivalent- all monomeric states of BocFF are effectively interchangeable due to a low barrier to conformational change.* d) "Native-like" aggregates, off the aggregation pathway- no transition occurs to amyloid/crystal critical nucleus (f). The comparison is made to the spherical phase. e) On-pathway aggregate with short-range order, capable of structural reorganisation into the amyloid. The comparison is made to the gel phase. f) Minimal amyloid nucleus. Compared with the critical nucleus for nucleation of the crystal phase. g) Amyloid fibril/BocFF crystal.

A question then naturally arises as to whether conclusions drawn from the mechanism and thermodynamics of BocFF aggregation can be generalised to the aggregation of amyloid fibrils. It is known that the process of fibrillogenesis involves the emergence of transient oligomeric species [101, 155], and that these are capable of rearranging to give amyloid fibril [156]. This process, in which a less stable aggregate nucleates first, is in accordance

with the step rule [157], and so a direct comparison can be drawn between a diphenylalanine system and full-length polypeptides. A question arises as to internal degrees of freedom, once again- if we seek to superpose the phase changes of BocFF onto those of an amyloid system such as in figure 4.9, we must do so knowing that the "aggregation competent" state of BocFF is determined far more by its concentration- cooperative effects- than by any sort of solution-phase conformational change the dipeptide may undergo. Any process dependent on early structural triggers within monomers, in particular folding and misfolding, cannot be sensibly modelled with dipeptides. Figure 4.9a,b,c are different states on potentially different pathways for an amyloid-forming polypeptide, but are indistinguishable for BocFF.

In the spherical suspension, we have many of the descriptors of an off-pathway aggregate [154, 158]- it is an easily isolable, discontinuous solid phase that is nonetheless structurally distinct from the fibril. It has a higher free energy than the state with long-range order, and the pathway from the spheres to the crystal is mediated by nucleation of a new phase [136] rather than any transition of the spheres themselves. The spheres and the oligomers are therefore off-pathway aggregates, kinetic products arising in accordance with the step rule. The gel phase can be similarly contextualised in terms of known stages of amyloid fibril formation as an "on-pathway" aggregate- the gel phase is clearly nucleation competent and the shear sensitivity is strongly suggestive of a process involving structural rearrangement to form the nucleus of the crystal (Figure 4.9e-f), and must be higher in free energy than the crystal. Little is known about the quantitative thermodynamics of this phase, as it has not been distinguished by calorimetry [136], but the observed reaction pathway would suggest that it is lower in free energy than the spherical suspension (formation of the gel causes dissolution of the spheres), but displays a higher barrier to formation (the Ostwald step rule). Its free energy of formation from the monomer must be between -16.3 and -19.6 kJ/mol, and it has a low barrier to rearrangement into the crystal.

In chapter 5, materials science and mechanical applications of the parent dipeptide are explored. While this chapter has concerned itself with crystalline, unmodified FF, a stable aggregate and a thermodynamic product, the isolation of *kinetic* products of dipeptide aggre-

gation opens paths to a far wider range of functional microstructures than would otherwise be possible.

Chapter 5

Applications in materials science- the effect of solvent environment on self-assembly

5.1 Introduction

Bioinspired nanomaterials represent a growing field of study and application, especially those composed of amyloid aggregates. These structures are tolerant to a wide range of conditions, with typically low kinetic solubility *in vivo* [159]. Amyloid aggregates composed of synthetic polypeptides, designed for specific interactions and surface functionality can display a wider range of material properties than fibrils formed from naturally-occurring protein.

It was noted [135] that the fibrils formed by shorter peptides display greater mechanical stability than those of longer species, in line with previous work [63] which found that longer

polypeptides tended to have a lower free energy of fibril elongation, arising from frustration of intermolecular interactions in the aggregate.

Diphenylalanine displays one of the greatest mechanical stabilities for any peptide-based nanostructure [9], displaying strength and Young's modulus comparable to bone [160]. Also advantageous is its low cost, and its rapid and simple preparation. However, limitations of its use include the relatively fixed morphology and the inability to functionalise the material prior to assembly, both due to its state as a small molecule crystal. Nonetheless, decoration of FF nanostructure surfaces has been achieved through covalent linking with biotin [67] and through introduction of a cysteinyl derivative (FFC) to surface sites [5]. Both post-assembly strategies potentially remain open to unmodified FF crystals displaying different morphologies. This chapter is concerned with the structural potential of the unmodified FF system, explored through variation of solvent environment.

The most common method of preparation of FF microcrystals for nanotechnological applications is the dilution of a stock solution of FF in hexafluoroisopropanol (typically 100 g/l, 321 mM) at a ratio of 1:50 in water, producing a fine suspension of visible crystallites within seconds [2]. The stability of the crystals in water [10, 72] and other solvents [72] has been discussed in some recent studies [10, 72] and it has been shown that below a certain total concentration of peptide, the crystals can be redissolved in water, resolving the conflicting reports on their water-solubility [10, 72].

Hexafluoroisopropanol (HFIP) is an excellent solvent for biomolecules by virtue of the strong hydrogen bonds formed between the fluoroalcohol donor and heteroatom acceptors on the solute. The presence of this solvent in trace amounts can cause problems in work involving biological systems; it is capable of thinning phospholipid bilayers, a process confounding investigations of the role of synthetic amyloid fibrils in processes involving membranes [161]. In addition, HFIP is highly volatile and it is therefore difficult to handle small volumes of highly concentrated solutions of diphenylalanine close to saturation.

The ability of HFIP to solvate the dipeptide at concentrations of 100 g/l could however also be expected from other species capable of forming strong hydrogen bonds. In particular, it was hypothesised that select common organic solvents would possess this ability. It is found that kinetics and morphology are strongly influenced by the solvent conditions and we present alternatives to HFIP/water for the preparation of FF assemblies, a novel crystal structure due to crystallisation from non-aqueous media, and a range of solvents suitable for the construction of persistent nanoscale structures due to the low solubility of FF in these conditions.

5.2 Results and discussion

5.2.1 Solubilities

In order to explore the solubility of FF in solvents other than the HFIP commonly used for FF self-assembly to date, we selected an array of organic solvents with varying capacity as hydrogen bond donors and acceptors and varying dielectric constant and determined the critical concentration of FF in each one of these solvents. The critical concentrations are shown in Table 5.1.

The solvents are grouped according to an indication of their use in nanotechnological applications; those solvents capable of dissolving more than 10 g/L of FF are useful for the preparation of stock solutions and in the disassembly of tubular structures following use as temporary scaffolds or moulds for nanowires. Of note here is the remarkable capacity of glacial acetic acid, capable of dissolving in excess of 400 g/L (433 g/L, 1.38M) of the dipeptide. Acetic acid is the strongest acid tested, and in order to determine the effect of pH on the solubility, a solution of HCl was prepared at the same pH as a 2% v/v acetic acid

Solvent	Structure	Solubility (g/L)		Solvent solubility in water (g/L)
Hexanes		0.002	±0.001	Very low
Diethyl ether		0.062	± 0.003	69
Methylene chloride		0.088	± 0.002	13
Chloroform		0.148	± 0.003	8
Acetonitrile		0.193	± 0.006	Miscible
Ethyl acetate		0.59	± 0.035	8.3
2-Propanol		0.080	± 0.002	Miscible
1-Butanol		0.210	± 0.002	Miscible
1-Propanol		0.290	± 0.005	Miscible
Hexanol		0.33	± 0.017	Miscible
t-Butanol (30°C)		0.37	± 0.019	Miscible
Water		0.76	± 0.008	Miscible
Ethanol		0.89	± 0.019	Miscible
Water +2% HFIP		0.92	± 0.016	N/A
HCl solution, pH 2.58		1.47	± 0.044	N/A
Water +2% acetic acid		2.38	± 0.069	N/A
Acetone		4.2	± 0.152	Miscible
Methanol		10	± 0.099	Miscible
Formamide		33	± 1.07	Miscible
Phenol (46°C)		130	± 5.7	8.3
HFIP		240	± 11.5	Miscible
Acetic acid		430	± 15.7	Miscible

Table 5.1: The solubility of diphenylalanine in a range of different solvents. Error is standard deviation of 5 trials for each solvent.

solution (2.58) and the FF solubility was found to be significantly lower, indicating specific interaction between the acetic acid and the solute.

In particular, acetic acid has the advantages over HFIP of being nontoxic, easily handled and readily available, in addition to a far greater capacity rendering high dilution ratios capable of producing a supercritical FF concentration in water. It should be noted that the volume of the solution on introduction of 400 g/l FF increases by a factor of 1.3- hence the volume added is 0.65% for a final FF concentration of 2 g/l.

5.2.2 Moderate solubility- water-like systems

Solvents displaying moderate capacity, that is, exhibiting an FF solubility roughly within an order of magnitude of that of water, represent a potential field for further study of the role of solvent in the self-assembly process. All the aliphatic alcohols other than isopropanol (0.08 g/L, $2.6 \cdot 10^{-4}$M) tested here displayed moderate solubility, and the morphology of the resulting crystallites is shown below in figure 5.1.

It is known that water is associated with amine protons and carboxylate termini in the nanochannels in the crystal structure in an ordered arrangement conducive to study by X-ray diffraction. Alkoxy protons have similar electron densities to those of water, however, with increasing alkyl chain length the nanochannels will be less able to satisfy all possible hydrogen bonding interactions with the solvent due to the steric bulk of the chains.

The alcohol displaying the highest solubility, methanol, is primarily notable as the most polar alcohol (dielectric constant 33 vs 24 for ethanol), and short chain alcohols display low surface tensions; in addition to potential interactions between alkyl chains and the benzyl residues, the energetic cost of forming a cavity in the solvent into which the hydrophobic

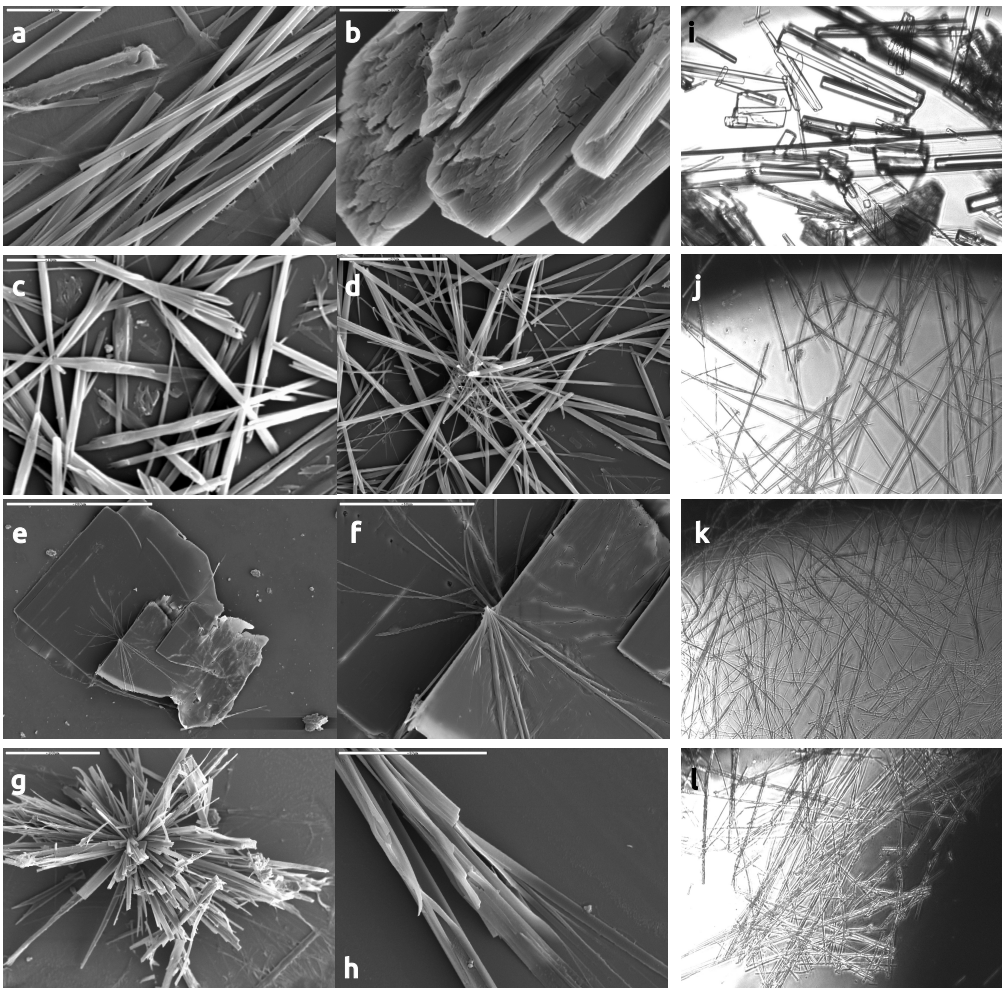

Figure 5.1: Crystal morphologies arising from crystallisation in different solvents investigated by scanning electron microscopy. a) Microcrystals grown from methanol, scale bar 10 μm. b) Detail of larger crystal grown from methanol, scale bar 10 μm. c) Microcrystals grown from ethanol, scale bar 20 μm. d) Detail of ethanol microcrystals demonstrating hollow cores, scale bar 10 μm. e) Lamellar structure from isopropanol, scale bar 200 μm. f) Detail of edge of IPA crystal, scale bar 50 μm. g) Crystals grown from common nucleation site in n-propanol, scale bar 100 μm. h) Detail of n-propanol crystal, scale bar 50μm. i [MeOH], j [EtOH], k [i-PrOH], l [n-PrOH]) Corresponding light microscopy images. Width of each image is 832μm. Visible in (j) are the filiform crystallites precipitated from isopropanol, lamellar crystals are absent in this image.

species can be introduced is far lower than in water [162]. Solvophobic effects are therefore less important in alcohols. However, it is noted that the major product of nearly all crystallisations from aliphatic alcohols are highly anisotropic filiform or rod-like structures.

SEM images of the crystals as grown from the alcohols were obtained, displaying a wide variation in habit. Particularly surprising is the square lamellar form obtained from isopropanol, this form coexisting with extremely fine filiform crystallites. In bulk solution, these lamellar crystals often serve as nucleation points for extremely large numbers of such crystallites. Evidence of this process can be seen in the image 5.1, (f), where filiform crystallites (Figure 5.1, (k)) extend from the edges of the lamellae. The crystals as grown from ethanol seem to display the closest morphological similarity to the water-grown crystals- indeed, in some of the images it is possible to make out a number of crystallites with hollow cores.

5.2.3 Methanol

Crystallisation of the dipeptide by the slow cooling of a saturated methanol solution produced a large number of whisker-like crystallites, superficially similar in morphology to those produced by a similar procedure in water. However, it was noted that the water-grown crystals are unstable in even saturated methanol solution, being rapidly dissolved through radial cracks (Figure 5.2). The SEM images above demonstrate the absence of a hollow core from the crystallites, suggesting that the crystals as formed in methanol represent a new solvomorph.

The structure of the crystals grown from methanol solution was investigated via X-ray diffraction from a single crystal measuring 50 x 100 x 700 μm. Comparison was made with a crystal grown from water, the result of which agreed with the previous work by Görbitz [3]. The results of the methanol experiment are given in Figure 5.3.

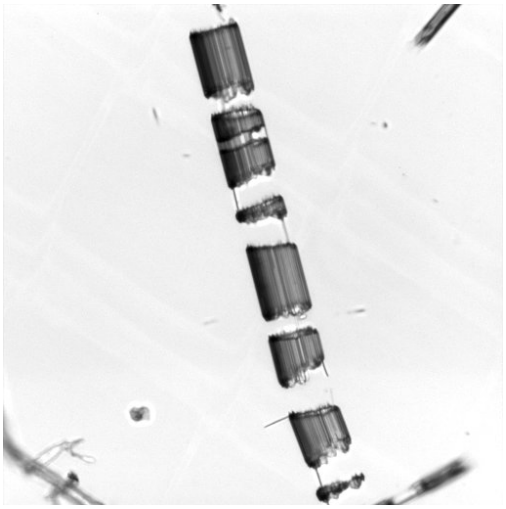

Figure 5.2: Water grown crystals exposed to saturated methanol solution decompose via solvation at particular sites on the radial face of the crystals, resulting in the breaking of the crystallite into multiple sections

Another important difference is the burial of the peptide bond and the exposure of the benzyl side chains to cocrystallised solvent. The crystal habit is similar, and the unit cell of similar dimension, with the peptide bonds once again oriented parallel to the long axis of the crystal, indicating the relative strength of the peptide and ammono-carboxylate interactions relative to the radial π stacking interactions, here present in a familiar herringbone arrangement.

In both systems, methanol and water, the hydrogen bonds between amide groups (NH$\cdots$OC) are parallel to the long axis of the crystal. The face to which these strong, directional interactions are normal will be a high energy face, and so in accordance with the Gibbs-Wulff theorem [43], this face will be much further from the centroid of the crystal at equilibrium [98]. Radial interactions are far weaker than axial interactions, giving rise to the observed morphology.

Exposure to the solvent differs in the two solvomorphs- while in water-grown crystals the channels are broad and are composed of the peptide bonds and the ionic groups, the

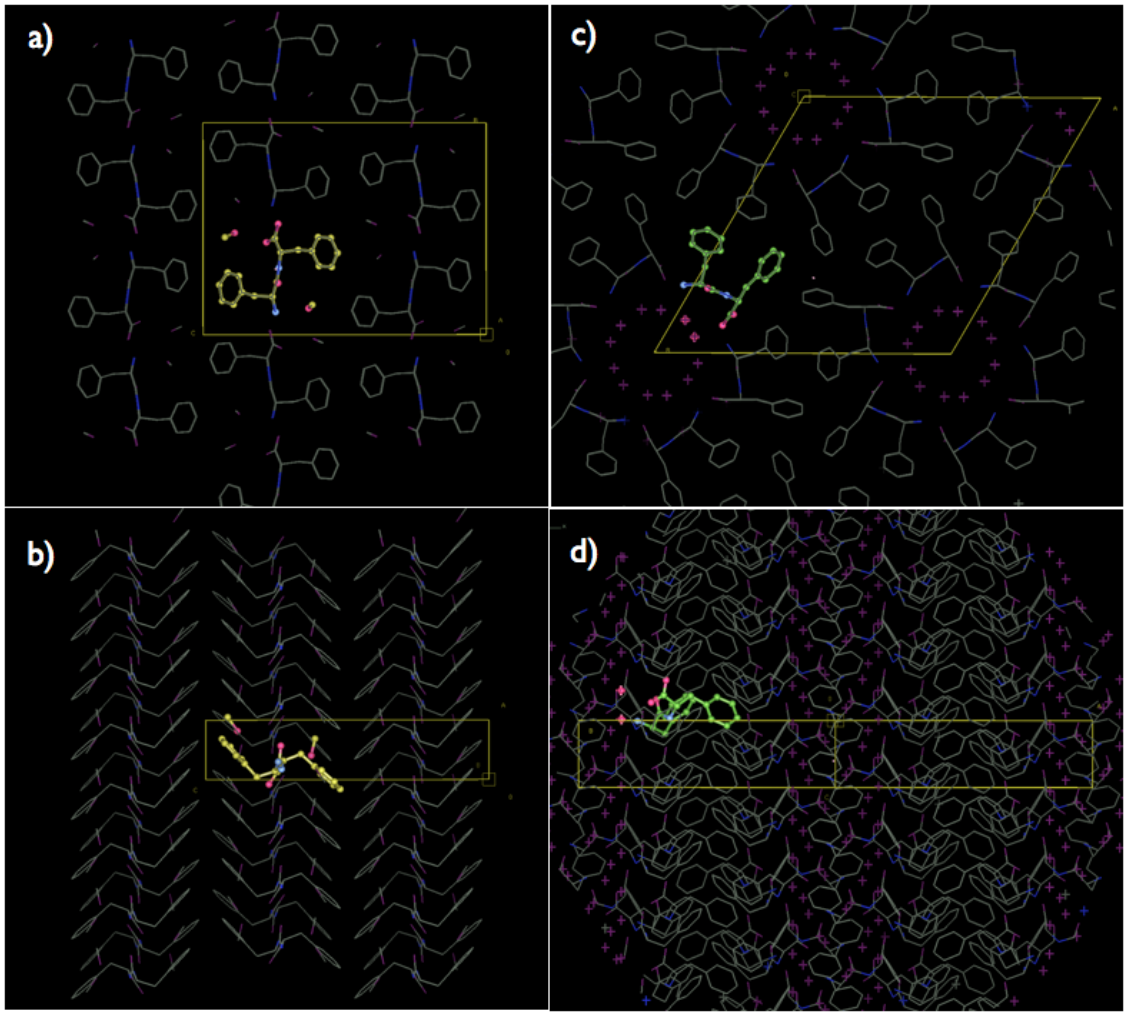

Figure 5.3: The view of the unit cell and molecular packing of FF-methanol and FF-water crystal structures. The contents of the asymmetric unit are shown as ball-and-stick models and coloured yellow in FF-methanol structure; green in FF-water structure. The water molecules are shown as red crosses and the methanol molecules as stick models. The hydrogen atoms are not shown. a) FF-methanol structure as viewed along the a axis and b) along b axis. c) FF-water structure as viewed along the c axis and d) along the diagonal between a and b axis.

solvent positions in the methanol grown crystals display contact between the methyl group of methanol and the benzyl R-group. Methanol is self-associated on its sites via hydrogen bonding, there being no void in the structure.

The effect of increased solvophobicity in water as opposed to methanol [163] is demonstrated through the conformation of the two R-groups- in the water system these are "cis" to the central peptide linkage, ensuring burial within solvent-inaccessible areas, whereas in methanol the groups are on opposing sides of the plane described by the RCONHR' group. Hydrogen bonding interactions are visible in the methanol crystal, between the ionic termini and the methanol proton.

In light of the new crystal structure solved for methanol-FF, the habit of the crystals grown from n-propanol (Figure 5.1, (g)) is interesting- the crystals can be seen to display the familiar needle-like habit, again with rectangular cross section and an absence of hollow cores, similar to methanol-grown crystals.

5.2.4 The crystal structure of aromatic dipeptides

It has been known for some time that hydrophobic dipeptides display highly unusual crystal structures- a comprehensive statistical study [108] of hydrogen bond connectivity in oligopeptide structures gives four distinct orderings of the hydrogen bonds between the constituent molecules. Which pattern is observed is determined by the identity of the dipeptide R-groups, both in terms of their simple steric interactions (to establish close packing) and any preferred orientation displayed by the R-groups, in particular the quadrupole interactions of aromatic sidechains. These crystals are commonly highly anisotropic, often appearing as needles [1].

By far the most common observed structural motif was the eight-membered chain, denoted as C(8), corresponding to a "head to tail" arrangement of the dipeptide backbones- the eight members of the chain being those of the backbone itself. It was absent only in rare cases, one being the aromatic dipeptide YW (tyrosyltryptophan), described in a 2008 paper by the same author [109]. The crystal structure of this dipeptide, memorably referred to in the paper as a "Big Mac" structure, displays the familiar segregation of the hydrophobic

species, and indeed segregation between the two aromatic substituents, with the tryptophan residues and tyrosine residues occupying different layers in between hydrophilic layers bordered by the amide and charged termini. This layer structure is also interesting in that it displays hydrogen bonding (albeit weak) between the ammonium terminus and the aromatic tyrosine ring.

The first study to elucidate the crystal structure of diphenylalanine was that by Görbitz in 2001 [1], as part of a series of X-ray diffraction experiments on the aggregate state of hydrophobic dipeptides. The structure of FF was found to be invariant with respect to the size of the aggregate, that is, no polymorphism was observed for the water-grown structures [3, 59]. High resolution X-ray diffraction data, carried out at low temperature and "freezing" the channel water molecules in place, further confirmed the structure given by Görbitz [56].

The original paper discusses the pattern of hydrogen bonding within the crystals, finding extended "chains" of hydrogen bonds in the hydrophilic channels. This is remarked upon as a significant structure director, in FF this phenomenon is visible as two helical C(8) patterns- one right handed, and one unit cell in length, the other left handed and five unit cells in length. Remaining hydrogen bonds from the charged termini of the dipeptides are satisfied by the presence of the water in the channels. Görbitz mentions the absence of hydrogen bonding at the peptide carbonyl in FF.

Other studies in reference 1 are dipeptides of leucine and phenylalanine- both the homodipeptides and FL and LF. These are grouped together by their internal hydrogen-bond connectivity, the arrangement of the eight-membered chains being similar in all cases (though the left-handed helix in LL, LF and FL is only three unit cells in vertical dimension). All of these dipeptides also display a hydrophilic/hydrophobic segregation pattern, with the water-filled channels similar to those observed in FF.

Interestingly, the structure where the crystals are grown from methanol solution do not display these channels- the less hydrophilic solvent being able to interact with the aromatic residues and also (to an extent) to satisfy the hydrogen bonding requirements of the polar termini. The hydrogen bonding chains in this structure are a repeating unit of 8 atoms and a perpendicular repeat of 4 atoms from backbone amide hydrogen bonding. Also visible in the crystal structure is the effect of the aromatic quadrupoles on the side chain interactions. Whereas FF-H_2O displays the "T-shape" or herringbone type packing, FF-CH_3OH displays the "staggered" arrangement of aromatic substituents.

In both water and methanol-grown crystals of FF, and indeed in the other dipeptide structures studied by Görbitz, there is an extended hydrogen-bonded "backbone" in each structure, this interaction being a strong (but variable, depending on the side chains) determinant of the crystal structure and the presence or absence of solvent molecules in the unit cell. An extended hydrogen bond system is also, of course, the ubiquitous property of amyloid polypeptide aggregates, in the form of an extended, interstrand beta-sheet type

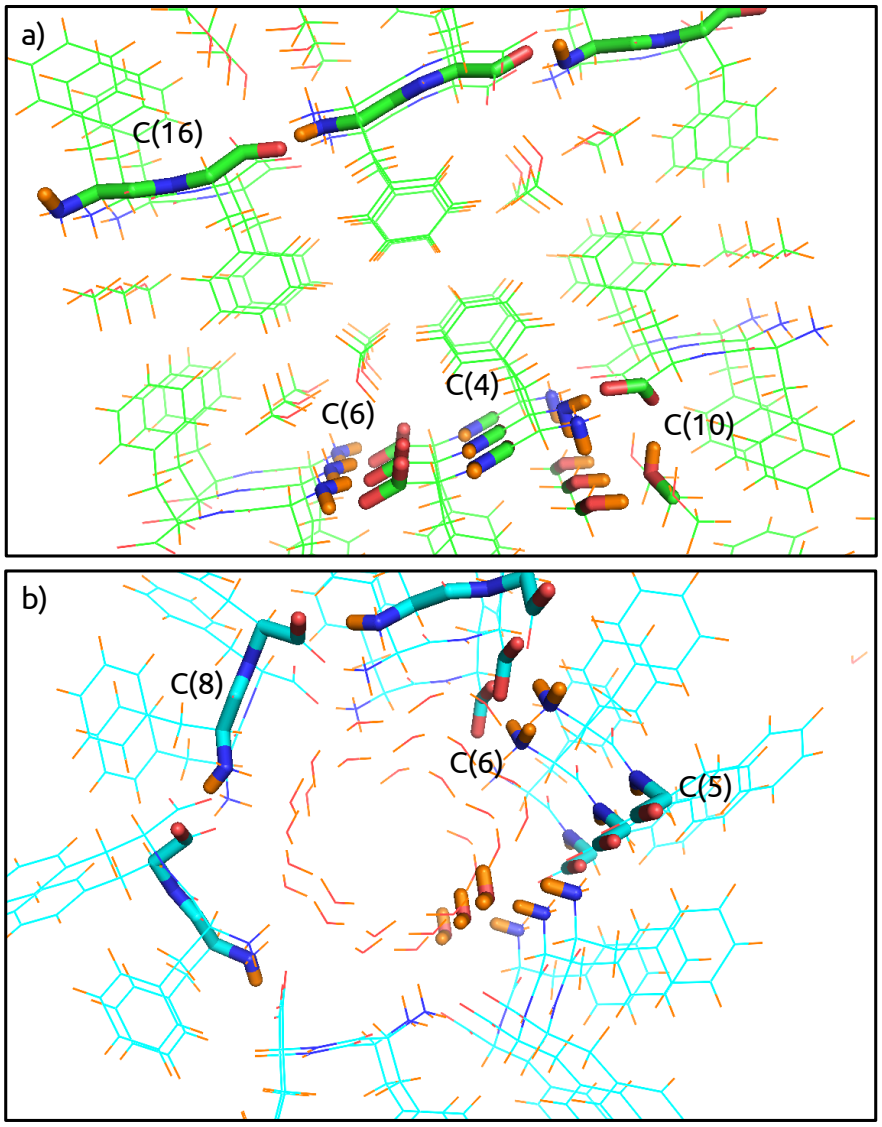

Figure 5.4: a) Crystal structure of the diphenylalanine dipeptide, as the methanol solvate, looking down the [001] direction. Carbon green, nitrogen blue, hydrogen orange and oxygen red. Hydrogen bond chains are highlighted by thicker lines. A C(16) pattern is present, as are amide-amide interactions forming a four-membered repeat. Charged termini form a C(6) chain and a helical arrangement involving two methanol molecules is visible in the helical C(10) to the bottom right. b) Crystal structure of the diphenylalanine dipeptide as grown from water, looking down [0001], as in references 56, 1. No C(4) amide pattern is apparent, the amide proton interacting instead with the terminal carboxylate (C(5)). One of the eight-membered chains is highlighted, as is the common six-membered terminal interactions. The third ammonium proton protrudes into the solvent channel, where it interacts with trapped solvent.

structure. The dipeptide FF, should it display identical intermolecular interactions, both in terms of chemical identity of the species and their precise geometry, would therefore be an interesting model system for the role of aromatics in the aggregation of polypeptides.

A study by Lekprasert et. al. [58] aimed to establish the nature of the hydrogen bond chains within the FF unit cell and to compare them to the established beta-sheet amyloid structure seen in pathological long-peptide aggregation. This was accomplished by Raman spectroscopy, focussing specifically on the amide I and III bands. The frequencies of these bands give some information about the environment of the C=O and N-H amide groups, with a lower frequency absorption being observed where the atoms are involved in hydrogen bonding. Involvement of either the N-H or C=O in hydrogen bonding results in an amide III frequency increase of 22-23/cm, and the amide I band is particularly sensitive to the environment of the carbonyl group, exhibiting a calculated lowering of frequency on hydrogen bonding to the carbonyl of 33/cm [164], and a lowering of 10/cm in case of involvement of the N-H. The observed frequency, at 1690/cm- close to that of the free carbonyl at 1700/cm, was consistent with a picture where the carbonyl was uninvolved in hydrogen bonding, as was suggested previously [1]. This indicates a hydrogen bond connectivity in FF distinct from that in the aggregates of longer polypeptides.

The concept of "periodic bond vectors"- that is, the presence of structure-directing bonding interactions with implications for overall crystal morphology, was mentioned in chapter 1. In figure 5.4 above, a number of these strong bonding interactions can be identified in both the methanol and water solvomorphs- both of these views are nearly parallel to the long axis of the crystal, that is, according to the Gibbs-Wulff theorem, the view is normal to the highest energy face. In figures 5.1 and 1.2, the needle-like habit of both solvomorphs can be observed.

Figure 5.4a shows the hydrogen-bonding patterns in the methanol solvate, and immediately apparent is the arrangement of the bond chain vectors- nearly all, except the C(16)

repeat in the crystallographic c-axis, have vertical (a-axis, axial) bond chain vectors. Immediately from this we can expect either needle-like or lamellar structures, with a tendency towards needles due to the greater number of bond chains in the a-direction.

Figure 5.4b shows the familiar water solvomorph. Here there is, again, an obvious preponderance of axial bond-chain vectors. To make sense of the helical C(8) and its influence, a point is made in reference 46 that any bond chain is only as structure-determining as its weakest (lowest-energy) link. The vector sum of a helix is coaxial with the helix, and the radial components alternate between strong charge/charge interactions in the channels and weak hydrophobic interactions in the interior. This observation further explains the results detailed in chapter 2- the radial faces, being coplanar to a number of strong periodic bond chain vectors, are by far the largest faces of the crystallite once growth is complete. The axial faces have comparatively much smaller areas- the bond chains coplanar with these faces include relatively weak aromatic quadrupole interactions.

5.2.5 High solubility systems

The kinetics of crystal nucleation in acetic acid and HFIP solutions are easily distinguished by the significantly later appearance of crystals on dilution of acetic acid solutions. The interface on addition of acetic acid stock solutions is far more persistent than that on addition of HFIP stock solutions, but still far slower than that on addition of phenol (where the interface is persistent due to finite solubility of phenol in water), visible in figure 5.6.

Solutions at approximately 2 mg/ml final FF concentration were prepared by the injection of a stock solution (122 g/l in HFIP, 186 g/l in acetic acid) into quiescent distilled water at a ratio of 2% by volume in a spectrophotometer measuring absorbance at 300 nm, and the reaction was followed for 10 minutes. On injection of the HFIP stock solution, turbidity was apparent within seconds and the reaction reached completion after less than a minute. The acetic acid solution, however, displayed a significant time delay before reaching maximal

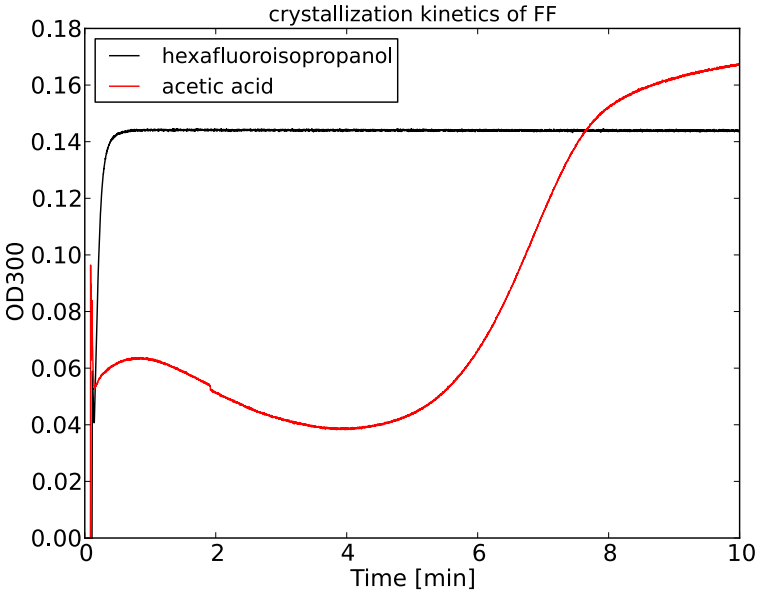

Figure 5.5: Increase in turbidity measured at 300 nm following injection of stock solution sufficient to establish a final solution composition of 2% of the organic solvent and a supersaturation ratio of 2.5 in that system. Crystal formation from acetic acid is significantly slower than from HFIP, due to the stronger interaction of acetic acid with the peptide. The spike after ca. 10s is due to the end of the injection.

turbidity. The turbidity at 300 nm was measured as a function of time following injection (figure 5.5).

The lower rate of assembly in acetic acid can yield interesting morphological differences between crystals precipitated by HFIP dilution or by acetic acid dilution. Those resulting from HFIP dilution are typically small, on the order of tens of microns in length. Those resulting from the dilution of acid stock solutions nucleate at the persistent solution/water interface and grow radially from there, resulting in a wider length distribution with a far greater mean, on the order of millimetres in quiescent solution. These fine, dendritic crystals are frequently seen to originate from one central site, presumably a droplet of the relatively hydrophobic acetic acid/FF solution. The processes are visually compared in figure 5.6.

The low rate of solution of the mixture into water provides a number of possible routes to regular arrangements of crystallites, for example through a microporous membrane separating the water from the stock solution, or through mixture in a microchannel.

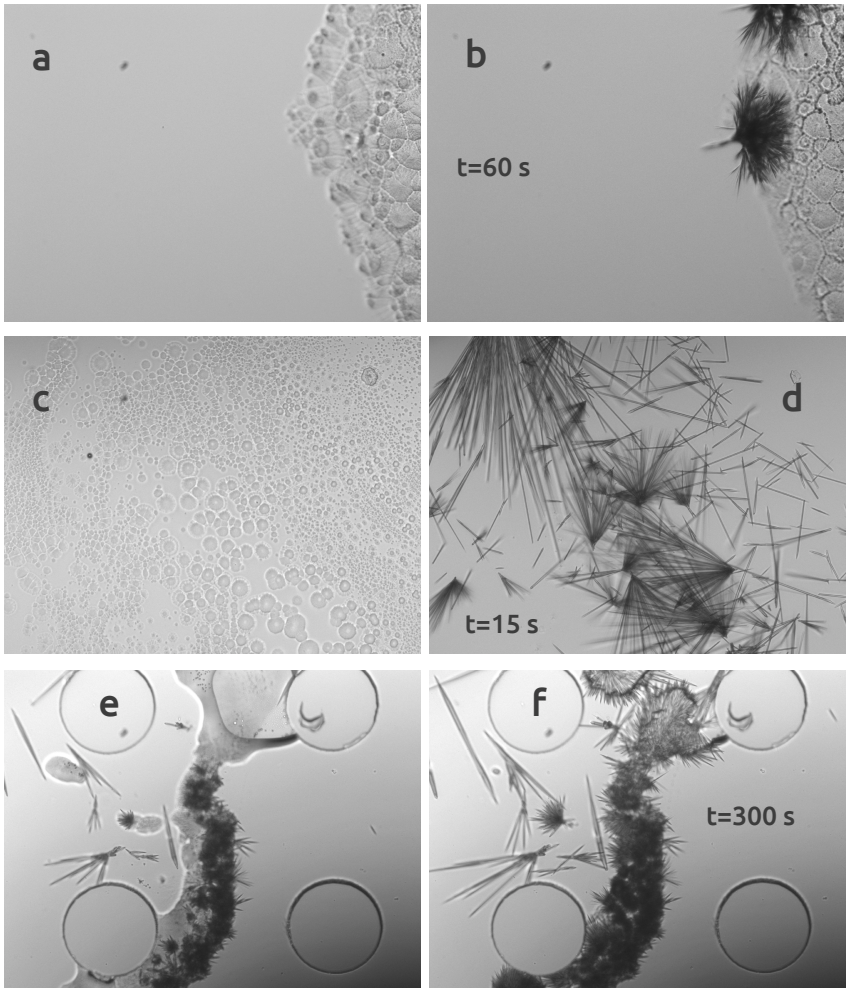

Figure 5.6: Morphological and kinetic differences between the growth of crystals from the dilution of various stock solutions into water. a) Acetic acid, on the right of the image, immediately after contact with water. b) Acetic acid, 60 seconds after contact. Nucleation has occurred at two visible sites. c) HFIP immediately after contact. The fluoroalcohol is dispersed readily and forms small droplets, many of which provide nucleation sites. d) FF crystals forming rapidly from dispersed nucleation sites, 15 seconds later. e) Phenol/water in microfluidic channel (the circular objects being pillars in the channel) Central phase is phenol- and FF-rich. Image taken shortly after initial contact. f) Phenol/water interface 300 seconds later, showing the persistence of the phase boundary and radiating crystallites.

A possible concern when using concentrated acid solutions is that of hydrolysis of the amide, causing the degradation of the dipeptide to the phenylalanine monomer. Analysis of an acetic acid stock solution by thin layer chromatography indicated no presence of monomer on standing at 25°C for two days. Mass spectrometry indicates that it is not hydrolysis, but rather dehydration that is taking place, a result consistent with cyclisation to the diketopiperazine.

The other high capacity solvent systems have some particular features. Formamide, capable of dissolving 30 g/l of the dipeptide, produces gels which collapse to an amorphous mass on standing. Phenol, a solid at room temperature, likely engages in similar hydrogen bonding to that in HFIP. Alone among the high-capacity solvents tested, phenol is only slightly water-soluble, giving a persistent interface on addition to water from which crystallites are capable of growing.

5.2.6 Low solubility systems

Solvents in which the dipeptide is virtually insoluble were notably those having no strong hydrogen bond donors or acceptors5.1. The weak Lewis base diethyl ether, functioning as a hydrogen bond acceptor, displayed marginally greater capability as a solvent than hexanes.

Of interest are the chloromethanes chloroform and particularly methylene chloride, in which the dipeptide is virtually insoluble. MC is of very similar density to the assembled nanostructures, and the low solubility in the compound, taken together with the volatility of the fluid, provides an interesting opening for higher-order structural assembly either through direct manipulation of the crystallites or through functionalisation using amphiphilic surface-attached monolayers.

5.3 Applications in micromechanical systems- release of stored energy

Considering the remarkable mechanical rigidity of diphenylalanine assemblies [8, 9] and their relative ease of preparation, along with their inherent biocompatibility, investigations into the application of the crystals as force transducers were initiated [90]. Through the confinement of the crystals as they undergo rapid growth from a highly concentrated solution, it was found that the energy stored as the chemical potential of the dipeptide in solution could be released as external mechanical work.

This process requires the generation of mechanically metastable systems through the balancing of opposing forces, a motif in biological actuation that is observed in mechanisms for ejection of spores [165]. In this application, the forces in balance are those arising from elastic deformation of FF crystals, and that due to surface tension at a water-fluorocarbon interface. The actuators are triggered by an osmotic modification of the solvent environment of the dipeptide, releasing energy stored in the elastic distortion of the growing crystal. Crucially, this energy is not constant, but is a function of the dimensions of the crystal and the extent of its distortion- it changes with the growth of the crystal, or with the shrinking of its container. As the crystal grows from a highly concentrated solution, the chemical potential of the monomer in solution is stored as the elastic deformation energy of the crystal, being released when the force required to restrain the straightening of the crystal exceeds that which can be applied by the interface [90].

The water/fluorocarbon interface is generated by a microfluidic device operating in a "dripping" regime of shear-induced fluid jet breakup [166, 167], resulting in highly uniform suspensions of an aqueous phase in fluorocarbon oil. The fluorocarbon typically used in these investigations is Fluorinert FC-40 (3M Corporation), and the droplets so produced are stabilised by perfluoropolyether/polyethylene oxide surfactants. These droplets, with

diameters typically in the tens of micrometers, restrict the growing crystals resulting in their buckling.

The experimental details for the application of FF in microscale actuators are given in figure 5.7. A droplet maker is used to create a macroemulsion from two injected, miscible liquids, and this new phase is then separated into isolated droplets by means of the device pictured in figure 5.7a and b. This setup allows for the encapsulation of thermodynamically unstable phases that would react in the bulk- the two miscible components (water, and a highly concentrated stock solution of FF in acetic acid) are only in contact in the short channel between the water/acetic acid junction and the disperse/continuous junction. Once formed, the droplets are reasonably stable and can be transferred as a suspension in the continuous phase into other devices, as in Figure 5.7c. The surface of these droplets then form the restraining force which buckles the crystal, storing elastic energy- as the FF deposits from the supersaturated solution, it will elongate and thicken the crystal (as in chapter 2). Figure 5.7e shows two paths to the triggering of the actuators- path A, which involves radial growth of the crystal, and path B, which requires the crystal to shrink. In this section, I develop and demonstrate a reliable method for the triggering of peptide-based actuators through osmotic modification of their growth environment.

5.3.1 Osmotic triggering of microcrystal-based actuators

I investigated the possibility of actuator control through the use of osmotically-driven changes in solvent environment for FF within the droplets. Such variations have the potential to alter droplet diameter, thus triggering the criticality mentioned in the previous section, but also the potential to trigger nucleation by removal of acetic acid and water. It had previously been observed that the droplets were quite capable of triggering on their own- exposure to ambient air resulted in evaporation of the solvents, pushing the system to a point where nucleation was immediate. The crystals could then be seen to distort the water/oil interface as they grew, before finally the interface "snaps", allowing the crystal to straighten. The

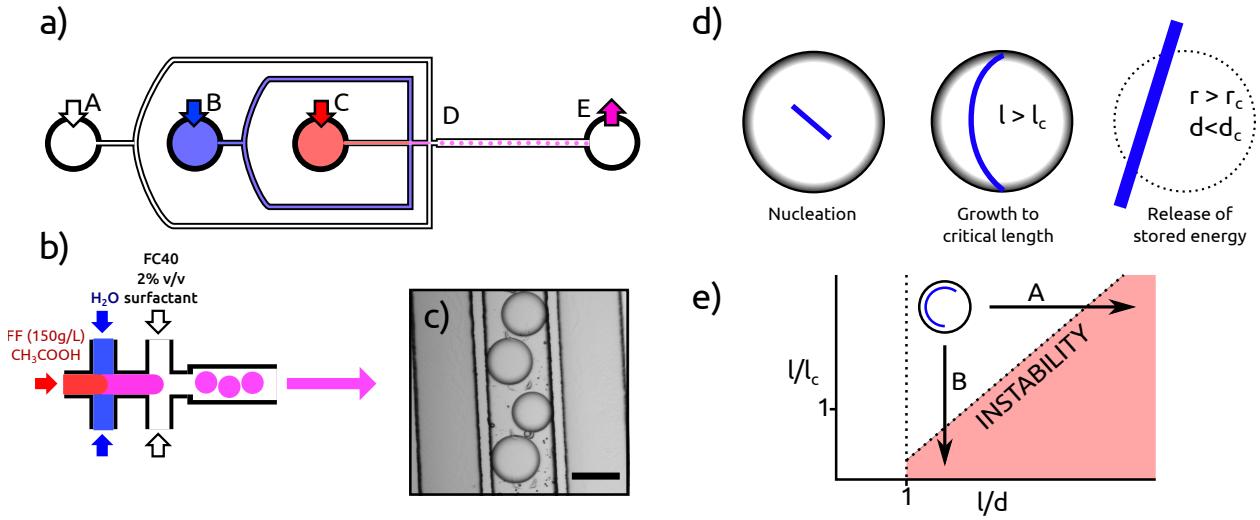

Figure 5.7: Experimental overview of this section. a) Schematic of a three-component droplet maker. A, B and C are inlets for the fluorocarbon continuous phase, water and a highly concentrated solution of FF in acetic acid. D is the mixing region where droplets are formed, and E the outlet where they are collected. b) Junctions of 3-component droplet maker. Flow rates are such that the two miscible phases have insufficient time to nucleate/fully mix before encapsulation, a technique with wide application. c) Droplets as captured in a device for controlled actuation. Scale bar 100μm d) Processes occurring within the droplets. The crystal nucleates and grows (length l) to the point where it undergoes Euler buckling ($l<l_c$). If the crystal undergoes radial growth (radius denoted by r), making its buckled form unstable, or the droplet diameter (d) shrinks, reducing the radius of curvature of the crystal below what the surface tension can force the crystal to adopt, the crystal unbuckles. Based on reference 90. e) Phase space diagram relating crystal/droplet geometry to system stability. A buckled crystal at the point depicted in phase space travels in direction A if the droplet shrinks, and B if it grows radially. Based on reference 90.

system still required a method of control, however. I discounted modulation of axial/radial growth rates out of hand as impractical in disperse droplet phases- those rates, and indeed the rates at which monomer would be "sunk" by other nucleation events are not readily controllable in a disperse phase.

I decided that osmosis would represent the closest approximation to the established evaporation mechanism- the droplets would lose solvent- ideally both water and acetic acid. This process would have three effects- firstly, it would decrease the radius of curvature of any FF crystals that may have been present- pathway B of figure 5.7e. Secondly, it would raise the concentration of FF within the droplet, triggering nucleation had it not occurred. Lastly, that higher concentration would enable the crystal to grow more rapidly in both directions, speeding the response time to the stimulus. The droplets produced by a device such as that in Figure 5.7a are relatively stable and can be either collected for later use and handled via pipette, or simply run into a second device.

The "second device" in this case would be one designed to withdraw solvent from the droplets, most critically acetic acid. Loss of water would simply enhance the solubility of the dipeptide (solubility 430 g/L in acetic acid, 0.76 g/L in water). As a result, I decided to use concentrated salt solutions- the low solubility of the salt in apolar media would limit its flow through whatever "membrane" was used, and the lower water activity would also mitigate possible flow of water into the droplets- while this would still likely trigger nucleation due to the extreme FF concentrations within the droplets, it would have implications for the droplet geometry. The first experiments made use of the continuous phase itself as a barrier. A device containing "cups" for the retention of droplets was prepared, and the output of the droplet maker was run into the inlet of the triggering device. Once sufficient droplets had been caught, the inlet was simply connected to a syringe containing a 15M solution of zinc bromide (Sigma-Aldrich).

Figure 5.8 shows the setup and typical result of this approach. The osmolyte flow was directed down the central channel, and any transport of acetic acid or water through the

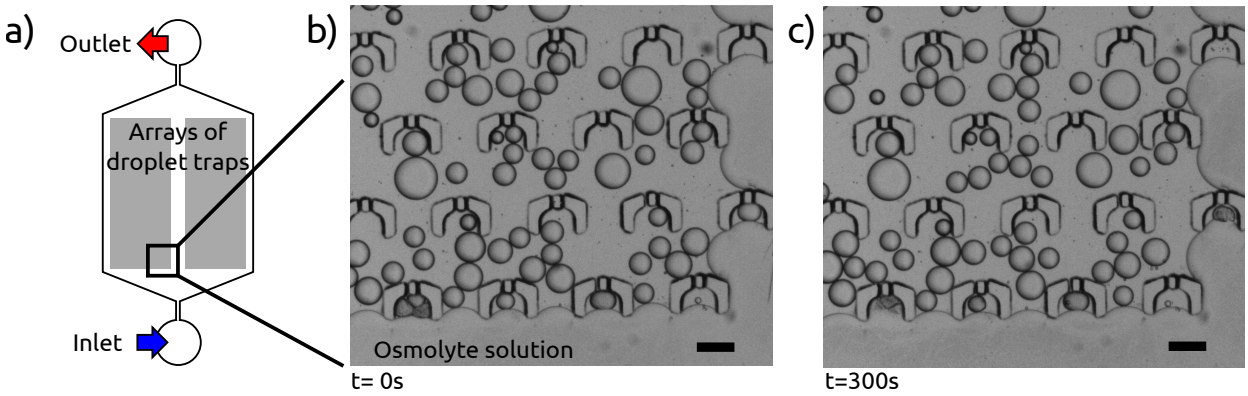

Figure 5.8: a) Schematic of a device used in the direct-contact test. Device width is 8mm, with two arrays of 100μm internal diameter "cups" either side of a narrow central channel. At the inlet, the device is loaded with droplets, and the inlet is then connected to a flow of osmolyte solution. b) Test region at start of timecourse. Droplets trapped inside cups by the osmolyte have already nucleated, visible as darkening. c) Test region at 300 seconds, with no change other than continued growth in the nucleated droplets and some evidence of droplets merging with the osmolyte stream. Scale bar 100 microns in both.

FC40 made possible by the surfactant would, in theory, manifest itself as a delay in actuation dependent on distance from the interface. However, it is apparent from the test that the method is not dependable- droplets only seem to nucleate where there is not only contact but pressure and direct flow past the surface, and this eventually leads to the surfactant and FC40 being stripped from the interface and the droplet merges with the bulk. The narrowness of the "membrane" and its liquid nature may also be a cause of a loss of selectivity- FF may be being lost from the droplets, and zinc bromide may be flowing in. Droplets in contact with the osmolyte but not within cups conspicuously fail to nucleate in figure 5.8. An unsuccessful attempt was made to use air as the "osmolyte" with the same setup. No actuation was observed over a 1200 second time course.

I concluded that some form of solid membrane was required, and having seen droplets shrinking while trapped within devices, I decided to use the elastomer for both the structure of the device and as an active component within it. PDMS is commonly thought to be more-or-less inert and impermeable- this is true for ionic solutes and for macromolecular biological

analytes [168], but over longer timescales, or in the presence of small molecule, hydrophobic solutes, PDMS is capable of absorption and desorption of uncharged small molecules to an extent that is capable of interfering with experiments [169, 170]. Critically, the permeability of PDMS to water vapour [171] leads to the shrinking of droplets stored in PDMS-walled chambers and to permeability induced flow [172]. This is partially controllable through the use of presaturation [172] but monolayers produced by silanes would be unlikely to show a significant effect on adsorption rates, other than to limit the contact area between a small, enclosed droplet of an aqueous phase and the channel wall, via the inhibition of wetting.

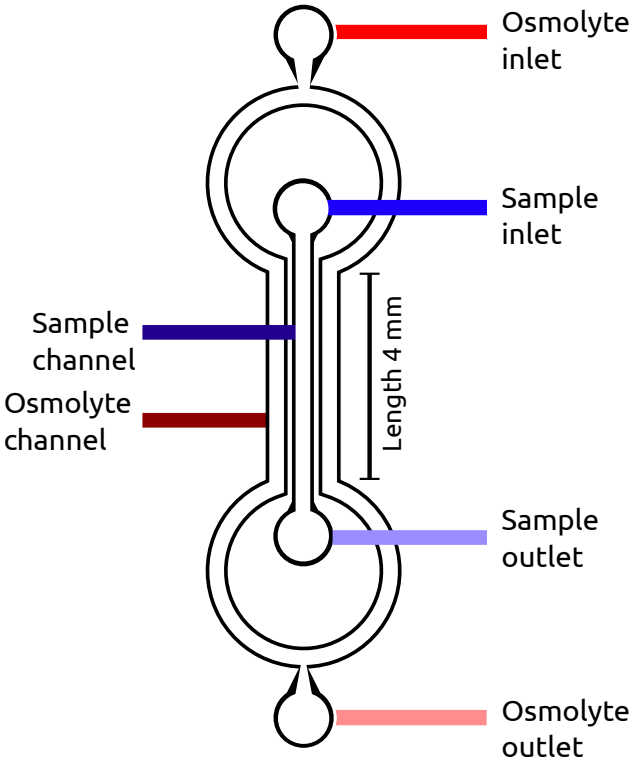

Figure 5.9: Diagram of the triggering device used. Channels are 100 microns wide and 50 microns high, separated by 20 micron walls. Prior to initiating the osmolyte flow, the walls are pre-saturated with a 50% v/v acetic acid solution in water.

As such, a device was designed that consisted of a narrow "capillary" channel that would hold the droplets to be triggered, separated by narrow PDMS walls from osmolyte channels carrying either a 50/50 water/acetic acid solution for storage of droplets or a concentrated salt solution to trigger the actuators. Sodium perchlorate, an inert, high solubility salt was chosen in preference to zinc bromide and sodium hydroxide, both of which (sodium hydroxide in particular) had proven to be corrosive to PDMS. Prior to the experiments, the channels had to be primed with the water/acetic acid solutions so as to avoid actuation due

to simple absorption by the walls. Use of a glass chip as a cover for the channel, embedded within the PDMS further limited the volume of PDMS into which the solvents could absorb. An important practical concern arises here due to the fact that the membranes-cum-walls, already having a high aspect ratio, must adhere to the underside of the glass without tearing off due to stress concentrations. A possible solution to this is to pre-treat the glass with allyl trimethoxysilane, which will leave it coated in allyl groups capable of reacting with the crosslinker used in Sylgard 184 (a silane), covalently bonding the glass chip to the walls. Pretreatment of the silicon wafer itself with the perfluorosilane solution mentioned elsewhere similarly renders the PDMS far less likely to stick to the wafer.

Figure 5.10: a) 15M sodium perchlorate solution in the external osmolyte channels is capable of triggering the actuators by withdrawal of solvent into the PDMS and osmolyte channel. b) A 50 % acetic acid solution in water fails to cause actuation when flowed in the osmolyte channel.

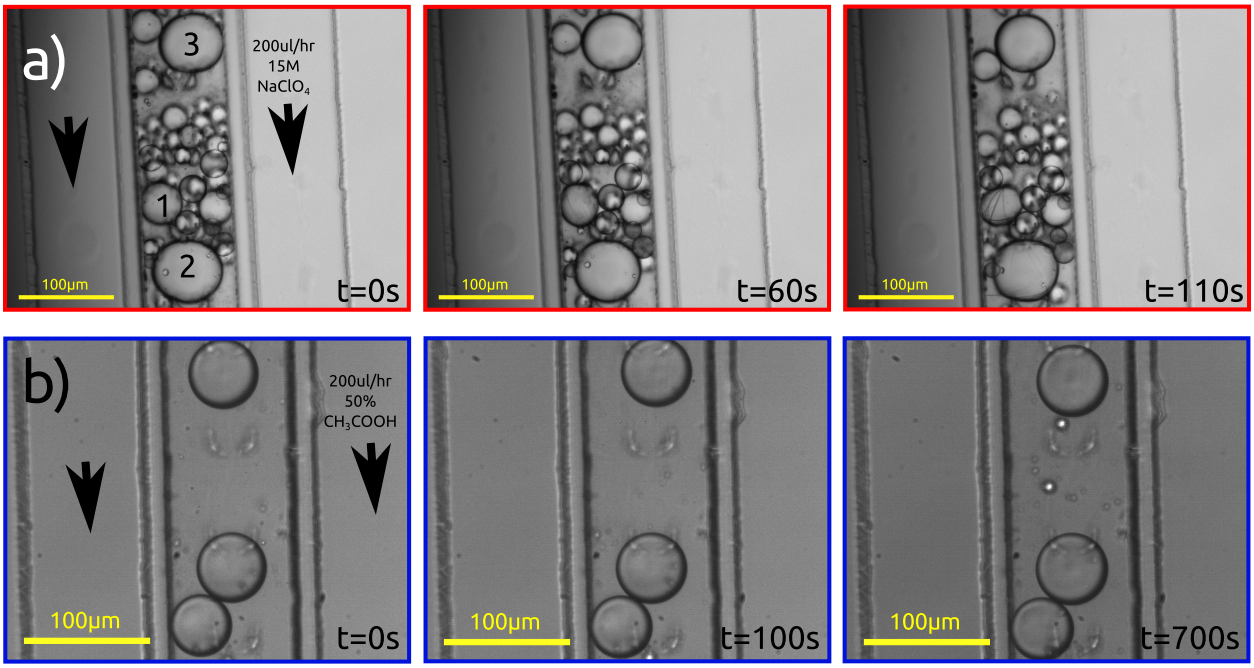

In Figure 5.10a) three droplets are labelled. Droplet 1 undergoes nucleation with spring-type actuation at 60 seconds, and droplet 2 after 110 seconds. In both cases, actuation is preceded by a loss of volume of around 4%, thought to be due to loss of acetic acid. Droplet 3 is an interesting case as during the test (1000 seconds total), no spring-type actuation is

observed. It is not in contact with the walls, either by contact or by indirect contact through another droplet. During a period of 200 seconds, it loses 17% of its volume. In 5.10b), the flowed solution is 50% acetic acid. This is a higher saturation than in the droplets, which are roughly 30% acetic acid by volume, the remainder being due to the volume of the FF in solution. All droplets increase in volume during the test, thought to be due to inflow of acetic acid from the presaturated walls of the device. The droplet not in contact with the active walls (the uppermost one) increases in volume by 11% over 300 seconds and stabilises at this volume. Those in contact, the lower two, increase in volume by 17% over the same period. The concentration of water remains higher in the osmolyte than in the droplets, but previous studies [168, 172, 169] suggest that permeability of water (and ionic salts) in PDMS is far lower than that of acetic acid, and so it is thought that the gradient of acetic acid is the major driving force for the growth or shrinkage of the droplets.

Before the tests in figure 5.10, the droplets were allowed to stand for 24 hours at room temperature, in the presence of the oil phase and surfactants and in sealed containers. No actuation was observed under any osmotic test conditions for newly-formed droplets. This curious observation can perhaps be associated with the possibility of chemical reaction or formation of solution structure within the droplets, and might explain the curious case of droplet 3 in figure 5.10a. Some slow (and therefore likely nucleation based) process must occur before the droplets can be triggered at all. This contrasts with the situation in air-drying droplets, where no such limitation is observed. The rates of loss of solvent are very different in air-drying and osmotically-actuated droplets, and the composition of the lost solvent is different, the air-dried droplets losing water as well as acetic acid in proportion to their vapour pressure. There is the possibility of alternate morphologies nucleating prior to the familiar FF crystals that provide the energy here, and those aggregates providing nucleation sites or rearranging on desolvation to form the familiar FF crystal.

5.3.2 PDMS as an active material

Throughout all the investigations detailed here, the microfluidic devices are composed of poly(dimethylsiloxane), PDMS, bonded to glass by use of oxygen plasma surface activation. Sylgard 184 (Dow Corning) is the specific formulation of the elastomer used, and it consists of allyl-functionalised polydimethylsiloxane chains which are crosslinked by a silane-terminated siloxane. When exposed to low-pressure plasma, PDMS displays a short-term hydrophilicity arising from the oxidation of surface groups [173], and can rearrange over the course of hours by mechanisms including reptation and inter-diffusion of chains [174], removing the oxidised species from the surface [175, 176]. The process of hydrophobic recovery can result in surface fouling from simple van der Waals interactions between proteins and the surface [177]. Further, the oil phase typically used in droplet makers fails to wet the surface of PDMS- a common failure mode of droplet makers then occurs, where the aqueous phase contacts the channel walls at the interface, resulting in a jetting breakup of the stream or simply a failure of the stream to form droplets.

The surface properties must therefore be altered, ideally in a way that permits the surface to be wetted by a perfluorocarbon/fluorosurfactant solution but not by the droplet stream. Previously, this was most frequently done with "Aquapel", a brand name for a substance having the appearances of being a saturated solution of a perfluoroalkyl trichlorosilane in petroleum ether. This volatile, water-reactive liquid would be injected into the channel and allowed to sit, before being flushed out by a stream of isopropanol or simply a jet of nitrogen. However, it is known that surface coatings on PDMS are labile, and frequently unstable with respect to rearrangement [174]. The extreme distortion of the channels which occurs on injection of petroleum ether is due to swelling of the elastomer- apolar species are readily absorbed by PDMS [168]- and this will result in rapid exchange at the surface, which is extensively distorted during the swelling and deswelling. The intended grafting is not likely to be the reason for the fluorophilic behaviour of the surface following the process, but rather fluorocarbon chains remigrating to the surface.

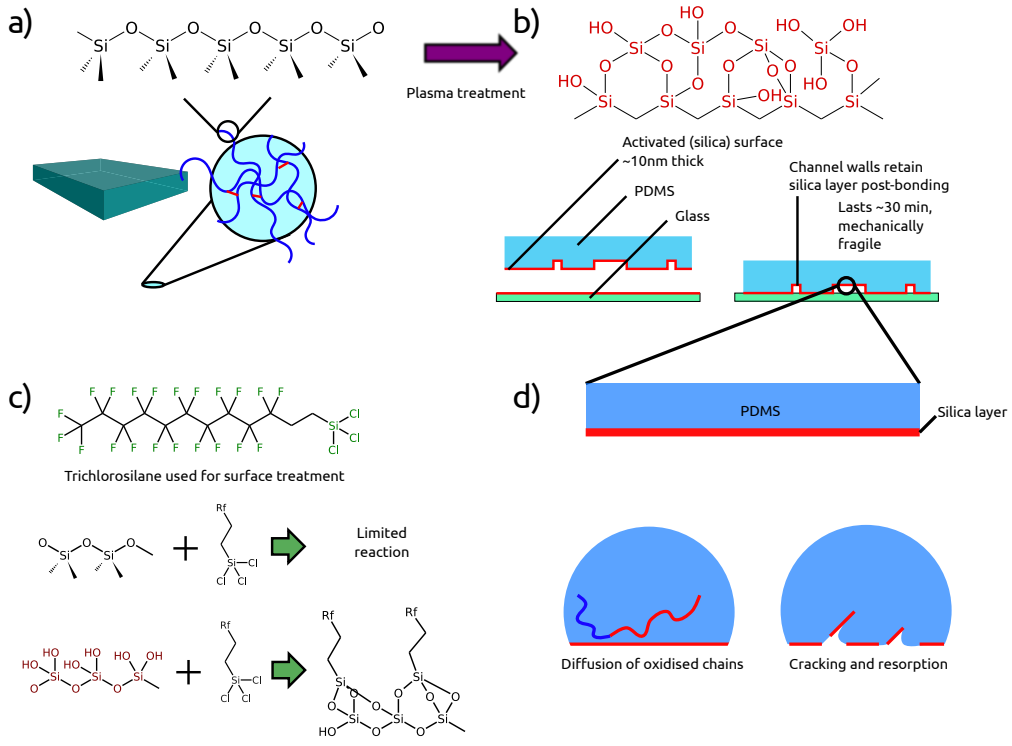

Figure 5.11: Overview of PDMS surface treatments. a) Untreated PDMS, a siloxane. Sylgard 184 consists of these chains (blue), which are terminated by allyl groups crosslinked by short silanes (red). It is a chemically inert material with low permeability to water. b) Plasma treatment oxidises the surface to yield a nanometres-thick silica layer [174]. This surface is fragile and is gradually resorbed. c) Surface treatment by silanes- only the activated surface is readily able to react with the trichlorosilane, yielding a perfluorocarbon layer and HCl. d) Mechanisms of PDMS surface degradation. Reptation and diffusion of chains away from the surface, and cracking and resorption of the silica layer. Both are strongly *promoted* by the use of petroleum ether solvents (e.g. Aquapel), while careful use of the method presented here will inhibit at least the resorption by rendering the silica layer non-wettable by PDMS.

A dependable method for perfluoroalkylation of PDMS surfaces therefore avoids the use of petroleum ether and similar solvents, and I sought to develop a reliable and reproducible way of carrying out the surface modification of the elastomer. A 0.25% v/v solution of (1,1,2,2-tetrahydro)perfluorododecyl trichlorosilane is prepared in FC-40, and the solution is introduced into the channels immediately following plasma activation and bonding to the glass slide. The solution is left for 10-15 minutes at 65 degrees, and prior to use the channels should be refilled with a solution of the surfactant. This scheme avoids many of the major issues with other protocols- by carrying out the functionalisation immediately after plasma exposure, the reaction takes place at a silica surface, rather than a methylated one [173]. By avoiding the use of solvents that swell PDMS, the intrachain diffusion and extensive distortion of the device (damaging the fragile silica layer) is suppressed, and the FC40 solution has no sensitivity to ambient moisture, nor does it attack polymer septa used to exclude moisture. Aquapel absorbs sufficient moisture over the course of days to become a suspension of fluorous polysilicates capable of obstructing microchannels.

5.3.3 Surfactant synthesis

Droplet microfluidics is a broad, and rapidly growing field. Of particular relevance to this work is the role of the droplet as an isolated microreactor, capable of being produced in great quantities amenable to statistical analysis by a relatively simple microfluidic device. Nucleation is the barrier that limits the rate of phase separation in supercritical systems, and division of a system into a great number of smaller, isolated systems enables this stochastic process to be studied [178] and allows for the easy elimination of spurious readings that may occur due to contamination by sequestering contaminants within discrete samples.

In chapter 3, it is shown that the phase transition in the BocFF system between the suspension and the extended fibrillar network is inhibited by shrinking the system size, and it has been demonstrated that in the nucleation and propagation of insulin aggregates, there is a direct relation between the droplet volume and the “lag time” to the formation of

aggregates with the characteristics of amyloid fibrils (ThT fluorescence and propagation by secondary nucleation) of the form $\tau = c_n V^{-1} + \tau_g$, for τ, τ_g the lag times in droplets and in bulk respectively, c_n a nucleation rate per unit volume and V the droplet volume [135].

Separation of a system into a controllably monodisperse emulsion enables the study of these rare events, and is a process readily achieved through microfluidic techniques. The encapsulation of FF/acetic acid/water ternary mixtures is achieved through a two-step process, occurring on a microfluidic chip on a millisecond timescale. The microfluidic device used employs a co-flow geometry, where the aqueous (disperse) and fluorocarbon (continuous) phases meet at a junction and subsequently flow together down a collection channel [179], with the aqueous phase separating into droplets due to the balance between its viscosity and the interfacial tension, in a "dripping" regime [180, 167].

The choice of solvents and continuous phases in PDMS-based microfluidics is critical, and does not permit the use of more familiar continuous phases. Simple hydrocarbons, for example, dissolve into PDMS and distort channels [168]. As a result, the continuous phase used in microfluidic droplet experiments is typically a fluorocarbon, typically Fluorinert FC-40, a brand name of the 3M company for C4, C5 perfluorotrialkylamines. This compound exhibits extremely low water solubility, and immiscibility with both aqueous and hydrocarbon phases. Furthermore, FC-40 wets neither PDMS nor glass, complicating its application in droplet microfluidics. The interface between the droplets and the continuous phase must be stabilised by a surfactant, though it is important to note that macroemulsions are intrinsically thermodynamically unstable due to their extended interface between bulk phases. The surfactant kinetically stabilises the emulsion by providing a barrier to coalescence [181] of the droplets, but a tendency of the surfactant to form microemulsions can result in "bridging" and hence the merging of droplets. A rule-of-thumb known as Bancroft's rule states that the phase in which the surfactant is more soluble will tend to form the continuous phase [182, 183, 184].

Taken together, these recommendations suggest the use of macrosurfactants with ex-

tended fluorocarbon "tails", capable of both creating relatively long-range steric barriers to coalescence in accordance with DLVO theory [185], and in order to enhance their solubility in the continuous phase. Highly fluorophilic surfactants based on fluoroalkyldimorpholinophosphates have been demonstrated to stabilise water-in-fluorocarbon emulsions [186, 187], but these are not proof against surface adsorption by aggregating biomolecules, in contrast to polyethylene glycol based surfactants [188]. The presence of surfactants in the aqueous phase runs a risk of perturbing aggregation processes, and in order to avoid effects due to changes in ionic strength, a non-ionic surfactant was necessary.

It was therefore decided to base the approach on the method of Holtze et. al. [189], with variations designed to improve reproducibility and to control more precisely the ratio of diblock to triblock surfactant molecules. The detailed synthesis is described in Materials and Methods, and the interfacial tension between the aqueous and fluorinated phases of droplets prepared as described is measured as 9.58 mN/m, approximated in the subsequent calculations as 10 mN/m.

7.25 grams Krytox 157FS(H) (Du Pont) (1.0 mmol), a perfluoropolyether of molecular weight 7250 (avg.) terminated by a carboxylic acid group is mixed with 4 ml Fluorinert FC-40 in a carefully-dried 25ml RBF, equipped with a magnetic stirrer, set up for short path vacuum distillation and the mixture thoroughly deoxygenated with a stream of dry nitrogen bubbled through the liquid. To this mixture, under a very slow flow of nitrogen, is added 300 microlitres of thionyl chloride through a septum and the temperature is brought to 60°C under vigorous stirring, and held at that temperature for four hours. Krytox 157FS(H) is a viscous and difficult-to-handle liquid and so the addition of FC-40 renders it amenable to stirring, though the remarkable capacity of both Krytox and FC-40 to dissolve gases requires both be rigorously deoxygenated. Thionyl chloride was chosen as the chlorinating agent as it produces no solid byproducts[1], but temperature control is necessary due to its volatility (b.p. 74°C) and tendency to decompose (noticeable as yellowing).

[1]Phosphorus pentachloride or oxychloride yield phosphoric acid, which forms a biphasic mixture and interferes in later reactions

The apparatus is then connected to a vacuum line and an efficient trap for acid gases, and the temperature maintained at 60°C for two hours, then gradually increased to 130°C over the course of 60 minutes, maintaining vigorous stirring. Unreacted thionyl chloride will condense in the receiver. The temperature is maintained until no haze or cloudiness is visible in the FC40-Krytox mixture. For added certainty, after the apparatus has cooled and the thionyl chloride removed, a flow of nitrogen should not pick up acid gases (SO_2 and HCl) when tested at the vent with UI paper.

The apparatus is allowed to cool to room temperature and brought back to very slight positive pressure with a gentle flow of nitrogen. A solution of Jeffamine ED600[2] (294mg, 0.49mmol) and diisopropylethylamine (258mg, 2.0mmol) in dry THF (10ml) is added dropwise over 10 minutes with vigorous stirring. A white precipitate forms. The mixture is stirred under slow nitrogen flow overnight. I observed that Jeffamine, indeed all PEG/PPG amines, are highly sensitive to heat and to oxygen. They seem to readily undergo chain scissions yielding foul-smelling short-chain amines, and will rapidly yellow in air. As a result, I find that heating is unwise, as well as unnecessary. Acid chlorides are highly reactive and the main barrier is the phase transfer- which naturally becomes easier as the reaction proceeds.

To form the diblock surfactant, the above protocol applies but rather than use Jeffamine ED600, which is bifunctional, the monofunctional Jeffamine M2000 (1960mg, 0.98mmol) was used.

The precipitate and THF are then washed into a 50ml falcon tube with the aid of 4ml FC-40 and the mixture centrifuged, separating the layers. The THF layer is drawn off and discarded, and replaced with a fresh layer. The mixture is agitated again, and the centrifugation repeated at higher speed. The supernatant is drawn off and the lower layer dried in vacuo. Yield is 90-95% of a pale yellow to clear viscous fluid.

[2]Jeffamine is a trademark of the Huntsman Corporation for a range of mono-, bi- and tri-functional amine-terminated copolymers of ethylene and propylene oxide

In operation, the diblock surfactant, which proved incapable of stabilising the output of a droplet maker on its own, was used as an additive to the triblock in proportion of up to 10% with good results. It is worth mentioning that simulations have suggested that the use of two surfactants with varying solution structure may be advantageous in preventing wetting of channel surfaces by the aqueous phase [190], quite aside from concerns about the surface presented by the surfactant to the internal environment.

5.3.4 Energy storage by elastic deformation

Many studies have appeared with the aim of establishing the mechanical properties of diphenylalanine and its derivatives through nanoindentation [9] via atomic force microscopy, through beam bending experiments [8], and by prediction from density functional theory [191]. Modified dipeptide nanostructures based on Boc-FF have been reported with point stiffness of 275 GPa [13]. The remarkable stiffness of diphenylalanine nanotubes is thought to depend to a great extent on the steric interactions of the bulky benzyl side chains [191], and the self-assembly of diphenylalanine-based scaffolds is partially determined by the tendency to adopt preferred orientations due to the quadrupole moment and resultant pi-stacking of the phenyl group [192, 193].

An FF crystal growing in a droplet will eventually contact the droplet walls through the axial growth process, and the properties of the walls and the crystal will then determine what follows. In the energy storage mode discussed in this subsection, the crystal undergoes elastic buckling. This is a process of deformation under a compressive load, where the applied stress causes a sudden, large deflection to a new, unstable equilibrium state. The Euler formula for buckling is given by the relation:

$$F_b = \frac{EI\pi^2}{l^2} \tag{5.1}$$

for Young's modulus E (20GPa [8]), second moment of area I and crystal length l. On contacting the droplet wall, it will be subject to a compressive force [90]:

$$F_c = 2\pi r\sigma \cos\theta \tag{5.2}$$

where it contacts the walls at a contact angle θ, and the surface tension of the interface is σ (10mN/m). This then gives rise to a critical length for buckling [90], and a balance of energies between the deformation of the crystal and of the interface determines whether or not the interface is pierced. It is shown in the reference that the requirement for buckling to occur is that the bending and interfacial energies are balanced as tube length increases- the crystal will simply exhibit a smaller and smaller radius of curvature until it reaches the curvature of the droplet. The critical length for buckling varies with the radius of the crystal as $r^{3/2}$ and with the diameter of the droplet as $d^{2/3}$. Interestingly, increase in length of a buckled crystal does not itself trigger the unbuckling (both surface energy and bending energy being linear in l) [90].

There is therefore a significant dependence of the "unbuckling" of the tubes- and the rapid release of the stored energy- on the radial growth rate of the filaments and droplet diameter. Both of these can be achieved through variation of initial conditions. Radial growth rate is a predictable function of the supersaturation, as demonstrated in chapter 2, and regimes of growth exist for the aqueous case at least where the radial growth rate is very low. Altering the initial composition of the mixture could result in variations in actuator stability, and indeed whether or not axial growth leads more to piercing or to buckling, but far more precise control can be exercised through the variation of droplet diameter and indeed droplet contents.

5.4 Conclusions

The investigation detailed in this chapter presents a new solvomorph of FF, displaying amyloid-like C(4) bond chains parallel to the long axis of the crystal. It displays similar

growth anisotropy arising from the axially-aligned peptide bonds and ionic interactions but a markedly different crystal structure to that as grown from water. Several other possible solvomorphs have been identified from those crystals grown in other alcohols, including a remarkable lamellar structure in isopropanol. The material properties of these crystals, in particular the large crystals that can be grown from methanol solutions, represent opportunities for further study and application. Further, I have quantified the solubilities of the diphenylalanine peptide in a wide range of solvents. Both the growth kinetics and morphologies of the resulting crystals can be modified through appropriate choice of the initial solvent of the FF as well as the lower solubility medium into which the solution is introduced to induce crystallization.

The crystal habit is determined by the alignment of the peptide linkage and the ionic termini, the crystal face normal to these interactions being high energy and accordingly prone to much faster growth than the parallel (radial) faces. The lamellar crystals formed in isopropanol may represent a system with multiple dipeptide environments in the unit cell.

Several useful alternatives have therefore been found to the most commonly used HFIP in the preparation of stock solutions. Acetic acid is easier to handle than HFIP, non-toxic and able to dissolve almost twice as much of the peptide. The kinetics of crystallization are significantly slowed in acetic acid, facilitating control of the process. We have fully characterised a novel solvomorph arising from the methanol-FF system, and have observed morphology changes with solvent conditions between a series of simple alcohol solvents. The findings in this chapter are highly relevant to studies and applications of the self-assembly of the FF dipeptide, including both the solubility behaviour of a wide range of solvent systems and detailed studies of the morphologies arising from certain alcohol-FF systems. Even between the simple alcohols studied in figure 5.1, striking variations in habit are observed. This work, therefore, introduces a new dimension to the space of parameters that can be varied in the preparation of nanostructures through diphenylalanine self-assembly.

An application of the FF-acetic acid system is then detailed in section 5.3. HFIP would be

unsuitable here due to its volatility and its ability to rapidly dissolve into PDMS, but the less volatile water/acetic acid/FF system is capable of being stored without special precaution, and then triggered to undergo nucleation of FF by osmotic withdrawal of solvent through the PDMS walls, here acting as membranes permeable to acetic acid and water, but not to the larger, polar dipeptide. The rate of energy release of the system is remarkably high (10 W/cc) [90], a power density significantly greater than that of actin polymerisation [194, 90]. This power density, coupled with the ease of preparation and biocompatibility of the components, demonstrates once again the incredible range of behaviours, properties and applications of the crystals formed by hydrophobic dipeptides.

Chapter 6

Conclusions and outlook

In conclusion, the FF dipeptide and its substituted derivatives form a fascinating family of self-assembling systems. The mechanical properties of the crystals and their intriguing morphology are likely to sustain interest in the system for a long time to come. The properties of any molecular aggregate are, of course, inextricably linked to its structure on the atomic level- the repeating pattern of molecules in space. In this thesis, I demonstrate that the repeating, three dimensional structure of aggregated FF leads directly to aggregation kinetics clearly distinct from those of amyloid fibril. The kinetics, even in the absence of diffractograms, demonstrate that the tubular aggregates are crystalline in nature. In the FF system, both radial and axial growth kinetics are now directly predictable from supersaturation alone, and this has allowed unprecedented insight into the processes occurring at the growth faces- leading to my conclusion that the aggregation of crystalline FF aggregates from solution is mechanistically quite distinct from that of long-chain polypeptides adding to an amyloid fibril. The most obvious difference is cooperativity- a polypeptide chain does not generally need to be radially stabilised as it adds to an axial face of its aggregate, while surface nucleation is a major step in the growth of FF aggregates from solution. Critically, this behaviour is seen on the axial and radial faces of the FF aggregate- the radial growth/thickening of amyloid

fibrils is not generally a continuous function of the excess concentration of monomer, but in FF the repeating units repeat in all directions, effectively indefinitely.

Experimental results in chapter 3 place FF, together with a number of other dipeptides, in a family of oligopeptides displaying a particular scaling behaviour of the free energy of aggregation. This scaling derives from the ratio between interactions scaling with volume, and interactions scaling with surface area. A relationship is established between the non-polar accessible surface area of the side chains and the free energy of aggregation, allowing extension of the scaling rule to the dipeptides. Kinetic measurements at a range of temperatures allow for the detailed analysis of the barrier to the elongation of FF crystals, which can then be compared with the barrier to elongation of full-length, unequivocally amyloid species. The values for the enthalpic barrier are strikingly similar between Aβ(1-42), with the free energy and entropy being somewhat variant. The FF elongation process (essentially, the deposition of a new layer of monomer in crystalline order on the axial face) is slightly less well compensated, but is still a thermally activated process. The nature of the barriers, however, are very disparate. Internal dynamics of the chain play a significant role in the rearrangement of the full chain in the elongation process, while the barrier derived for FF is a composite of a number of contributions corresponding to processes occurring at the face of the crystal. Addition-capable sites must be generated by the presence of monomer on the surface, and the concentration of these addition sites continues to be dependent on the supersaturation of FF. FF has little in the way of complicated internal dynamics and occurs in only two isolable states- the free monomer in solution, and the crystalline aggregate.

The case is different for the N-terminal substituted species BocFF, which displays a remarkable range of kinetic products- injection of the stock solution instantly yields a very stable suspension of spheres. These spheres undergo a ripening process but have not been observed to undergo phase transitions directly to the final product- a needle-like crystal. That step is mediated by nucleation of a new, "on-pathway" phase, an extremely shear-sensitive gel, followed shortly by the nucleation of crystals. This is a remarkable mirror of some well-characterised processes in amyloid aggregation- on/off-pathway aggregates, and

the concept of Ostwald's step rule applies there as here.

On the materials science front, this investigation has established the critical concentration of the dipeptide in a range of common solvents, and has underlined the importance of the alignment of the peptide bond within the unit cell, as can be seen from the novel solvomorph presented. The extremely anisotropic morphology of the aggregates of diphenylalanine, just as in amyloid fibril, is due to the relative alignment of the strong peptide hydrogen bond and the weak radial interactions generated from side chain hydrophobicity. This morphology, which is fairly robust even to some drastic changes in the solvent environment, gives rise to the second branch of studies of diphenylalanine, its application in materials science. The elongated crystals are notably strong and stiff, but they remain manipulable by the application relatively strong forces on the microscale, and I present two routes to reliably creating those forces.

Taken together, in the mechanism of diphenylalanine aggregation and the associated energy changes, there are some parallels to be drawn to amyloidogenic systems. FF fits onto a trendline that relates hydrophobic surface area and free energy of aggregation, and other short peptides, ones that form unequivocally fibrillar aggregates, also sit on this line. The extension of that line to the full-length species starts to become dubious, perhaps. A substituted diphenylalanine follows the Ostwald step rule in a manner familiar in protein aggregation, as far even as the early branching of the system into on- and off- pathway aggregates, interchanging only via the solvated monomer. It *demonstrates* these behaviours, just as FF demonstrates the famous "water-filled nanotube" paradigm, in its unit cell and often in its crystal. It is inescapable, though, that few of the mechanisms underpinning the processes inherent to amyloid aggregation and propagation are accurately *modelled* by the crystalline dipeptide. FF as a subject of study doubtless has more yet to give, but in my view, it will give far more to the materials scientist than the medical researcher.

Chapter 7

Materials and Methods

7.1 Thermodynamics of diphenylalanine self-assembly

7.1.1 Reagents and solutions

Solutions in water were prepared by the suspension of FF (Diphenylalanine, Bachem) in distilled water (18.2 Ω / m) followed by ultrasonication in a sonic bath until the suspension was homogeneous and heating to 100°C by means of a household kettle. Following 30 minutes at $\sim$ 100°C no visible aggregate was observable for concentrations up to and including 6 g / L (19.2 mM). Seed solutions for growth experiments were prepared by the sonication (via ultrasonic bath) at room temperature of 2 g/ l water solutions that had been allowed to aggregate and left standing for a day or more. FF was used as received without further purification, while the sample of GF as obtained required further purification. A solution of crude GF was prepared from GF (Nova, 692 mg) and 13 ml distilled water at 100°C. On cooling, GF precipitated as fine, needle-like crystals with a habit similar to FF (yield 312

mg). These crystals were removed from the mother liquor by vacuum filtration and washed on the filter with 2 ml cold distilled water.

7.1.2 UV spectrophotometry

UV spectrophotometry was conducted using a Cary 400 spectrophotometer, instrument version 8.01. Spectra were recorded between 300 and 230 nanometres with a reading every 0.4 nm. Spectral bandwidth was 2 nm. The spectrophotometer was fitted with a variable temperature stage (Peltier thermocouple system). Glass cuvettes of path length 2 mm or 4mm were used depending on the volume of solution available for the test. Concentration was taken to be proportional to the peak height of the maximum closest to the 257.6 nm absorption. A calibration curve was obtained. Solutions of FF in distilled water was prepared in accordance with the above method at supercritical concentrations of 1.50, 1.40, 1.30 and 1.20 g / L. The solutions were prepared separately and not by dilution of the 1.50 g / L stock. Spectra were recorded and the intensity of absorption (above 300 nm zero) at 257.6 nm was plotted against concentration. A linear least squares best fit was plotted through the origin. The change in peak absorbance with temperature was found by heating a solution of 0.5 g / L concentration from 4 to 70 $^{\circ}C$ and this was used to correct readings at each temperature. To investigate potential subcritical association in water and hence the validity of the crystallisation model (which assumes no long-lived association below the critical concentration, and nucleation-dependent association thereafter), solutions at concentrations 0.10 to 1.00 g / l (3 at each concentration, final value an average) were prepared by dilution of 1.00 g / l stock. These were allowed to stand for one hour, and then ultracentrifuged for one hour under 620000 g. The absorption above a zero (300 nm) at 257.6 nm was plotted against concentration. To ascertain critical concentrations (solubility) as a function of temperature, quantities of diphenylalanine at a range of concentrations were prepared and allowed to equilibrate slowly in quiescent conditions to room temperature and then held at 4°C overnight in the presence of a number of macroscopic crystals. The temperature controlled stage of the spectrophotometer was set to the starting temperature (either 4 or

8 °C) and the program "Wavelength Scans at Temperature Increments", from the Agilent website was used to record a series of spectra between 230 and 300 nm following stirring for 80 minutes at a number of temperatures between 8 and 68°C.

7.2 Boc-FF: Structural Transitions and Ostwald's Step Rule

7.2.1 UV-Vis spectrophotometry

10 ml aliquots of a suspension of Boc-FF were prepared as described above and allowed to stand in a syringe. At 2 min intervals, the suspension was gently agitated and 1.5 ml was pushed through a 0.22μm syringe filter (Millex Ultrapore, PVDF membrane). The concentration of Boc-FF in these aliquots was determined from the difference in specific absorbance at 257.6 nm and a baseline at 300 nm using Cary-Varian 400 spectrophotometer running WinUV software. The spectral bandwidth was 1.0 nm.

7.2.2 Microfluidics

The microfluidic measurements of the growth kinetics of the FF crystals were performed as described below, except that here the measurements were performed at different temperatures. Temperature was controlled using a heated microscope stage (Turner TC series).

Measurements of lengths of growing microcrystals were made every 5 s using time delay photography, using a Zeiss Axio Observer A1 microscope (Carl Zeiss, Jena, Germany) and a CoolSNAP-MYO camera (Photometrics, Tucson, AZ, USA). The axial growth rates at

each value of the supersaturation were computed as the mean of the five fastest growing structures (see chapter 2). We measured the axial growth rates at different temperatures, using the data on the temperature dependence of the critical concentration to correct for the fact that the driving force for aggregate growth decreases at higher temperatures.

7.2.3 Phase Behavior

N-(tert-butoxycarbonyl)-L-Phe-L-Phe-COOH (Boc-FF, Bachem) stock solutions were prepared in absolute ethanol and then diluted in the required ratios in double distilled water, forming an array of peptide concentrations and solvent compositions. The structural morphologies of the resulting species were then determined by bright field microscopy and SEM observations. In all following experiments, Boc-FF stock solution in ethanol was diluted to form 10% (v/v) ethanol in water solution, and phase behavior was monitored by the following methods.

7.2.4 Isolation of Separate Phases

Suspensions of Boc-FF spheres were prepared by mixing of 1 part in 10 by volume stock solution of its monomers into ddH_2O followed by gentle mixing. The crystalline phase was isolated by the agitation of this suspension for 15 minutes or by allowing this solution to stand for one hour. The fibrillar phase was isolated by centrifugation of suspensions of spheres at 4°C and the separation of the supernatant. The supernatant was stored at 4°C for 15-20 minutes and was then flash frozen with liquid nitrogen and dried under reduced pressure.

7.2.5 Dynamic Light Scattering (DLS)

1 ml suspension of Boc-FF were prepared as described above, and 100μl aliquots were introduced into a low volume DLS cell. The refractive index was estimated to be 1.450 and the absorbance to be 0.001. The dispersant viscosity was taken to be 1.538 cP, and the dispersant refractive index as 1.339. Size measurements were made at 20°C using a Malvern Zetasizer Nano ZSP (Malvern Instruments, Malvern, UK). ζ-potential measurements were performed in a Malvern disposable folded capillary cell with the same parameters as above, and the additional specification of a dispersant dielectric constant at ϵ_r=69.4. Measurements were averaged over the first five minutes after sample preparation.

7.2.6 Microdroplet Formation

Microfluidic channels were fabricated in polydimethylsiloxane (PDMS; Dow Corning), using SU8 on silicon masters and standard soft lithography techniques, and then plasma bonded to glass slides to create sealed devices. Boc-FF stock solutions in ethanol were mixed on chip to form a solution of 10% (v/v) ethanol in water, and microdroplets were formed in an oil phase of Fluorinert FC-40 (SigmaAldrich, Gillingham, UK), and 2.0% (ww) block-copolymer surfactant. Syringe pumps (Cetoni GmbH, Korbussen, Germany) were used to control the flow of fluids, and the microdroplets were immediately inserted into rectangular glass capillaries (CM Scientific, Silsden, UK) sealed and then observed under bright field microscopy as a function of time.

7.2.7 High Resolution Scanning Electron Microscopy (HR-SEM)

Samples of Boc-FF solutions at 1:10 ethanol:water ratios at various time points after the initiation of self-assembly were placed on glass slides and were left to dry at room temper-

ature. Samples were then coated with Cr and viewed using a JSM-6700 field-emission SEM (Jeol, Tokyo, Japan), equipped with a cold field emission gun (CFEG), operating at 1 kV.

7.2.8 Nuclear Magnetic Resonance (NMR) Spectroscopy

NMR data were acquired using a BRUKER Avance 700 Ultrashield spectrometer equipped with TXI Cryoprobe. Samples of the Boc-FF peptide were dissolved in 100% EtOD and then diluted to form 10% (v/v) ethanol in H_2O solutions. 1D ^1H spectra were rapidly acquired at 25°C using 180 water-selective pulses to suppress resonances from H_2O. NMR data were processed and analysed using TOPSPIN.

7.2.9 X-ray Powder Diffraction

Samples of the spheres, gels and tubes were prepared as above and mechanically ground into fine powders. The resulting samples were placed in a flat glass sample holder and XRPD data was collected on a laboratory Philips X'Pert Pro diffractometer using Bragg-Brentano geometry operating at 40 kV and 40 mA using Cu-Kα radiation ($\lambda = 1.5418$ Å).

7.3 Kinetics of the self-assembly process

7.3.1 Microfluidics

The flow reactors used in this study were microfluidic devices constructed from polydimethylsiloxane (PDMS), according to standard protocols of soft lithography [74, 75]. In brief, a

25μm thick layer of SU-8 3025 photoresist was spin-coated onto a silicon wafer, exposed to UV-light through a mask in which the device design was printed, then manufactured in 1-methoxy-2-propyl acetate (PGMEA). The microfluidic device was fabricated from Sylgard 184 PDMS elastomer (DowCorning, Midland, MI, USA), using 1h curing at 65°C. After cutting the device, punching the holes for inlets and outlets, and activation via plasma treatment with a Femto plasma bonder (Diener Electronic, Ebhausen, Germany), the microfluidic device was bonded to a 3x1 inch microscope slide.

7.3.2 Protocol

A suspension of seed crystals was passed through the device, and once sufficient crystals had settled in the central chamber, a flow of solution of known concentration was initiated at a rate of 800 μl/hr, corresponding to velocities on the order of millimetres per second in the channel centre, by means of a NemeSys syringe pump (Cetoni, Korbussen, Germany). The experiment was halted either at the predetermined time or if nucleation was observed in the supersaturated solution.

Measurements of lengths of growing microcrystals were made every 5s using time delay photography, using a Zeiss Axio Observer A1 microscope (Carl Zeiss, Jena, Germany) and a CoolSNAP-MYO camera (Photometrics, Tucson, AZ, USA). For the experimental long timescales used in the low supersaturation experiments, images were taken every 5 min for periods up to 1000 min. To ensure sufficient sample population of growing crystals, suspensions of seed crystals were injected into the channel and the supernatant drawn off leaving large numbers of settled crystals. The results were recorded after a delay of 60 minutes after commencing flow, in order to limit the influence of the resolvation of small aggregates.

The axial and radial growth rates at each value of the supersaturation were computed as the mean of the five fastest growing structures. We included only the five fastest growing crystals in order to ensure that the reaction was not inhibited by random effects arising from positioning, surface contact or contamination, which would be expected to slow down the

growth kinetics. This strategy was prompted by the observation that even at the highest values of σ, some crystals displayed no measurable growth. The kinetic data (growth rate as a function of σ) were fitted to the exponential model derived by Nielsen [71] for 2D-nucleation dominated crystal growth. This analysis has the caveat that there is possibly an additional contribution from a dislocation mechanism, that will be more important at low σ values, but is generally likely to be very small [71].

7.3.3 Solutions and seed crystals

Solutions in water were prepared by the suspension of FF (diphenylalanine, Bachem, Bubendorf, Switzerland) in distilled water (18.2 MΩ/m) followed by ultrasonication in a sonic bath until the suspension was homogeneous, and then heating to 100°C. Following incubation for 30 min at this temperature, no visible aggregates were observable for concentrations up to and including 6 g/L (19.2 mM); these solutions were then diluted to the desired concentrations for the growth experiments. To confirm the concentrations, the absorbance at 258 nm at room temperature was taken to be proportional to concentration (absorption coefficient of FF at 258 nm is 390 $cm^{-1}M^{-1}$). These measurements were made using a Cary 400 spectrophotometer, instrument version 8.01. Spectra were recorded between 300 and 230 nm with a reading every 0.4 nm with a spectral bandwidth of 2 nm, using glass cuvettes with 10mm path lengths. Concentrations were taken to be proportional to the peak height of the absorption maximum closest to 258 nm.

Pre-formed seed fibrils were prepared for growth experiments by cooling-induced precipitation of 2 g/L FF from dd H_2O. The resultant suspensions were kept cool and sonicated (Sonorex, 50% power, 50% duty cycle, 2 min, Bandelin, Berlin, Germany) prior injection into the channels by micropipette through the outlet port of the microfluidic device. Suspensions of microcrystals, with a relatively narrow starting size distribution, for the experiments in which the aspect ratios were modified were prepared by sonication of 1 ml of an aggregated suspension at 2g/L total FF concentration without external cooling (Bandelin Sonorex, 50% power, 50% duty cycle, 2 min).

7.4 Applications in materials science- the effect of solvent environment on self-assembly

7.4.1 Solubility

Solubility was established spectroscopically, using both a standard solution to establish the extinction coefficient in the solvent and then a saturated solution prepared by addition of a relatively large quantity of diphenylalanine a sample of the solvent. The samples were centrifuged and the supernatant drawn off for analysis. Concentration was taken to be proportional to the difference in absorbance at the peak closest to 257.6 nm and the baseline at 300 nm. The instrument used was a Cary-Varian 400 running WinUV software. The spectral bandwidth was 1.0 nm. Five separate samples were taken for each solvent.

For low solubility solvents, experimental error in calibration was deemed greater than the error introduced by varying extinction coefficients. The extinction coefficient was approximated as that of 1-decanol.

For solvents strongly absorbing in the 230-280 nm range (acetone, phenol, ethyl acetate, formamide), and solvents for which the solubility was too high to give reliable spectrophotometric results solutions were made as above and samples were placed on microscope slides and weighed. The samples so prepared (other than those in volatile HFIP, TFE and acetone) were heated at 100°C until dry and the residue weighed.

For solvents that are solid at room temperature (phenol, tert-butanol) the reported solubility is that 5 degrees above their melting point. (46°C for phenol, 30°C for t-butanol).

7.4.2 Thin layer chromatography

Glass backed plates with 250μm unmodified silica matrix layer (Sigma) were used without modification. The retention factor in absolute ethanol was obtained for diphenylalanine (Bachem), phenylalanine (Sigma) and acetic acid. Two solutions of diphenylalanine in acetic acid were prepared, one being allowed to stand at room temperature for two days and one being prepared immediately prior to the test. A solution of phenylalanine was also prepared in acetic acid directly before the test. Spots were visualised by exposure to iodine vapour.

Diphenylalanine shows a somewhat higher retardation factor than does phenylalanine alone; in ethanol the R_f of FF is 0.61, compared to 0.49 for the more polar monopeptide. No spot at 0.49 was visible in either the FF solution that had been newly prepared or that which had been allowed to stand for two hours.

7.4.3 Microfluidic devices

The flow reactors were microfluidic devices constructed from poly(dimethylsiloxane) bonded to a microscope slide [74, 75]. Immediately following plasma activation of the surface (Diener Femto, 40% power, exposure time 10 s), a solution of a trichlorosilane in Fluorinert FC40 was introduced to the channels and the devices incubated at 65° C for 10 minutes, as described in the text.

Where glass chips were used to prevent excessive loss into the bulk PDMS, the glass chips were cleaned by means of sonication in isopropanol, then randomly fractured with the first weapon to hand, yielding a heterogeneous distribution of fragments. These fragments were suspended in a 0.25% solution of allyl trimethoxysilane (Sigma-Aldrich) in refluxing chloroform for 15 minutes before being collected on a filter paper and washed with isopropanol and

dried. Chips closely matching the dimensions of the channels were then inserted into the degassed PDMS and carefully placed on top of the device channels, and the PDMS cured.

Surface treatment of silicon wafers carrying the positive image of the channels is carried out by first cleaning the wafer (sonication in isopropanol), followed by plasma activation of the surface. The trichlorosilane/FC40 solution is then applied to the wafer. The wafer is then heated to 65°C for 15 minutes and dried in a nitrogen stream.

7.4.4 Microdroplet encapsulation of solutions

A 300mg/ml solution of diphenylalanine (Bachem) in acetic acid (Sigma-Aldrich) was prepared and mixed with ddH_2O in a droplet making device. Immediately following mixing on chip, the flow of acetic acid-FF-water was separated into droplets by a flow of Fluorinert FC40 containing 2% v/v of a triblock surfactant prepared as in the text.

7.4.5 Osmotic actuation of FF-containing microdroplets

The droplets produced were incubated at room temperature for 24 hours, and loaded into PDMS microchannels, separated from a flow of osmolyte by walls measuring 20μm in width by 50μm height. Prior to the loading of the droplets, flow of the non-actuating osmolyte in the outer channels was established and allowed to equilibrate for five minutes. Images were taken by timelapse optical microscopy at intervals of 5 or 10 seconds over experimental runs up to 1000 seconds.

Osmolyte solutions were prepared by the solution of sodium perchlorate (Sigma Aldrich) in water to a final concentration of 1836 g/L (15 molar). Non-actuating osmolyte solutions were prepared by mixing acetic acid and water in a 1:1 volume ratio.

Chapter 8

Bibliography

Bibliography

[1] Görbitz, C. H. *Chemistry* **2001,** *7,* 5153–5159.

[2] Reches, M.; Gazit, E. *Science* **2003,** *300,* 625–627.

[3] Görbitz, C. H. *Chem. Commun. (Camb.)* **2006,** 2332–2334.

[4] Gazit, E. *FASEB J.* **2002,** *16,* 77–83.

[5] Carny, O.; Shalev, D. E.; Gazit, E. *Nano Lett.* **2006,** *6,* 1594–1597.

[6] Bdikin, I.; Bystrov, V.; Kopyl, S.; Lopes, R. P. G.; Delgadillo, I.; Gracio, J.; Mishina, E.; Sigov, A.; Kholkin, A. L. *Appl. Phys. Lett.* **2012,** *100,* 43702–43702–4.

[7] Kholkin, A.; Amdursky, N.; Bdikin, I.; Gazit, E.; Rosenman, G. *ACS Nano* **2010,** *4,* 610–614.

[8] Niu, L.; Chen, X.; Allen, S.; Tendler, S. J. B. *Langmuir* **2007,** *23,* 7443–7446.

[9] Kol, N.; Adler-Abramovich, L.; Barlam, D.; Z., S. R.; E., G.; Rousso, I. *Nano Lett.* **2005,** *5,* 1343–1346.

[10] Adler-Abramovich, L.; Reches, M.; Sedman, V. L.; Allen, S.; Tendler, S. J. B.; Gazit, E. *Langmuir* **2006,** *22,* 1313–1320.

[11] Görbitz, C. H. *Chemistry* **2007,** *13,* 1022–1031.

[12] Knowles, T. P. J.; Fitzpatrick, A. W.; Meehan, S.; Mott, H. R.; Vendruscolo, M.; Dobson, C. M.; Welland, M. E. *Science* **2007,** *318,* 1900–1903.

[13] Adler-Abramovich, L.; Kol, N.; Yanai, I.; Barlam, D.; Shneck, R. Z.; Gazit, E.; Rousso, I. *Angew. Chem., Int. Ed. Engl.* **2010,** *49,* 9939–9942.

[14] Gour, N.; Barman, A. K.; Verma, S. *J. Pept. Sci.* **2012,** *18,* 405–412.

[15] Wang, M.; Du, L.; Wu, X.; Xiong, S.; Chu, P. K. *ACS Nano* **2011,** *5,* 4448–4454.

[16] Kauzmann, W. *Adv. Prot. Chem.* **1959,** *14,* 1–63.

[17] Tanford, C. *The Hydrophobic Effect: Formation of Micelles and Biological Membranes;* Wiley Interscience Publications: 1979.

[18] Hanwell, M. D.; Curtis, D. E.; Lonie, D. C.; Vandermeersch, T.; Zurek, E.; Hutchison, G. R. *J. Cheminf.* **2012,** *4,* 1–17.

[19] Muller, N. *J. Solution Chem.* **1988,** *17,* 661–672.

[20] Graziano, G.; Lee, B. *J. Phys. Chem. B* **2005,** *109,* 8103–8107.

[21] Dill, K. A. *Biochemistry* **1990,** *29,* 7133–7155.

[22] Frank, H. S.; Evans, M. W. *J. Chem. Phys* **1945,** *13,* 507.

[23] Blokzijl, B. W.; Engberts, J. B. F. N. *Angew. Chem., Int. Ed. Engl.* **1993,** *32,* 1545–1579.

[24] Liu, L.; Yang, C.; Guo, Q. *Biophys. Chem.* **2000,** *84,* 239–251.

[25] Ben Naim, A. *Hydrophobic Interactions;* Plenum Press: 1980.

[26] Abraham, H. *J. Chem. Soc., Faraday Trans.* **1984,** *80,* 153–181.

[27] Chandler, D. *Nature* **2005,** *437,* 640–647.

[28] Stillinger, F. H. *J. Solution Chem.* **1973,** *2,* 141–158.

[29] Helfand, E.; Reiss, H.; Frisch, H. L.; Lebowitz, J. L. *J. Chem. Phys.* **1960,** *33,* 1379.

[30] Reiss, H.; Frisch, H. L.; Lebowitz, J. L. *The Journal of Chemical Physics* **1959,** *31,* 369.

[31] Perutz, M. F.; Finch, J. T.; Berriman, J.; Lesk, A. *PNAS* **2002,** *99,* 5591–5595.

[32] Balbirnie, M.; Grothe, R.; Eisenberg, D. S. *PNAS* **2001,** *98,* 2375–80.

[33] Kuwajima, K.; Hiraoka, Y.; Ikeguchi, M.; Sugai, S. *Biochemistry* **1985,** *24,* 874–881.

[34] Kuwajima, K. *Proteins* **1989,** *6,* 87–103.

[35] Dill, K. A. *Biochemistry* **1985,** *24,* 1501–1509.

[36] Agashe, V. R.; Shastry, M. C. R.; Udgaonkar, J. B. *Nature* **1995,** *377,* 754–756.

[37] Richards, F. M. *J. Mol. Biol.* **1974,** *82,* 1–14.

[38] Suzuki, S.; Green, P. G.; Bumgarner, R. E.; Dasgupta, S.; Goddard III, W. A.; Blake, G. A. *Science* **1992,** *257,* 942–945.

[39] Stone, A. J. *The Theory of Intermolecular Forces;* Clarendon Press: 1997.

[40] Bohon, R. L.; Claussen, W. F. *J. Am. Chem. Soc.* **1951,** *73,* 1571–1578.

[41] Graziano, G. *Biophys. Chem.* **2004,** *110,* 249–58.

[42] Gibbs, J. W. *Trans. Conn. Acad. Arts Sci.* **1878,** *3,* 343–524.

[43] Wulff, G. *Zeitschrift für Kryst. und Mineral.* **1901,** *34,* 449–530.

[44] von Laue, M. *Z. Kristallogr.* **1943,** *105,* 124.

[45] Strickland-Constable, R. F. *Kinetics and Mechanism of Crystallization;* Academic Press Inc. (London): 1968.

[46] Hartman, P.; Perdok, W. G. *Acta Cryst.* **1955,** *8,* 49–52.

[47] Hartman, P.; Perdok, W. G. *Acta Cryst.* **1955,** *8,* 525.

[48] Glenner, G. G.; Wong, C. W. *Biochem. Biophys. Res. Commun.* **1984,** *120,* 885–890.

[49] Klimov, D. K.; Thirumalai, D.; Park, C. *Structure* **2003,** *11,* 295–307.

[50] Tjernberg, L.; Hosia, W.; Bark, N.; Thyberg, J.; Johansson, J. *J. Biol. Chem.* **2002,** *277,* 43243–6.

[51] Gazit, E. *FEBS J.* **2005,** *272,* 5971–5978.

[52] Pawar, A. P.; Dubay, K. F.; Zurdo, J.; Chiti, F.; Vendruscolo, M.; Dobson, C. M. *J. Mol. Biol.* **2005,** *350,* 379–392.

[53] Aida, T.; Meijer, E. W.; Stupp, S. I. *Science* **2012,** *335,* 813–817.

[54] Tysseling-Mattiace, V. M.; Sahni, V.; Niece, K. L.; Birch, D.; Czeisler, C.; Fehlings, M. G.; Stupp, S. I.; Kessler, J. A. *J. Neurosci.* **2008,** *28,* 3814–3823.

[55] Marshall, K. E.; Hicks, M. R.; Williams, T. L.; Hoffmann, S. r. V. n.; Rodger, A.; Dafforn, T. R.; Serpell, L. C. *Biophys. J.* **2010,** *98,* 330–338.

[56] Mason, T. O.; Chirgadze, D. Y.; Levin, A.; Adler-Abramovich, L.; Gazit, E.; Knowles, T. P. J.; Buell, A. K. *ACS Nano* **2014,** *8,* 1243–53.

[57] Li, Q.; Jia, Y.; Dai, L.; Yang, Y.; Li, J. *ACS Nano* **2015,** *9,* 2689–2695.

[58] Lekprasert, B.; Sedman, V.; Roberts, C. J.; Tendler, S. J. B.; Notingher, I. *Opt. Lett.* **2010,** *35,* 4193–4195.

[59] Lekprasert, B.; Korolkov, V.; Falamas, A.; Chis, V.; Roberts, C. J.; Tendler, S. J. B.; Notingher, I. *Biomacromolecules* **2012,** *13,* 2181–2187.

[60] Azriel, R.; Gazit, E. *J. Biol. Chem.* **2001,** *276,* 34156–34161.

[61] Tenidis, K.; Waldner, M.; Fischle, W.; Bergmann, M.; Weber, M.; Merkle, M.-l.; Voelter, W.; Brunner, H. *J. Mol. Biol.* **2000,** *295,* 1055–1071.

[62] Jarrett, J. T.; Lansbury, P. T. *Cell* **1993,** *73,* 1055–1058.

[63] Baldwin, A. J.; Knowles, T. P. J.; Tartaglia, G. G.; Fitzpatrick, A. W.; Devlin, G. L.; Shammas, S. L.; Waudby, C. A.; Mossuto, M. F.; Meehan, S.; Gras, S. L.; Christodoulou, J.; Anthony-Cahill, S. J.; Barker, P. D.; Vendruscolo, M.; Dobson, C. M. *J. Am. Chem. Soc.* **2011,** *133,* 1–9.

[64] Meisl, G.; Yang, X.; Hellstrand, E.; Frohm, B.; Kirkegaard, J. B.; Cohen, S. I. a.; Dobson, C. M.; Linse, S.; Knowles, T. P. J. *Proceedings of the National Academy of Sciences of the United States of America* **2014,** *111,* 9384–9.

[65] Šarić, A.; Buell, A. K.; Meisl, G.; Michaels, T. C. T.; Dobson, C. M.; Linse, S.; Knowles, T. P. J.; Frenkel, D. *Nat. Phys.* **2016,** *12,* 874–882.

[66] Yan, X.; Zhu, P.; Li, J. *Chem. Soc. Rev.* **2010,** *39,* 1877–1890.

[67] Reches, M.; Gazit, E. *J. Nanosci. Nanotechnol.* **2007,** *7,* 2239–2245.

[68] Yemini, M.; Reches, M.; Gazit, E.; Rishpon, J. *Anal. Chem.* **2005,** *77,* 5155–5159.

[69] Yan, X.; Su, Y.; Li, J.; Früh, J.; Möhwald, H. *Angew. Chem., Int. Ed. Engl.* **2011,** *50,* 11186–11191.

[70] Burton, W. K.; Cabrera, N.; Frank, F. C. *Phil. Trans. R. Soc. Lond.* **1951,** *243,* 299–358.

[71] Nielsen, A. E. *J. Cryst. Growth* **1984,** *67,* 289–310.

[72] Andersen, K.; Castillo-Leon, J.; Hedstrom, M.; Svendsen, W. E. *Nanoscale* **2011,** *3,* 994–998.

[73] Song, Y.; Challa, S. R.; Medforth, C. J.; Qiu, Y.; Watt, R. K.; Miller, J. E.; van Swol, F.; Shelnutt, J. A.; Lafayette, W.; March, A. *Chem. Commun. (Cambridge, U. K.)* **2004,** 1044–1045.

[74] Duffy, D. C.; McDonald, J. C.; Schueller, O. J.; Whitesides, G. M. *Anal. Chem.* **1998,** *70,* 4974–84.

[75] Whitesides, G. M. *Nature* **2006,** *442,* 368–373.

[76] Brody, J. P.; Yager, P.; Goldstein, R. E.; Austin, R. H. *Biophys. J.* **1996,** *71,* 3430–3441.

[77] Collins, S. R.; Douglass, A.; Vale, R. D.; Weissman, J. S. *PLOS Biol.* **2004,** *2,* 1582–1590.

[78] Knowles, T. P. J.; Shu, W.; Devlin, G. L.; Meehan, S.; Auer, S.; Dobson, C. M.; Welland, M. E. *PNAS* **2007,** *104,* 10016–10021.

[79] Cannon, M. J.; Williams, A. D.; Wetzel, R.; Myszka, D. G. *Anal. Biochem.* **2004,** *328,* 67–75.

[80] Behrens, S. H.; Grier, D. G.; Behrens, S. H.; Grier, D. G. *J. Chem. Phys.* **2001,** *115,* 6716.

[81] Beamer, W. H.; Maxwell, C. R. *J. Chem. Phys.* **1946,** *14,* 569.

[82] Chernov, A. *Sov. Phys. Crystallogr.* **1963,** *7,* 728–730.

[83] Cabrera, N.; Levine, M. M. *Philosophical Magazine* **1956,** *1,* 450–458.

[84] a.a. Chernov, *Progress in Crystal Growth and Characterization of Materials* **1993,** *26,* 121–151.

[85] Lewis, B. *J. Cryst. Growth* **1974,** *21,* 40–50.

[86] Takubo, H.; Kume, S. *J. Cryst. Growth* **1984,** *67,* 217–226.

[87] Li, S.; Xu, J.; Luo, G. *J. Cryst. Growth* **2007,** *304,* 219–224.

[88] Yan, X.; Cui, Y.; He, Q.; Wang, K.; Li, J. *Chem. Mater.* **2008,** *20,* 1522–1526.

[89] Souza, M. I.; Jaques, Y. M.; de Andrade, G. P.; Ribeiro, A. O.; da Silva, E. R.; Fileti, E. E.; Ávilla, E. D. S.; Pinheiro, M. V. B.; Krambrock, K.; Alves, W. A. *J. Phys. Chem. B* **2013,** *117,* 2605–14.

[90] Levin, A.; Michaels, T.; Adler-Abramovich, L.; Mason, T. O.; Müller, T.; Zhang, B.; Mahadevan, L.; Gazit, E.; Knowles, T. P. J. *Nature Physics* **2016,** *12,*.

[91] Andersen, K. B.; Christiansen, N. O.; Castillo-León, J.; Rozlosnik, N.; Svendsen, W. E. *Org. Electron.* **2013,** *14,* 1370–1375.

[92] Gadewar, S. B.; Doherty, M. F. *J. Cryst. Growth* **2004,** *267,* 239–250.

[93] Ban, T.; Hoshino, M.; Takahashi, S.; Hamada, D.; Hasegawa, K.; Naiki, H.; Goto, Y. *J. Mol. Biol.* **2004,** *344,* 757–67.

[94] Fitzpatrick, A. W. P. *et al. PNAS* **2013,** *110,* 5468–73.

[95] Petkova, A. T.; Leapman, R. D.; Guo, Z.; Yau, W.-M.; Mattson, M. P.; Tycko, R. *Science* **2005,** *307,* 262–5.

[96] Jansen, R.; Dzwolak, W.; Winter, R. *Biophys. J.* **2005,** *88,* 1344–1353.

[97] Buell, A. K.; Galvagnion, C.; Gaspar, R.; Sparr, E.; Vendruscolo, M.; Knowles, T. P. J.; Linse, S.; Dobson, C. M. *PNAS* **2014,** *111,* 7671–6.

[98] Cabriolu, R.; Kashchiev, D.; Auer, S. *J. Chem. Phys.* **2012,** *137,* 204903.

[99] Tang, J. X.; Wong, S.; Tran, P. T.; Janmey, P. A. *Ber. Bunsenges. Phys. Chem.* **1996,** *100,* 796–806.

[100] Yu, X.; Carlsson, A. E. *Biophys. J.* **2004,** *87,* 3679–89.

[101] Serio, T. R.; Cashikar, A. G.; Kowal, A. S.; Sawicki, G. J.; Moslehi, J. J.; Serpell, L.; Arnsdorf, M. F.; Lindquist, S. L. *Science* **2000,** *289,* 1317–1322.

[102] Reches, M.; Gazit, E. *Isr. J. Chem.* **2005,** *45,* 363–371.

[103] Makhatadze, G. I.; Privalov, P. L. *J. Mol. Biol.* **1993,** *232,* 639–659.

[104] Oosawa, F.; Kasai, M. *J. Mol. Biol.* **1962,** *4,* 10–21.

[105] Amend, J. P.; Helgeson, H. C. *Pure Appl. Chem.* **1997,** *69,* 935–942.

[106] Breil, M. P.; Mollerup, J. M.; Rudolph, E. S. J.; Ottens, M.; van der Wielen L. A. M., *Fluid Phase Equilib.* **2004,** *215,* 221–225.

[107] Lampreia, I. M. S.; Magalhaes, S. R. J.; Rodigues, S. I. M.; Mendonca, A. F. S. S. *J. Chem. Thermodynamics* **2006,** *38,* 240–244.

[108] Görbitz, C. H. *Acta Crystallogr. C* **2004,** *60,* o810—-o812.

[109] Görbitz, C. H.; Hartviksen, L. M. *Acta Crystallogr. C* **2008,** *64,* 171–6.

[110] Görbitz, C. H. *Acta Crystallogr. B* **2010,** *66,* 84–93.

[111] Karplus, P. A. *Protein Sci.* **1997,** *6,* 1302–1307.

[112] Pochapsky, T. C.; Gopen, Q. *Protein Sci.* **1992,** *1,* 786–795.

[113] Walsh, P.; Simonetti, K.; Sharpe, S. *Structure* **2009,** *17,* 417–426.

[114] Marshall, K. E.; Serpell, L. C. *Open Biol. J.* **2009,** *2,* 185–192.

[115] Rochet, J.-C.; Lansbury, P. T. *Curr. Opin. Struc. Biol.* **2000,** *10,* 60–68.

[116] Smith, J. F.; Knowles, T. P. J.; Dobson, C. M.; MacPhee, C.; Welland, M. E. *PNAS* **2006,** *103,* 15806–15811.

[117] Goldsbury, C.; Kistler, J.; Aebi, U.; Arvinte, T.; Cooper, G. J. *J. Mol. Biol.* **1999,** *285,* 33–39.

[118] Okuno, H.; Mori, K.; Jitsukawa, T.; Inoue, H.; Chiba, S. *Chem. Biol. Drug Des.* **2006,** *68,* 273–275.

[119] Buell, A. K.; Blundell, J. R.; Dobson, C. M.; Welland, M. E.; Terentjev, E. M.; Knowles, T. P. J. *Phys. Rev. Lett.* **2010,** *104,* 228101.

[120] Kusumoto, Y.; Lomakin, A.; Teplow, D. B.; Benedek, G. B. *PNAS* **1998,** *95,* 12277–12282.

[121] Vogel, S. *Life's Devices: The Physical World of Animals and Plants;* Princeton University Press: 1988.

[122] Wilke, C. R.; Chang, P. *A.I.Ch.E. Journal* **1955,** *1,* 264–270.

[123] Mason, T. O.; Michaels, T. C.; Levin, A.; Gazit, E.; Dobson, C. M.; Buell, A. K.; Knowles, T. P. J. *J. Am. Chem. Soc.* **2016,** *138,* 9589–9596.

[124] Buell, A. K.; Dhulesia, A.; White, D. A.; Knowles, T. P. J.; Dobson, C. M.; Welland, M. E. *Angew. Chem., Intl. Ed. Engl.* **2012,** *51,* 5247–5251.

[125] Richards, F. M. *Annu. Rev. Biophys. Bioeng.* **1977,** *6,* 151–176.

[126] Hermann, R. B. *J. Phys. Chem.* **1972,** *76,* 2754–2758.

[127] Bellesia, G.; Shea, J. *Biophys. J.* **2009,** *96,* 875–886.

[128] Ostwald, W. *Z. Phys. Chem.* **1897,** *22,* 289–330.

[129] Charalambidis, G.; Kasotakis, E.; Lazarides, T.; Mitraki, A.; Coutsolelos, A. G. *Chemistry* **2011,** *17,* 7213–7219.

[130] Hamley, I. W. *Angew. Chem., Intl. Ed. Engl.* **2007,** *46,* 8128–47.

[131] Mahler, A.; Reches, M.; Rechter, M.; Cohen, S.; Gazit, E. *Adv. Mater.* **2006,** *18,* 1365–1370.

[132] Orbach, R.; Adler-abramovich, L.; Zigerson, S.; Mironi-harpaz, I.; Seliktar, D. *Biomacromolecules* **2009,** *10,* 2646–2651.

[133] Smith, M. I.; Sharp, J. S.; Roberts, C. J. *Biophys. J.* **2008,** *95,* 3400–3406.

[134] Cohen, S. I. A.; Linse, S.; Luheshi, L. M.; Hellstrand, E.; White, D. A.; Rajah, L.; Otzen, D. E.; Vendruscolo, M.; Dobson, C. M.; Knowles, T. P. J. *PNAS* **2013,** *110,* 9758–63.

[135] Knowles, T. P. J.; White, D. A.; Abate, A. R.; Agresti, J. J.; Cohen, S. I. A.; Sperling, R. A.; Genst, E. J. D.; Dobson, C. M.; Weitz, D. A. *PNAS* **2011,** *108,* 14746–14751.

[136] Levin, A.; Mason, T. O.; Adler-Abramovich, L.; Buell, A. K.; Meisl, G.; Galvagnion, C.; Bram, Y.; Stratford, S. A.; Dobson, C. M.; Knowles, T. P. J.; Gazit, E. *Nat. Commun.* **2014,** *5,*.

[137] Lifshitz, I. M.; Slyozov, V. V. *J. Phys. Chem. Solids* **1961,** *19,* 35–50.

[138] Kahlweit, M. *Adv Coll. Interface Sci.* **1975,** *5,* 1–35.

[139] Wagner, C. *Z. Elektrochem.* **1961,** *65,* 1961.

[140] Vengrenovitch, R. D. *Acta. Metall.* **1982,** *30,* 1079–1086.

[141] Zeng, H. C. *Curr. Nanosci.* **2007,** *3,* 177–181.

[142] Wong, E. M.; Bonevich, J. E.; Searson, P. C. **1998,** *5647,* 7770–7775.

[143] Vauthey, S.; Santoso, S.; Gong, H.; Watson, N.; Zhang, S. *PNAS* **2002,** *99,* 5355–5360.

[144] Santoso, S.; Hwang, W.; Hartman, H.; Zhang, S. *Nano Lett.* **2002,** *2,* 687–691.

[145] Bekard, I. B.; Asimakis, P.; Bertolini, J.; Dunstan, D. E. *Biopolymers* **2011,** *95,* 733–745.

[146] Talboys, B. L.; Dunnill, P. *Biotech. Bioeng.* **1985,** *27,* 1726–1729.

[147] San Biagio, P. L.; Martorana, V.; Emanuele, A.; Vaiana, S. M.; Manno, M.; Bulone, D.; Palma, M. U. *Proteins* **1999,** *37,* 116–120.

[148] Shankaran, H.; Neelamegham, S. *Biophys. J.* **2004,** *86,* 576–588.

[149] Jin, H.-J.; Kaplan, D. *Nature* **2003,** *424,* 1057–1061.

[150] Vollrath, F.; Knight, D. P. *Nature* **2001,** *410,* 541–548.

[151] Dirix, C.; Meersman, F.; Macphee, C. E.; Dobson, C. M.; Heremans, K. *J. Mol. Biol.* **2005,** *347,* 903–909.

[152] Petty, S. A.; Decatur, S. M. *PNAS* **2005,** *102,* 14272–14277.

[153] Souillac, P. O.; Uversky, V. N.; Millett, I. S.; Khurana, R.; Doniach, S.; Fink, A. L. *J. Biol. Chem.* **2002,** *277,* 12666–12679.

[154] Bemporad, F.; Chiti, F. *Chem. Biol. (Oxford UK)* **2012,** *19,* 315–327.

[155] Calamai, M.; Chiti, F.; Dobson, C. M. *Biophys. J.* **2005,** *89,* 4201–4210.

[156] Lee, J.; Culyba, E. K.; Powers, E. T.; Kelly, J. W. *Nat. Chem. Biol.* **2011,** *7,* 600–607.

[157] Auer, S.; Ricchiuto, P.; Kashchiev, D. *J. Mol. Biol.* **2012,** *422,* 723–30.

[158] Miti, T.; Mulaj, M.; Schmit, J. D.; Muschol, M. *Biomacromolecules* **2015,** *16,* 326–335.

[159] Mankar, S.; Anoop, A.; Sen, S.; Maji, S. K. *Nano Rev.* **2011,** *2,* 1–12.

[160] Rho, J Y, A. R. B.; H, T. C. *J. Biomech.* **1993,** *26,* 111–119.

[161] Capone, R.; Quiroz, F. G.; Prangkio, P.; Saluja, I.; Sauer, A. M.; Bautista, M. R.; Turner, R. S.; Yang, J.; Mayer, M. *Neurotoxic. Res.* **2009,** *16,* 1–13.

[162] Chandler, D. *Nature* **2002,** *417,* 491.

[163] Rissanou, A. N.; Georgilis, E.; Kasotakis, E.; Mitraki, A.; Harmandaris, V. *J. Phys. Chem. B* **2013,** *117 (15),* 3962–3975.

[164] Myshakina, N. S.; Ahmed, Z.; Asher, S. A. *J. Phys. Chem. B Lett.* **2008,** *112,* 11873–11877.

[165] Noblin, X.; Rojas, N. O.; Westbrook, J.; Llorens, C.; Dumais, J. *Science* **2012,** *335,* 1322.

[166] Duncanson, W. J.; Lin, T.; Abate, A. R.; Seiffert, S.; Shah, R. K.; Weit, *Lab Chip* **2012,** *12,* 2135–2145.

[167] Shang, L.; Cheng, Y.; Zhao, Y. *Chem. Rev.* **2017,** *117,* 7964–8040.

[168] Lee, J. N.; Park, C.; Whitesides, G. M. *Analytical chemistry* **2003,** *75,* 6544–54.

[169] Toepke, M. W.; Beebe, D. J. *Lab Chip* **2006,** *6,* 1484–1486.

[170] Wang, J. D.; Douville, N. J.; Takayama, S.; Elsayed, M. *Ann. Biomed. Eng.* **2012,** *40,* 1862–1873.

[171] Robb, W. L. *Ann. N. Y. Acad. Sci.* **1968,** 119–137.

[172] Randall, G. C.; Doyle, P. S. *PNAS* **2005,** *102,* 10813–10818.

[173] Owen, M. J.; Smith, P. J. *J. Adhes. Sci. Technol.* **1994,** *8,* 1063–1075.

[174] Eddington, D. T.; Puccinelli, J. P.; Beebe, D. J. *Sens. Actuators B* **2006,** *114,* 170–172.

[175] Kim, B.; Peterson, E. T. K.; Papautsky, I. *Proc. 26th Ann. Int. Conf. IEEE EMBS* **2004,** 5013–5016.

[176] Zhou, M.; Smith, A. M.; Das, A. K.; Hodson, N. W.; Collins, R. F.; Ulijn, R. V.; Gough, J. E. *Biomaterials* **2009,** *30,* 2523–30.

[177] Zhang, H.; Chiao, M. *J. Med. Biol. Eng.* **2015,** *35,* 143–155.

[178] Turnbull, D. *Phase Change in Solid State Physics, vol. 2;* Academic Press Inc. (London): 1956.

[179] Umbanhowar, P. B.; Prasad, V.; Weitz, D. A. *Langmuir* **2000,** *16,* 347–351.

[180] DeMenech, M.; Garstecki, P.; Jousse, F.; Stone, H. A. *J. Fluid. Mech.* **2008,** *595,* 141–161.

[181] Hazlett, R. D.; Schechter, R. S. *Colloids Surf.* **1988,** *29,* 53–69.

[182] Bancroft, W. D. *J. Phys. Chem.* **1913,** *17,* 501–519.

[183] Winsor, P. A. *Chem. Rev.* **1968,** *68,* 1–38.

[184] Ruckenstein, E. *Langmuir* **1996,** *12,* 6351–6353.

[185] Heller, W.; Pugh, T. L. *J. Chem. Phys.* **1954,** *22,* 1778.

[186] Sadtler, V. M.; Krafft, M. P.; Riess, J. G. *Angew. Chem., Int. Ed. Engl.* **1996,** *35,* 1976–1978.

[187] Riess, J. G. *Tetrahedron* **2002,** *58,* 4113–4131.

[188] Roach, L. S.; Song, H.; Ismagilov, R. F. *Anal. Chem.* **2005,** *77,* 785–796.

[189] Holtze, C.; Rowat, A. C.; Agresti, J. J.; Hutchison, J. B.; Angilè, F. E.; Schmitz, C. H. J.; Köster, S.; Duan, H.; Humphry, K. J.; Scanga, R. A.; Johnson, J. S.; Pisignano, D.; Weitz, D. A. *Lab Chip* **2008,** *8,* 1632–9.

[190] Debon, A. P.; Wootton, R. C. R.; Elvira, K. S. *Biomicrofluidics* **2015,** *9,* 024119.

[191] Azuri, I.; Adler-Abramovich, L.; Gazit, E.; Hod, O.; Kronik, L. *J. Am. Chem. Soc.* **2014,** *136,* 963–9.

[192] Gazit, E. *Angew Chem Int Ed Engl* **2002,** *41,* 257–259.

[193] Ryan, D. M.; Doran, T. M.; Nilsson, B. L. *Langmuir* **2011,** *27,* 11145–56.

[194] Higa, T.; Suetsugu, N.; Kong, S.; Wada, M. *PNAS* **2014,** *111,* 4327–4331.